



저작자표시-비영리-변경금지 2.0 대한민국

이용자는 아래의 조건을 따르는 경우에 한하여 자유롭게

- 이 저작물을 복제, 배포, 전송, 전시, 공연 및 방송할 수 있습니다.

다음과 같은 조건을 따라야 합니다:



저작자표시. 귀하는 원저작자를 표시하여야 합니다.



비영리. 귀하는 이 저작물을 영리 목적으로 이용할 수 없습니다.



변경금지. 귀하는 이 저작물을 개작, 변형 또는 가공할 수 없습니다.

- 귀하는, 이 저작물의 재이용이나 배포의 경우, 이 저작물에 적용된 이용허락조건을 명확하게 나타내어야 합니다.
- 저작권자로부터 별도의 허가를 받으면 이러한 조건들은 적용되지 않습니다.

저작권법에 따른 이용자의 권리는 위의 내용에 의하여 영향을 받지 않습니다.

이것은 [이용허락규약\(Legal Code\)](#)을 이해하기 쉽게 요약한 것입니다.

[Disclaimer](#)

공학박사 학위논문

Amorphous Phyllosilicate for Efficient Oxygen Evolution Reaction Catalyst

수소 생산용 비정질 층상규산염을 이용한
산소 발생 촉매에 관한 연구

2018년 2월

서울대학교 대학원
재료공학부
김 주 성

Abstract

Amorphous Phyllosilicate for Efficient Oxygen Evolution Reaction Catalyst

Ju seong Kim

Department of Materials Science and Engineering

The Graduate School

Seoul National University

Hydrogen is one of the most promising renewable source for next efficient energy generation because of its sustainability and higher energy density than conventional energy sources. Hydrogen can be produced from various method, however, splitting water is considered as the best solution to produce hydrogen owing to its advantages such as clean, environmentally-friendly and sustainability. In order to meet the industrial demand, integrating efficient water splitting system is crucial. Among the components of the water splitting system, the development of low-cost and efficient oxygen evolution reaction (OER) catalyst is pivotal because OER is the bottleneck of the overall water splitting reaction due to the sluggish multielectron reaction and O-O bond formation compared to hydrogen evolution reaction (HER). Many researches have been conducted to develop novel efficient OER catalysts and to understand the mechanism of OER.

In the early stage of the research about OER catalysts, precious metal based electrocatalyst such as Ru, Ir and their oxide material has been widely studied owing to their superior performance. However, their scarcity has led to

high prices, and this has been the biggest obstacle to commercialization. As a solution to this problem, 3d transition metal (Mn, Fe, Co and Ni) based catalysts have been proposed. Many reported transition metal-based catalysts show excellent properties and stability in neutral and alkaline electrolytes. In addition, many studies have been carried out to analyze the mechanism and the determinants of performance, but it is still controversial in many areas, and further research is needed.

In this thesis, we have designed an OER catalyst with excellent performance by using the mineral which exists in nature called phyllosilicate and analyzed the effect of the elements in the crystal structure on OER. We believe that phyllosilicate-based catalysts can pave a new unexplored avenue for the design of high performance catalyst.

In **chapter 2**, we introduced an amorphous cobalt phyllosilicate (ACP) with layered crystalline motif as a new efficient OER catalyst. A structural investigation using X-ray absorption spectroscopy revealed that the amorphous structure contains layered motifs similar to the structure of CoOOH, which is demonstrated to be responsible for the OER catalysis based on density functional theory calculations. However, the calculations also revealed that the local environment of the active site in the layered crystalline motif in the ACP is significantly modulated by the silicate, leading to a substantial reduction of η of the OER compared with that of CoOOH.

Chapter 3 presented the role of iron and cobalt in the OER through amorphous cobalt-iron binary phyllosilicate (ACFP). It was confirmed that prepared ACFP had a solid solution form in which cobalt and iron were uniformly mixed. As iron was added, overpotential tended to decrease until Fe content reached 40% and the Tafel slope decreased compared to the Co phase in all regions. The calculations revealed that inactive sites for oxygen evolution in the pure cobalt phyllosilicate phase could become active by lowering its overpotential of rate

determining step.

Keywords: Phyllosilicate, Water Electrolysis, Oxygen Evolution Reaction,
Layered (oxy)hydroxides, Transition metal, Electrocatalyst

Student Number: 2009-23894

Contents

List of Tables.....	vii
---------------------	-----

List of Figures	viii
-----------------------	------

Chapter 1. Introduction	1
1.1 Hydrogen energy as a future energy resources.....	1
1.2 Hydrogen production: Water electrolysis	2
1.3 Overall water splitting reaction	5
1.4 Oxygen evolution reaction	7
1.5 Literature review on OER catalyst.....	10
1.6 Purpose of this thesis.....	12

Chapter 2. Experimental details	14
2.1 Materials preparation	14
2.1.1 Synthesis of ACP and annealed ACP	14
2.1.2 Synthesis of ACFP and annealed ACFP series.....	14
2.1.3 Preparation of CoOOH, Co ₃ O ₄ , CoO, and LiCoO ₂	15

2.1.4	Synthesis of CFH series	16
2.1.5	Electrode preparation	16
2.2	Characterization.....	17
2.2.1	Material characterization.....	17
2.2.2	Electrochemical characterization	18
2.3	Computational details	20
2.3.1	Calculation details.....	20
2.3.2	Thermodynamics of OER.....	21

Chapter 3 Amorphous Cobalt Phyllosilicate with Layered Crystalline Motifs as Water Oxidation Catalyst.....24

3.1	Introduction	24
3.2	Results and Discussions.....	27
3.2.1	Phase identification of ACP.....	27
3.2.2	Electrochemical properties of ACP.....	46
3.2.3	Oxidation state and local structure of ACP	57
3.2.4	Slab modeling for DFT calculation.....	66
3.2.5	OER thermodynamics	76
3.3	Conclusion	83

Chapter 4 Activation of Reaction Sites in Amorphous Cobalt Iron Phyllosilicate for the Efficient Oxygen Evolution

Reaction	84
4.1 Introduction	84
4.2 Results and Discussions.....	88
4.2.1. Phase identification of ACFP	88
4.2.2. XPS analysis for solid solution forming.....	100
4.2.3. Electrochemical properties of ACFP	104
4.2.4. The oxidation state analysis: EPR analysis.....	111
4.2.5. Determination of reaction sites in ACFP	113
4.2.6. Tracking bridge site oxygen evolution	119
4.3. Conclusion.....	121
<hr/>	
Chapter 5. Concluding remarks	122
<hr/>	
Chapter 6. Abstract in Korean	126
<hr/>	
Chapter 7. Curriculum Vitae	128
<hr/>	
Chapter 8. References	134
<hr/>	

List of Tables

Table 3.2.1.	Elemental composition of ACP prepared using Co/Si precursor ratio of 3:4.....	34
Table 3.2.2.	Elemental composition of ACP prepared using Co/Si precursor ratio of 3:2.....	35
Table 3.2.3.	Elemental composition of ACP prepared using Co/Si precursor ratio of 3:3.....	36
Table 3.2.4.	Elemental composition of ACP prepared using Co/Si precursor ratio of 3:5.....	37
Table 3.2.5.	Structural parameters of the theoretically fitted FT-EXAFS spectra.	63
<hr/>		
Table 4.2.1.	Ratios of elements in the series of ACFP.....	99
<hr/>		
Table 5.1.	Electrocatalytic OER activities of previously reported metal oxidecatalysts	124

List of Figures

Figure 1.2.1.	Several method of hydrogen production and demand.....	3
Figure 1.2.2.	Illustration of differnet kinds of electrolyzer	4
Figure 1.3.1.	Schematic illustration of the oxygen evolution reaction and hydrogen evolution reaction	6
Figure 1.4.1.	Volcano plot of oxygen evolution catalyts using adsorption energies as a descriptor.....	9
<hr/>		
Figure 3.2.1.	Crystal structure of phyllosilicate (inset: two types of phyllosilicates).....	31
Figure 3.2.2.	Powder XRD patterns of the pristine ACP and ACP after hydrothermal treatment	32
Figure 3.2.3.	FT-IR spectra of the pristine ACP and ACP after hydrothermal treatment.....	33
Figure 3.2.4.	Variation of Co/Si ratio with precursor ratio.....	38
Figure 3.2.5.	Scanning electron microscopy (SEM) image of the ACP prepared	

	by co-precipitation method	39
Figure 3.2.6.	Powder XRD patterns of the ACP prepared with different precursor ratio	40
Figure 3.2.7.	Polarization curves of the ACP in 1 M KOH electrolyte prepared with different precursor ratios.....	41
Figure 3.2.8.	Schematic representation of CoOOH and ACP structures: the CoOOH and ACP consist of edge-sharing CoO ₆ octahedra, and the silicate layer of ACP consists of a Si-deficient structure in contrast to the ideal phyllosilicate structure, which consists of a hexagonal tetrahedral ring.	42
Figure 3.2.9.	Structure of cobalt phyllosilicate Co ₃ Si ₂ O ₉ H ₄ . Co ₃ Si ₂ O ₉ H ₄ consists of a cobalt hydroxide layer and perfect hexagonal silicate chains at one side of the cobalt layers. The other side is terminated with hydrogen. Co, Si, O, and H are represented by blue, green, red, and white spheres, respectively.	43
Figure 3.2.10.	Structure of cobalt phyllosilicate Co ₃ Si ₄ O ₁₂ H ₂ . The Co ₃ Si ₄ O ₁₂ H ₂ consists of a cobalt hydroxide layer and perfect hexagonal silicate chains at both sides of the cobalt layers. Co, Si, O, and H are represented by blue, green, red, and white spheres, respectively..	44

Figure 3.2.11. Calculated structure of the ACP ($\text{Co}_3\text{Si}_3\text{O}_{12}\text{H}_6$). Based on the reported structures of cobalt phyllosilicate ($\text{Co}_3\text{Si}_2\text{O}_9\text{H}_4$ and $\text{Co}_3\text{Si}_4\text{O}_{12}\text{H}_2$), we predicted the structural motif of the ACP with $\text{Co}:\text{Si}:\text{O} = 1:1:4$ using DFT calculations. Hydrogen atoms were added to maintain the Co oxidation state at 2+. (a) The homogeneous model with Si-deficient chains at both sides of the cobalt hydroxide layer shows much more stable energy (7.5 meV per atom) than that of (b) the inhomogeneous model with Si-deficient chain at one side of the cobalt hydroxide layer. Co, Si, O, and H are represented by blue, green, red, and white spheres, respectively.....	45
Figure 3.2.12. <i>iR</i> -corrected polarization curves in 1 M KOH at a scan rate of 10 mV s^{-1}	48
Figure 3.2.13. Powder XRD pattern of the CoOOH nanoplates	49
Figure 3.2.14. SEM image of the CoOOH nanoplates.....	50
Figure 3.2.15. Powder XRD pattern of the Co_3O_4 nanoparticles.....	51
Figure 3.2.16. SEM image of the Co_3O_4 nanoparticles.....	52
Figure 3.2.17. OER η required for $j = 10 \text{ mA cm}^{-2}$	53

Figure 3.2.18.	Tafel plots in 1 M KOH at a scan rate of 10 mV s ⁻¹	54
Figure 3.2.19.	$\Delta j = j_a - j_c$ at 1.05 V vs. RHE as a function of the scan rate to evaluate C_{dl}	55
Figure 3.2.20.	Long-term stability of ACP at $j = 10 \text{ mA cm}^{-2}$ for 24 h.....	56
Figure 3.2.21.	XANES Co K-edge spectra of the as-prepared ACP and ACP after 1st CV. For comparison, the spectra of CoO and LiCoO ₂ are also shown for reference samples of Co ²⁺ and Co ³⁺ , respectively.....	59
Figure 3.2.22.	Oscillations of the EXAFS spectra of the as-prepared ACP, ACP after electrolysis, and CoOOH.....	60
Figure 3.2.23.	k^3 -weighted FT-EXAFS spectra of the as-prepared ACP, ACP after electrolysis, and CoOOH.....	61
Figure 3.2.24.	Comparison of experimental FT-EXAFS spectrum (dotted line) of the ACP after electrolysis and theoretical fit (red line)	62
Figure 3.2.25.	Comparison of experimental FT-EXAFS spectrum (dotted line) of the CoOOH after electrolysis and theoretical fit (red line).....	64
Figure 3.2.26.	Comparison between experimental FT-EXAFS spectrum of the as-prepared ACP (dotted line) and theoretical fit (red line)	65

Figure 3.2.27. Side view of CoOOH ($10\bar{1}4$) surface, which is the most active surface for the OER.....	68
Figure 3.2.28. Side view of CoOOH surface with similar atomic configuration as the CoOOH ($10\bar{1}4$) surface. The ACP surface has a longer interlayer distance than the CoOOH surface.	69
Figure 3.2.29. Top view of active surface of CoOOH, showing active sites for the OER.....	70
Figure 3.2.30. Top view of active surface of ACP, showing active sites for the OER.....	71
Figure 3.2.31. Crystal structure of (a) CoOOH and (b) ACP; the cleavage lines are shown in black. Note that the ($10\bar{1}4$) surface is the most OER-active surface from CoOOH. The cleavage line for ACP has a similar atomic configuration as the CoOOH ($10\bar{1}4$) surface, and the silicate tetrahedron is preserved.	72
Figure 3.2.32. Surface termination of the ACP surface (model 1) corresponding to the potential. (a) Surface phase diagram as a function of applied potential for ACP surface model. Stable surface structures with adsorbates corresponding to applied potential with: (b) 1 monolayer (ML) of co-adsorbed H ₂ O (below 1.1 V), (c) 1 ML of	

OH and 3/4 ML of H (from 1.1 to 1.8 V), and (d) 1 ML of OH and 1/4 ML (above 1.8 V). For improved clarity, only the topmost atoms are shown..... 73

Figure 3.2.33. Surface structures of another surface of the ACP model (model 2). Unlike the ACP surface model in Figure 5, silicates are adsorbed at the bridge site rather than the terminal site. (a) Side view of the CoOOH surface with similar atomic configuration as the CoOOH ($10\bar{1}4$) surface. (b) Top view of the active surface of ACP showing the active sites for the OER. Co, Si, O, and H are represented by blue, green, red, and white spheres, respectively. For improved clarity, only the topmost atoms are shown..... 74

Figure 3.2.34. Surface termination of another ACP surface (model 2) corresponding to the potential. (a) Surface phase diagram as a function of applied potential for the ACP surface model. Stable surface structures with adsorbates corresponding to applied potential with: (b) 1 ML of co-adsorbed H₂O (below 1.1 V), (c) 1 ML of OH and 3/4 ML of H (from 1.1 to 1.8 V), and (d) 1 ML of OH and 1/4 ML (above 1.8 V). For improved clarity, only the topmost atoms are shown. 75

Figure 3.2.35. Theoretical η for OER of plausible sites. Some bridge sites on the ACP surface show much lower η than the active sites of CoOOH.79

Figure 3.2.36.	Free energy landscape for OER at 1.23 V (ideal potential for OER). The black, cyan, and blue lines indicate the free energy of the ACP bridge 1 site, CoOOH bridge site, and CoOOH terminal site, respectively.	80
Figure 3.2.37.	Comparison of the structures for the OOH* formation step (rate- determining step for these cases) at the ACP bridge 1 site. Reaction sites and hydrogen bonds are indicated with yellow and red circles, respectively. Further adjustment of the bond length at the ACP surface reduces the OER η	81
Figure 3.2.38.	Comparison of the structures for the OOH* formation step (rate- determining step for these cases) at the CoOOH bridge site	82
<hr/>		
Figure 4.2.1.	Powder XRD patterns of the series of as-prepared ACFPs.....	91
Figure 4.2.2.	Powder XRD patterns of the series of annealed ACFPs after hydrothermal treatment.....	92
Figure 4.2.3.	FT-IR spectra of as-prepared ACFP.....	93
Figure 4.2.4.	FT-IR spectra of annealed ACFP after hydrothermal treatment....	94
Figure 4.2.5.	Schematic illustrated crystal structure of cobalt iron	

phyllosilicate.....	95
Figure 4.2.6. XANES Co <i>K</i> -edge spectra of the series of as-prepared ACFP. For comparison, the spectra of CoO, and LiCoO ₂ are shown for reference samples of Co ²⁺ , and Co ³⁺ , respectively.	96
Figure 4.2.7. XANES Fe <i>K</i> -edge spectra of the series of as-prepared ACFP. For comparison, the spectra of Fe ₂ O ₃ is shown for reference samples of Fe ³⁺	97
Figure 4.2.8. Quantative analysis of Co/Fe ratio from EDS.....	98
Figure 4.2.9. XPS Co 2p spectra of the series of ACFP. Enlarged Co 2p _{3/2} peak is in right panel	102
Figure 4.2.10. XPS Fe 2p spectra of the series of ACFP. Enlarged Fe 2p _{3/2} peak is in right panel	103
Figure 4.2.11. <i>iR</i> -corrected polarization curves in 1 m KOH at a scan rate of 10 mV s ⁻¹	106
Figure 4.2.12. Double layer capacitance of the series of ACFPs for comparison of electrochemical active surface area.....	107
Figure 4.2.13. Tafel plots of the series of ACFP corresponding to Figure 4.2.1.	108

Figure 4.2.14. Overpotential and Tafel slope variation as a function of Fe content.	109
Figure 4.2.15. Overpotential comparison of phyllosilicate and hydroxide catalysts...	110
Figure 4.2.16. EPR spectra of ACFP10 and ACFP64. For comparison, the as-prepared sample and the sample when the OER potential was applied were plotted together...	112
Figure 4.2.17. Top view of active surface of ACFP, showing active sites for the OER. Co, Fe, Si, O, and H are represented by blue, dark yellow, green, red, and white spheres, respectively.	116
Figure 4.2.18. Radar plot for comparison with pure ACP and Fe-doped ACP of overpotential at each sites.	117
Figure 4.2.19. Free energy landscape of pure ACP and Fe-doped ACP for OER at 1.23 V (ideal potential for OER)..	118
Figure 4.2.20. DEMS analysis during OER to detect $^{34}\text{O}_2$ gas evolution.	120

Chapter 1. Introduction

1.1. Hydrogen Energy as a future energy resources

Demand for energy is increasing rapidly due to the continuous industrial development and population growth. Most energy requirements today rely heavily on carbon-based resources, such as oil, natural gas, and coal. However, the exhaustion of fossil fuels, environmental pollution by harmful gas and the greenhouse effect caused by CO₂ emissions have been emerging as serious problems for establishment of sustainable energy system. Developing new alternative energy is extremely important for the sustainability of our society. Accordingly, many energy resources that can replace fossil fuels are being researched widely for a sustainable energy system.

Among the various candidates for renewable energy resources, including wind, tidal, geothermal and biomass, hydrogen energy has been at the center of attention.[1, 2] Hydrogen is inexhaustible because it is formed from earth-abundant reactants such as water and methane, and environmentally friendly because it does not emit CO₂ or other toxic products during the conversion to electricity. Moreover, hydrogen energy has the advantage of an enormous energy density with 141.9 kJ g⁻¹ compared to other energy sources such as gasoline with 46.5 kJ g⁻¹ and coal with 30.2 kJ g⁻¹. Hydrogen energy can be used in fuel cells for producing electricity by combining hydrogen and oxygen molecules.

1.2. Hydrogen production: Water electrolysis

To use hydrogen as an energy resource for large-scale industry, it is necessary to produce high purity hydrogen. Several methods of hydrogen production are shown in **Figure 1.2.1**. The widely used method of hydrogen production today is steam reforming because of its low cost.[3] However, since carbon monoxide or carbon dioxide is released as a product in the process, it fades the advantage of environmentally friendly hydrogen energy. In order to replace this process, an electrolysis method of producing hydrogen by splitting water has been attracting attention. Water is one of the most abundant resources and environmentally friendly, because it emits only hydrogen and oxygen as products. The unit for water electrolysis, called an electrolyzer, can be used on a wide range of scales from small to large. In addition, electricity required for electrolysis can be obtained from unlimited solar energy by combining with a light absorbing material. The electrolyzer can be classified into polymer electrolyte membrane (PEM) electrolyzer, alkaline electrolyzer and solid oxide electrolyzer according to the electrolyte material of the cell. The schematic image of the various types of electrolyzer is shown in **Figure 1.2.2**. [4]

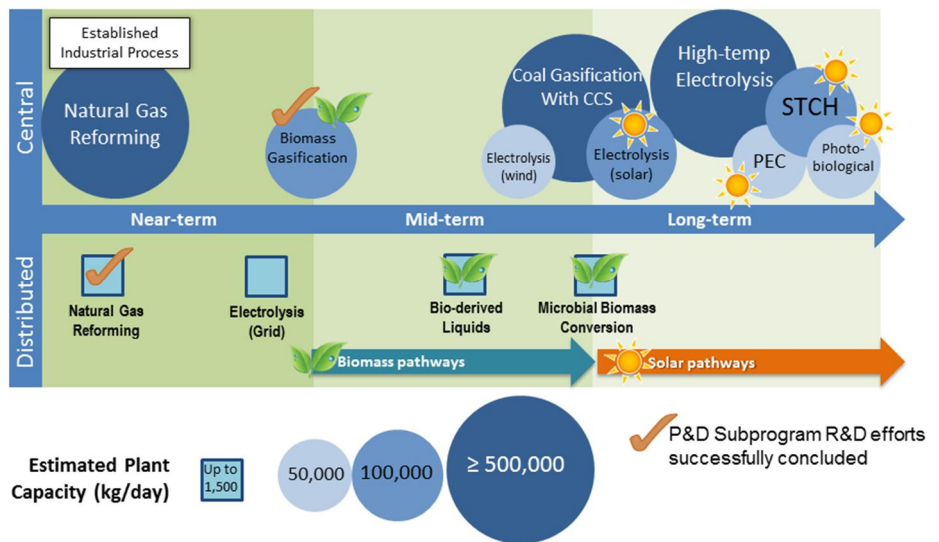


Figure 1.2.1. Several method of hydrogen production. Based on U. S. Department of Energy data from *Fuel cell technologies office. Hydrogen Production Pathways*. License: <https://energy.gov/eere/fuelcells/hydrogen-production-pathways>[5]

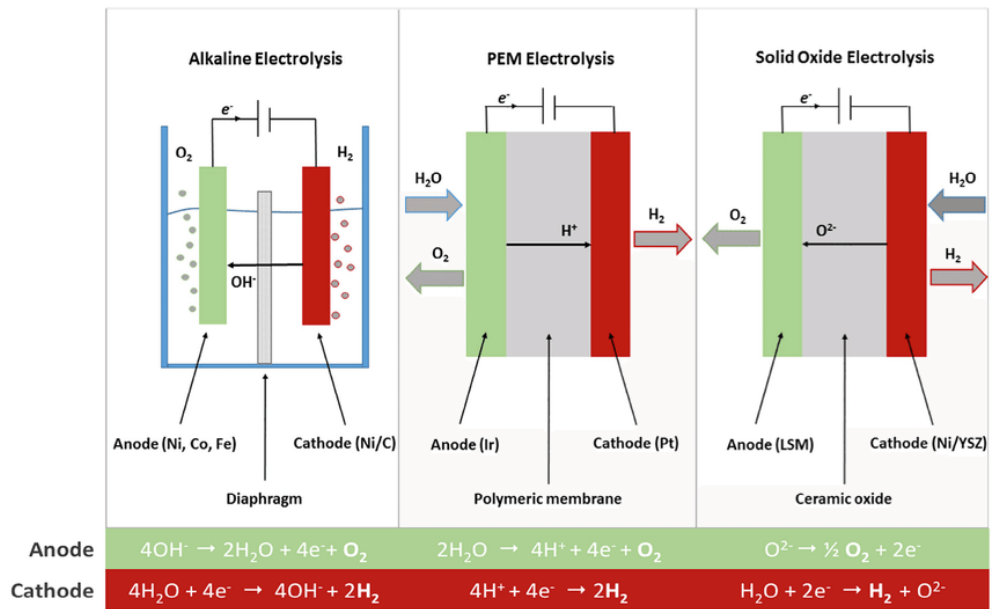
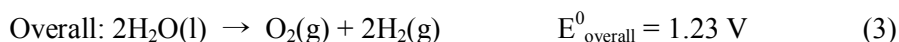
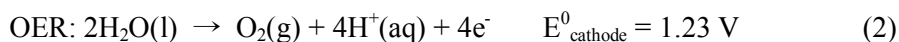


Figure 1.2.2. Illustration of different kinds of electrolyzer.[4]

1.3. The overall water splitting reaction

In the overall water splitting reaction, both hydrogen evolution reaction (HER) and oxygen evolution reaction (OER) occur simultaneously and can be described as shown in the following equation and briefly illustrated in **Figure 1.3.1**.



Thermodynamically, a potential of 1.23 V vs. reversible hydrogen electrode (RHE) is needed. However, overpotential (given the symbol η) is required because of potential loss due to problems of electrical series resistance and kinetics during electrochemical reaction. The electrocatalyst that promotes the water splitting reaction can reduce requiring overpotential, which is directly related to the performance of the electrolyzer. Therefore, developing an efficient electrocatalyst that operates at low applied voltage is the most important thing in the commercialization of hydrogen energy. In particular, OER has been regarded as a bottleneck reaction because of sluggish kinetic involving two more electrons compared to HER and the high activation energy for O-O bond formation. Many researchers have started to look for efficient electrocatalyst for OER in order to improve the efficiency of water splitting.

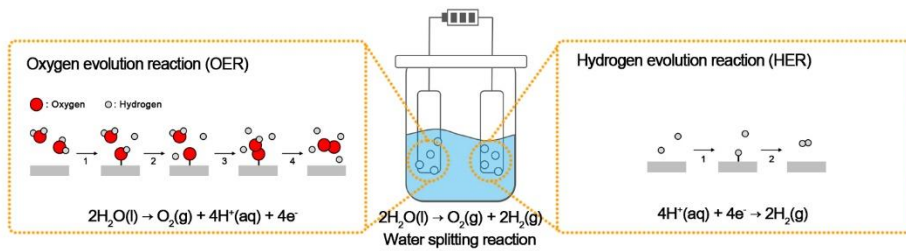
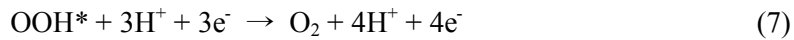
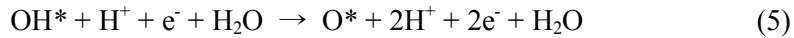


Figure 1.3.1. Schematic illustration of the oxygen evolution reaction and hydrogen evolution reaction.

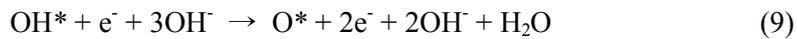
1.4. Oxygen evolution reaction

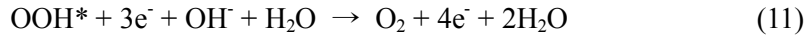
OER is accompanied by the transfer reaction of four electrons and protons and proceeds in four steps. At each steps, the electron and proton are transferred together, which is called proton coupled electron transfer (PCET). Although many OER mechanisms presented so far have been varied, the reaction usually begins with adsorption of the intermediate from the water molecule to the active site. The intermediates adsorbed on the active site is changed as each step proceeds. According to a generally known mechanism, it changes as follows. ($\text{OH}^* \rightarrow \text{O}^* \rightarrow \text{OOH}^* \rightarrow \text{O}_2$). And the 4 steps of OER is described differently under acidic and alkaline environment. And the four step of the OER can be written as follows.[6, 7]

In an acidic environment,



In an alkaline environment,





where * denotes a surface active site.

Since these four steps are thermodynamically uphill process, the overpotential requires for each step. The overpotential of the overall reaction is determined by the step requiring the largest activation barrier, which means rate-determining step. It is noteworthy that there is a correlation between the energy barriers of each step, called the scaling relation. The sum of energies required for $\text{OH}^* \rightarrow \text{O}^*$ step and $\text{O}^* \rightarrow \text{OOH}^*$ step is fixed to 3.2 eV. Therefore, this scaling relation can be expressed by the volcano plot in **Figure 1.4.1**. [8] If the energies of $\text{OH}^* \rightarrow \text{O}^*$ and $\text{O}^* \rightarrow \text{OOH}^*$ steps are same, the point will be on top of the peak which means that it has the smallest overpotential. Therefore, the closer the adsorption site of catalysts are to the peak of the volcano plot, the higher the efficiency of the catalysts is.

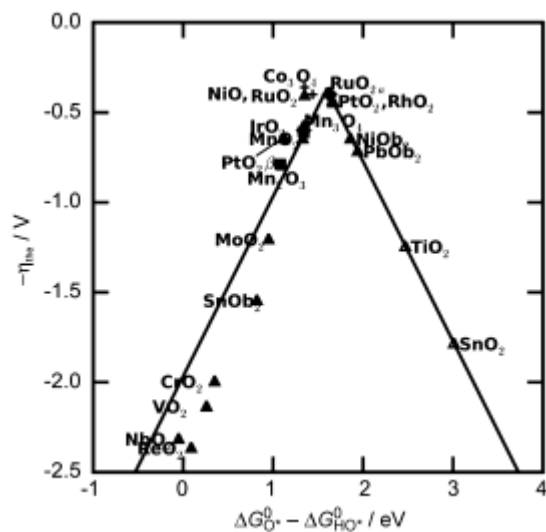


Figure 1.4.1. Volcano plot of oxygen evolution catalysts using adsorption energies as a descriptor.

1.5. Literature review on OER catalyst

In the early stage of the research, precious metal based electrocatalyst has been widely studied due to their performance and stability. For example, Ru, Ir and their oxide based electrocatalyst exhibits superior OER activity under both acidic and alkaline condition. However, rutile type RuO_2 and IrO_2 has been reported to easily dissolve during OER in a high acidic and high anodic condition, respectively.[9-11] Apart from stability, the high price of materials due to its scarcity can be a big obstacle for large-scale commercialization. (Ru = \$ 65.00 oz^t⁻¹ and Ir = \$ 970.00 oz^t⁻¹, Jul 2017)[12] In order to replace precious metals, a number of researches have begun to address 3d transition metal (Mn, Fe, Co and Ni) based catalysts.[13-16] High-efficiency catalysts based on 3d-metals have been reported from a variety of material groups, such as layered hydroxide, spinel, perovskite and amorphous materials. Various studies reported layered hydroxide as stable and efficient OER catalyst under alkaline condition.[17, 18] On the other hand, perovskite family can provide chemical tunability because they can accommodate various metals in their two atomic sites, so several perovskite catalysts showed excellent performance by tuning a factor that affects a oxygen evolution reaction called descriptor.[19] Nocera group have triggered the developments of amorphous catalysts.[13] They synthesized amorphous Co phosphate and Ni borate film through electrodeposition with metal ions and anion buffer solution, and it showed superior activity in neutral and alkaline electrolytes. In addition, local structural

analysis has reported that this amorphous oxide film has a layered structure, and many have noted the advantages of this structure in the oxygen evolution reaction.[20, 21] Furthermore, it has been found that the role of anions in amorphous films can play a role in inducing reactions even if they are not directly involved in the oxygen evolution reaction through various materials and various analyzes.[22-24] Recently, excellent performance and stability of various layered double hydroxide (LDH), especially NiFe LDH, catalysts in alkaline electrolyte have been reported. Numerous experimental analyzes and first principles calculations have been conducted to find the cause of superior performance.[25-30] In addition, a variety of new OER catalysts have been reported from the combination of transition metals with oxidation state of 2+ and 3+. As a result, the interest of many studies has focused on the role of each element during the reaction and many hypotheses about the role of each element have been reported.[31, 32]

1.6. Purpose of this thesis

Despite the various 3d transition metal-based catalysts reported so far, their performance were not high enough to replace noble metal-based catalysts. Therefore, for the realization of the hydrogen energy system, it is urgently required to develop a catalyst having superior performance and excellent price competitiveness. The purpose of this thesis is to reach the industrialization of hydrogen energy by developing an OER electrocatalyst with low cost and superior performance by using phyllosilicate material which is a natural mineral. From the viewpoint of synthesis process, we solved the problem that could be a stumbling block in actual commercialization by using synthesis method available at room temperature without special equipment.

This thesis suggests strategies to develop highly efficient OER catalysts. First, it will show that redox inactive part in the crystal structure can modulate the overpotential of active sites and help improve the properties through the amorphous cobalt phyllosilicate. In the layered structure, the silicate layer can enhance the structural flexibility during the oxygen evolution reaction by cutting off the O-H-O bonding between the layers, which can reduce the overpotential required for the oxygen evolution reaction. The second is that the reaction site, which was inactive with high overpotential for the oxygen evolution reaction, could be activated by the addition of iron to the amorphous cobalt phyllosilicate. Therefore, it was shown that the oxygen evolution reaction activity can be

improved by increasing the current density through the proper amount of iron. Also, the specific surface area and conductivity of the phyllosilicate catalyst could be improved through the nanosize carbon-active catalyst hybrid structure. More specifically, a nanotube with a core-shell shape was synthesized by coating a carbon nanotube (CNT) with a phyllosilicate catalyst. The nanotube shape exhibited a high specific surface area, and the conductivity was preserved through the CNT corresponding to the core.

Chapter 2. Experimental details

2.1 Materials preparation

2.1.1 Synthesis of ACP and annealed ACP

ACP was prepared by a simple co-precipitation method using cobalt chloride (CoCl_2 , Sigma-Aldrich) and sodium metasilicate (Na_2SiO_3 , Sigma-Aldrich). First, 10.7 mmol Na_2SiO_3 dissolved in 15 ml of deionized water was added to 8 mmol CoCl_2 dissolved in 75 ml of deionized water under vigorous stirring for 30 min. A hydrothermal process was used to synthesize crystallized ACP. The solution described above was transferred into a sealed Teflon-lined stainless steel autoclave. The autoclave was annealed at 200 °C for 24 h in an air atmosphere. All the obtained precipitates were washed using centrifugation with deionized water and ethanol several times and were then dried in a vacuum oven at 70 °C.

2.1.2 Synthesis of ACFP and annealed ACFP series

The series of ACFP were synthesized by a same method with ACP. Briefly, 10.7 mmol sodium metasilicate (Na_2SiO_3 , Sigma-Aldrich) dissolved in 15 mL of deionized water was added into 8 mmol of the total amount of cobalt chloride (CoCl_2 , Sigma-Aldrich) and iron chloride tetrahydrate ($\text{FeCl}_2 \cdot 4\text{H}_2\text{O}$) with

mole ratios of 10:0, 8:2, 6:4, 4:6, 2:8, and 0:10 dissolved in 75 mL of deionized water under stirring for 30 min. For the annealed ACFP series, annealing process was fabricated through hydrothermal method. The mixed solution described above was transferred into a sealed Teflon-lined stainless steel autoclave and heated at 180 °C for 24 h in an air atmosphere. All precipitated solution were washed several times with deionized water and ethanol using centrifugation and dried in a vacuum oven at 70 °C.

2.1.3 Preparation of CoOOH, Co₃O₄, CoO, and LiCoO₂

A previously reported method was used to synthesize CoOOH nanoplates using air oxidation.[70] A solution of 20 mmol Co(NO₃)₂·6H₂O dissolved in 100 ml of deionized water was added to 100 ml of a 5 M NaOH aqueous solution. Pink precipitates were formed, and the solution was diluted by pouring it into 1800 ml of deionized water. The diluted solution was stirred for 8 h, and the solution turned brown, indicating that the precipitated Co(OH)₂ (pink) was oxidized to CoOOH (brown). The CoOOH nanoplates were washed using the same steps described above. The Co₃O₄ nanoparticles and as-received CoO (Sigma-Aldrich) were directly used for comparison. LiCoO₂ bulk powder was synthesized using a conventional solid-state reaction method. As-received Li₂CO₃ and Co₃O₄ (Sigma-Aldrich) were used as the raw materials and were mixed using a high-energy ball

mill at 400 rpm for 4 h. After mixing, the mixture was heated at 900 °C for 6 h under an air atmosphere.

2.1.4 Synthesis of CFH series

The synthesis of CFH were processed by homogeneous precipitation using same metal precursor with ACFP, hexamethylenetetramine (HMT) and sodium nitrate (NaNO_3 , Sigma-Aldrich). After dissolving 10 mmol of the total amount of metal precursor, 10 mmol HMT, and 4 mmol NaNO_3 in 50 mL of deionized water, the solution was placed in an 80 °C vacuum oven for 24 h. All solution became opaque due to the precipitation reaction, the obtained precipitates were collected using the same method as above.

2.1.5 Electrode preparation

Carbon fiber paper (CFP) was used as the substrate for the working electrodes. First, 5 mg of the active materials was dispersed in 1 ml of deionized water with 0.1 ml of neutralized Nafion solution and sonicated for 30 min to form a homogeneous ink. The ink was then uniformly dropped onto the CFP with a mass loading of 0.4 mg cm^{-2} . The prepared electrode was dried in a 80 °C oven for 30

min. The Co_3O_4 nanoparticles and CoOOH electrodes were prepared under the same conditions.

2.2 Characterization

2.2.1 Material characterization

X-ray diffraction (XRD, D8 Advance, Bruker) with $\text{Cu K}\alpha$ radiation was used to investigate the crystal structure of the prepared samples. The ACP was identified using Fourier-transform infrared (FT-IR) spectroscopy (Hyperion 3000, Bruker). An electron probe microanalyzer (JXA-8530F, JEOL) and EDS coupled with FE-SEM (SU70, Hitachi) were used to analyze the element composition. The morphology and size of the clusters were investigated using high-resolution transmission electron microscopy (HR-TEM, JEM-2100F, JEOL). The oxidation state and local environment of the Co ions were investigated using X-ray absorption near edge structure (XANES) and X-ray absorption fine structure (EXAFS) analyses. The XANES and EXAFS analyses were performed at the 8C-Nano X-ray Absorption Fine Structure (XAFS) beamline at the Pohang Accelerator Laboratory (PAL). All the data were collected in transmittance mode using an electron energy of 2.5 GeV and current of 400 mA in top-up mode. To examine the local structural properties around the Co atoms, EXAFS data were extracted from full XAFS spectra. IFEFFIT software following a standard procedure was used to

analyze the EXAFS data.[71-73] After removing the atomic background with the AUTOBK code (a part of IFEFFIT), the EXAFS data were obtained as a function of the photoelectron wave number, $k = \sqrt{2m(E - E_0)}/\hbar$, where m is the electron mass, E is the incident X-ray energy, and E_0 is the absorption edge energy. XPS spectroscopy (Sigma probe, VG) was used to analyze binding energy of Co and Fe in the series of ACFP. EPR spectra were obtained by Bruker EMX plus spectrometer in the X band continuous wave EPR spectroscopy. All measurement were measured at the low temperature (~5.7K) by liquid He with control system (ER4112HV). For EPR measurement, catalyst paste layer combined with carbon was formed on the substrate in a large area. After bulk electrolysis at 1.6 V_{RHE} during 10 min, the catalyst layer was collected after detaching from substrate by razor blade and transferred to EPR tube to freeze immediately. Gas analysis for detecting 34O2 gas was performed using differential electrochemical mass spectrometry (DEMS, HPR-20, Hiden Analytical, U.K.) in swagelok cell.

2.2.2 Electrochemical characterization

Electrochemical measurements were performed using a three-electrode beaker cell system with an electrochemical potentiostat (CHI 608C, CH Instruments). In the OER test, a Hg/HgO electrode filled with 1 M NaOH solution

and Pt were used as the reference electrode and counter electrode, respectively. The potentials of all the data were converted to the reversible hydrogen electrode (RHE) scale, and the overpotential (η) at a current density (j) of 10 mA cm^{-2} was determined using the following equation, $\eta = E \text{ (vs. RHE)} - 1.23 \text{ V}$. The ohmic resistance was automatically compensated. Cyclic voltammetry (CV) curves were recorded in 1 M KOH solution at a scan rate of 10 mV s^{-1} . The capacitive background current was removed by averaging the forward and backward scan. Tafel plots of the samples were obtained by plotting η against the logarithm of j using the Tafel equation ($\eta = a \log j + b$, where a is the slope and b is a constant). A long-term stability test was performed at $j = 10 \text{ mA cm}^{-2}$ for 24 h. The electrochemically active surface area was determined based on the capacitive charging current of the electrochemical double layer. The potential range was 1.00–1.01 V vs. RHE, and the scan rates were 10, 20, 40, 60, 80, and 100 mV s^{-1} in 1 M KOH electrolyte. The double layer capacitance (C_{dl}) was determined from a plot of $\Delta j = j_a - j_c$ vs. the scan rate using the following equation:

$$q = C_{dl}E$$

$$j = \frac{\partial q}{\partial t} = C_{dl} \left(\frac{\partial E}{\partial t} \right).$$

Here, q is the charge and E is the potential. All the electrochemical measurements were conducted at room temperature.

2.3 Computational details

2.3.1 Calculation details

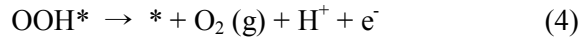
First-principles calculations presented in this work were performed based on plane-wave-based density functional theory (DFT) using the Vienna *ab initio* simulation package (VASP).[74] The projector augmented wave (PAW) pseudopotentials were used as implemented in VASP.[75] Exchange-correlation energies were described within the spin-polarized generalized gradient approximation plus Hubbard- U (GGA+ U) framework parameterized using the Perdew-Burke-Ernzerhof (PBE) functional.[76, 77] The effective Hubbard- U parameters of $U_{\text{eff}}(\text{Co}) = 3.5$ eV and $U_{\text{eff}}(\text{Fe}) = 4.0$ eV were applied to 3d electrons of Co atoms and Fe atoms respectively, which are in good agreement with the values reported in other works.[15, 82, 121-124] We also employed self-consistent implicit solvation model using VaspSol software package[125, 126] to depict solvation effects, which are often considered important for the electrochemical reactions that occur at the interface of electrode-electrolyte interface such as OER.[127-129] The bulk structures were calculated within an energy cutoff of 550 eV and an appropriate gamma-point-centered k-point mesh to ensure that the total energies converged within 0.1 meV per atom. The surface structure of the ACP (or CoOOH) was calculated from a slab model consisting of three (or four) Co sites per surface and a thickness of more than 15 Å with a vacuum layer of 15 Å to

achieve convergence of the adsorption energies and bulk properties of the center layers. The three topmost ACP and CoOOH layers were allowed to relax below the maximum force threshold of 0.05 eV/Å within an energy cutoff of 550 eV and a $3 \times 3 \times 1$ gamma-point-centered k -point mesh. For the purpose of comparing OER energetics of Fe-doped/undoped ACP, a slab model which was proposed in our previous study to depict the surface of OER are also applied in this work.[15] This ACP slab model is composed of three transition metal sites per surface and a thickness of five ACP layers that are separated by more than 15 Å of vacuum to obtain convergence of the adsorption energies and bulk properties of the center layers. Fe is doped into the Co sites in the topmost surface layer of the ACP slab. The atomic positions within the topmost three layers of slab were allowed to relax below a maximum threshold force threshold force of 0.05 eV/ Å within an energy cutoff of 550 eV and a $3 \times 3 \times 1$ gamma-point-centered k -point mesh. Dipole moment correction was employed to eliminate the effect of residual dipole moments perpendicular to the surface.

2.3.2 Thermodynamics of OER

Given the surficial model and active sites, we attempted to estimate the theoretical η of the OER based on DFT calculations. Although the detailed OER mechanism is complex and not completely established, insight into the

thermodynamics of the reaction can be obtained using the acid–base mechanism scheme proposed by Nørskov *et al.*[83] In this scheme, the OER is assumed to consist of the following four elementary reaction steps (under acidic conditions):



(where * denotes a surface site and X* denotes an adsorbed X species).

During the OER with acid–base mechanism, a water molecule in the liquid phase first adsorbs on the surficial active site and dissociates into H^+ and OH^* (step 1). Then, the OH^* splits into H^+ and O^* (step 2). Next, the O^* combines with a water molecule and forms O–O bonding as the hydroperoxo intermediate OOH^* (step 3) before finally evolving as O_2 gas (step 4).

The free energy differences for the OER steps can be calculated using the following equations:

$$\begin{aligned} \Delta G_1 = G(\text{OH}^*) - G(*) - \mu_{\text{OH}} = E(\text{OH}^*) - E(*) - E(\text{H}_2\text{O}) + 1/2E(\text{H}_2) - eU + \Delta G_{\text{H}^+}(\text{pH}) \\ + \Delta(\text{ZPE} - T\Delta S) \end{aligned} \quad (5)$$

$$\begin{aligned} \Delta G_2 = G(\text{O}^*) - G(\text{OH}^*) + \mu_{\text{H}} = E(\text{O}^*) - E(\text{OH}^*) + 1/2E(\text{H}_2) - eU + \Delta G_{\text{H}^+}(\text{pH}) + \\ \Delta(\text{ZPE} - T\Delta S) \end{aligned} \quad (6)$$

$$\begin{aligned} \Delta G_3 = G(\text{OOH}^*) - G(\text{O}^*) - \mu_{\text{OH}} = E(\text{OOH}^*) - E(\text{O}^*) - E(\text{H}_2\text{O}) + 1/2E(\text{H}_2) - eU + \\ \Delta G_{\text{H}^+}(\text{pH}) + \Delta(\text{ZPE} - T\Delta S) \end{aligned} \quad (7)$$

$$\Delta G_4 = 4 \times [1.23 \text{ eV} - eU + \Delta G_{\text{H}^+}(\text{pH})] - (\Delta G_1 + \Delta G_2 + \Delta G_3), \quad (8)$$

where U is the potential measured against a normal hydrogen electrode (NHE) under standard conditions. The Gibbs free energy change of a proton relative to the pH is represented by the Nernst equation as $\Delta G_{\text{H}^+}(\text{pH}) = -k_{\text{B}}T \log(\text{pH})$. The Gibbs free energy differences for each step (ΔG_i) are calculated from the DFT energy, zero-point energy (ZPE), and entropy correction according to $\Delta G_i = \Delta E_i + \Delta \text{ZPE}_i - T\Delta S_i$. To avoid the calculation including O_2 gas, which is difficult to determine within the GGA-DFT scheme, the sum of ΔG_{1-4} was fixed at 4.92 eV, which is the experimental Gibbs free energy change in $2\text{H}_2\text{O} > 2\text{H}_2 + \text{O}_2$.

The theoretical η could be obtained from the free energy differences at each step as

$$\eta = \max [\Delta G_1, \Delta G_2, \Delta G_3, \Delta G_4]/e - 1.23 \text{ V}. \quad (9)$$

Chapter 3. Amorphous Cobalt Phyllosilicate with Layered Crystalline Motifs as Water Oxidation Catalyst

(The content of this chapter has been published in *Advanced Materials*. Reprinted with permission from [J. S. Kim *et al.*, *Adv. Mater.*, **2017**, 29, 1606893; DOI: 10.1002/adma.201606893]. Copyright 2017 Wiley.)

3.1. Introduction

Electrochemical water splitting has been regarded as a promising and eco-friendly approach to produce hydrogen, a clean fuel, by avoiding a dependency on fossil fuels.[33-39] The oxygen evolution reaction (OER) is the bottleneck of the overall water-splitting reaction because of the sluggish multi-electron reaction and O–O bond formation.[13, 19, 40, 41] Precious-metal-based catalysts such as RuO₂ and IrO₂ have been widely studied as prime catalysts for the OER because of their superior catalytic activity.[42-46] However, the rarity and high cost of precious metals prohibit the large-scale commercialization of these catalysts; therefore, tremendous research efforts have been directed toward the search for efficient and inexpensive OER catalysts based on non-precious transition metals.[14, 27, 31, 47-61] Nocera and co-workers reported that Co- and Ni-based materials such as

amorphous cobalt phosphates and nickel borates are capable of delivering comparable performance to that of conventional catalysts even in neutral and weak alkaline electrolytes.[13, 54] In addition, more recent studies have revealed that layered metal (oxy)hydroxides can be effective electrocatalysts, among which layered double hydroxides containing Ni, Fe, or Co can exhibit remarkably high OER catalytic activity that can surpass that of precious-metal-based catalysts.[62-64]

Unveiling the origin of the high catalytic activity in these transition-metal-based OER catalysts would provide insight for the rational design of new efficient catalysts. In this respect, an atomistic level of understanding of the activity of OER catalysts is necessary with consideration of the local environment of the redox-active transition metal element. Recent studies have proposed that the coordination number of transition metals (MO_x), their local distortion, and how they are connected (*i.e.*, edge-shared or corner-shared) can sensitively affect the catalytic activity.[14, 20, 21, 65, 66] Furthermore, neighboring redox-inert elements can alter the redox activity of catalysts; for example, anions such as phosphate and borate facilitate proton-coupled electron transfer,[24, 67, 68] and capping anion species affect the domain size of electrodeposited amorphous catalysts,[20-23] significantly altering the catalysis. In addition, in our recent study, it was demonstrated that the phosphate or pyrophosphate group in catalysts such as $\text{Mn}_3(\text{PO}_4)_2 \cdot 3\text{H}_2\text{O}$, LiMnP_2O_7 , and $\text{Na}_2\text{CoP}_2\text{O}_7$ can enhance the structural flexibility, thereby stabilizing the transition metal and promoting the OER activity,[14, 16, 69]

which is indicative of the importance of the relationship between the structure and catalytic properties.

Herein, we report an amorphous cobalt phyllosilicate (ACP) with layered crystalline motif as a new efficient OER catalyst. The ACP catalyst can be prepared using a simple, fast, and low-cost precipitation method at room temperature and exhibits one of the highest OER activities among known Co-based catalysts. In our investigation to elucidate the origin of the catalysis, it is revealed that the OER activity stems from the layered crystalline motif in the ACP, which resembles the structure of CoOOH. Nevertheless, silicate groups present in the interlayer space of the layered crystalline motif significantly modulate the local environment of the active sites and substantially reduce the overall OER overpotential (η) compared with that of conventional layered metal (oxy)hydroxides, as demonstrated by density functional theory (DFT) calculations. This finding suggests that the structural modulation by introducing redox-inert groups in the layer space of metal (oxy)hydroxides can be a viable strategy to tune the catalytic activity and that transition-metal-based phyllosilicates may be new candidates for low-cost and efficient OER catalysts.

3.2 Results and Discussions

3.2.1 Phase identification of ACP

Phyllosilicate minerals generally refer to a class of earth-abundant layered materials comprising a sheet of edge-shared MO_6 (M: Mg, Fe, Co, Ni, and Al) octahedra and a polysilicate sheet with corner-shared silicate tetrahedra, as schematically illustrated in **Figure 3.2.1**. Each sheet is alternatively stacked with shared oxygen atoms; however, one or two polysilicate sheets may simultaneously reside between MO_6 sheets, forming an overall layered structure ($\text{M}_3\text{Si}_2\text{O}_5(\text{OH})_4$ or $\text{M}_3\text{Si}_4\text{O}_{10}(\text{OH})_2$), as depicted in the bottom panel of **Figure 3.2.1**. [84-86] Without the presence of the polysilicate sheets, the overall crystal is isostructural to typical metal hydroxides (MOOH). Among various transition metals that could be adopted in phyllosilicate form, we selected Co-based phyllosilicates as the system for this study. The cobalt phyllosilicate phase was synthesized at room temperature using a simple co-precipitation method. X-ray diffraction (XRD) analysis of the precipitates (black lines in **Figure 3.2.2**) revealed a generally broad peak pattern, which indicates their amorphous nature. [87, 88] To obtain further insight regarding the precipitate phase, we hydrothermally annealed the sample at 200 °C for 24 h. Figure 1b shows that the XRD pattern of the annealed sample is similar to that of the pristine powder; however, the peaks ($\sim 35^\circ$ and 60°) are sharper than those of the pristine precipitate, indicating the formation of a more crystalline phase of

layered cobalt phyllosilicates, $\text{Co}_3\text{Si}_2\text{O}_5(\text{OH})_4$ and $\text{Co}_3\text{Si}_4\text{O}_{10}(\text{OH})_2$, as schematically illustrated in the bottom panel of **Figure 3.2.1**.

The Fourier-transform infrared (FT-IR) spectra of the precipitate powder in **Figure 3.2.3** also confirm the characteristic local environment of the layered cobalt phyllosilicates. The peaks at 3629 and 1010 cm^{-1} correspond to the O–H vibration mode (ν_{OH}) of the OH–3Co group surrounded by three Co atoms and the Si–O vibration mode (ν_{SiO}), respectively. In addition, the peak at 663 cm^{-1} is attributed to the superimposition of the δ_{OH} vibration of the OH–3Co group and the ν_{SiO} vibration mode, and the peak at 451 cm^{-1} is assigned to the asymmetric Si–O bending vibration.[89] All of these bonding characters indicate that the precipitate basically exhibits the local orderings of crystalline cobalt phyllosilicates but lacks long-range ordering, as evidenced by the XRD result in Figure 1b. Thus, we call the precipitate powder an ACP, which will be further verified by X-ray absorption spectroscopy later. Note that the shoulder peak at 925 cm^{-1} that typically arises from the vibration of silanol (Si–OH) groups[90] is particularly pronounced for the pristine ACP. Silanol groups should not exist in a perfectly ordered polysilicate sheet in the layered phyllosilicate; however, a defective structure can induce their presence by bonding four protons with oxygen atoms surrounding a Si^{4+} vacant site to compensate for the charge imbalance, which is called a hydrogarnet-type substitution.[91, 92] This observation indicates that the ACP contains a significant amount of Si vacant sites and implies that the structure cannot be defined as the sole phase of either $\text{Co}_3\text{Si}_2\text{O}_5(\text{OH})_4$ or $\text{Co}_3\text{Si}_4\text{O}_{10}(\text{OH})_2$. We expect that the rapid

precipitation reaction causes the loss of long-range ordering with defective silicate chains in the ACP, which results in silanol groups in the basal plane of the silicate oxygen.

The chemical composition of the ACP was examined using electron probe microanalysis. The average atomic percentages of Co, Si, and O were 15.1, 16.6, and 68.3, respectively, indicating that the atomic ratio of Co:Si:O was approximately 1:1:4 (see **Table 3.2.1**). This result further suggests that the ACP cannot be solely designated as either $\text{Co}_3\text{Si}_2\text{O}_5(\text{OH})_4$ or $\text{Co}_3\text{Si}_4\text{O}_{10}(\text{OH})_2$, which is consistent with the observation of the hydrogarnet-type substitution previously discussed. Indeed, a previous experimental study reported that non-stoichiometric phyllosilicates can be synthesized with a significant amount of Si vacancies in the polysilicate layer.[92] To verify the composition of the phase, ACPs with various Co/Si precursor ratios were additionally synthesized. The Co/Si ratios of the precipitate samples, however, remained approximately 1, as observed in **Figure 3.2.4**, and no particular change is observed in the XRD patterns and the catalytic activities in **Figure 3.2.6** and **Figure 3.2.7**, respectively. These results indicate that regardless of the ratio of the precursor reactants, all the ACPs prepared at room temperature formed a relatively stable phase with a 1:1:4 ratio of Co, Si, and O comprised of non-stoichiometric silicate layers and CoO_6 layers.

A model crystal structure of the ACP is proposed with a molecular formula of $\text{Co}_3\text{Si}_3\text{O}_6(\text{OH})_6$ characterized by (i) the basic cobalt phyllosilicate structure, (ii) the existence of silanol groups originating from Si vacancies, and (iii)

the aforementioned experimental observations of the atomic ratio of 1:1:4 (Co:Si:O). **Figure 3.2.8** shows the optimized structure of $\text{Co}_3\text{Si}_3\text{O}_6(\text{OH})_6$ obtained from the DFT calculations. The ACP (right panel of **Figure 3.2.8**) adopts a similar crystal structure as CoOOH (left panel) with a series of CoO_6 layers except for the silicate groups between CoO_6 layers, which only exist in the ACP. Although perfectly layered cobalt phyllosilicate structures exhibit a complete interconnection of the silicates with hexagonal orderings in the layer (middle panel of **Figure 3.2.8**), the ACP does not exhibit this interconnection because it includes a significant amount of Si vacancies (see **Figures 3.2.9–3.2.11**).

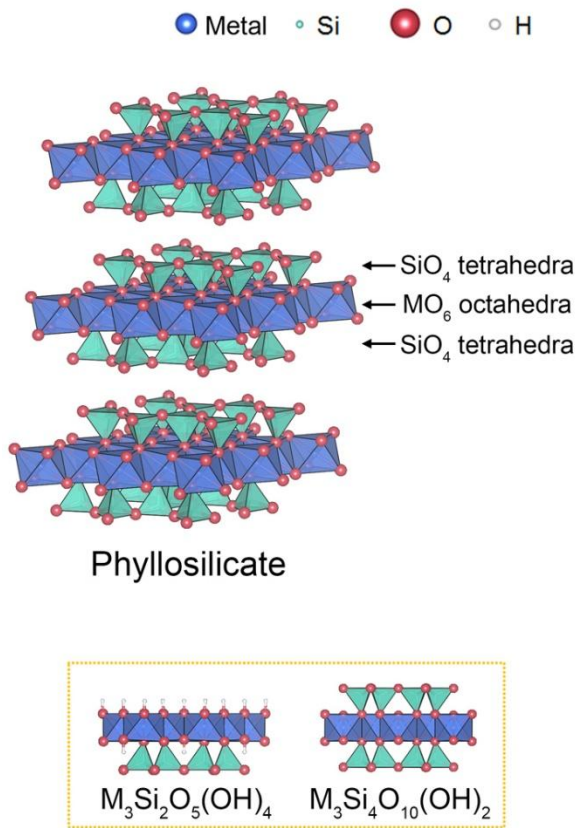


Figure 3.2.1. Crystal structure of phyllosilicate (inset: two types of phyllosilicates).

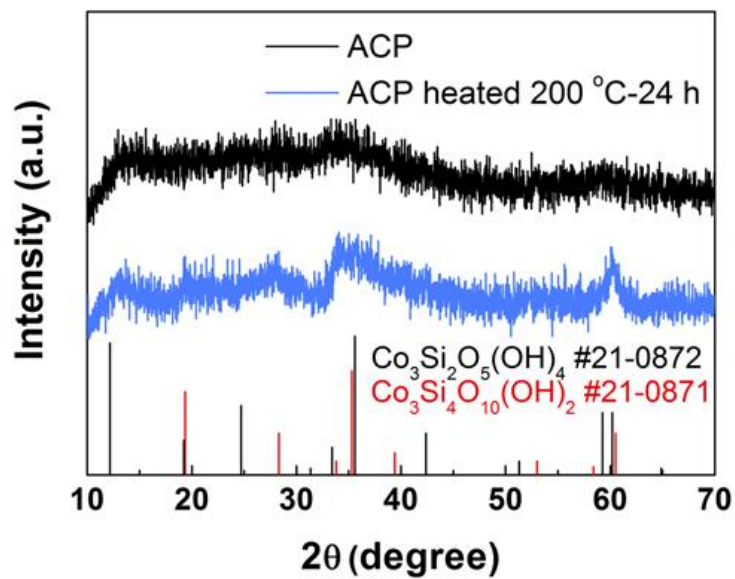


Figure 3.2.2. Powder XRD patterns of the pristine ACP and ACP after hydrothermal treatment.

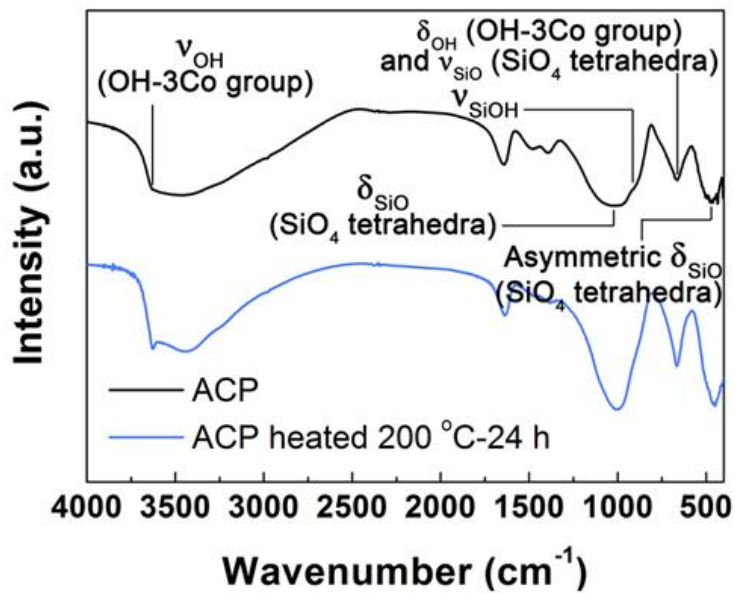


Figure 3.2.3. FT-IR spectra of the pristine ACP and ACP after hydrothermal treatment.

Table 3.2.1. Elemental composition of ACP prepared using Co/Si precursor ratio of 3:4.

Atomic %	Co	Si	O	Total
1	15.2370	16.9800	67.7830	100
2	15.2880	16.7550	67.9570	100
3	14.9050	16.1720	68.9230	100
4	15.5140	16.2910	68.1950	100
5	14.1640	16.3480	69.4880	100
6	15.8550	16.1880	67.9570	100
7	15.8800	16.2280	67.8920	100
8	15.7460	16.6800	67.5740	100
9	14.6480	16.6420	68.7090	99.9991
10	13.6870	17.6050	68.7080	100
Minimum	13.6870	16.1720	67.5740	99.999
Maximum	15.8800	17.6050	69.4880	100
Average	15.0924	16.5889	68.3186	99.9999
Sigma	0.7405	0.4516	0.6089	0.0003

Table 3.2.2. Elemental composition of ACP prepared using Co/Si precursor ratio of 3:2.

Atomic %	Co	Si	O	Total
1	17.8052	16.6459	65.5488	99.9999
2	18.309	17.0327	64.6582	100
3	18.7051	17.0357	64.2591	100
4	18.4406	17.1022	64.4572	100
5	17.1556	17.0722	65.7721	100
6	17.9667	17.1461	64.8871	99.9999
7	17.8551	16.8829	65.2621	100.0001
8	17.2881	17.0903	65.6216	100
9	17.9226	17.0617	65.0157	100
10	18.1698	17.0738	64.7565	100
Minimum	17.1556	16.6459	64.2591	99.9999
Maximum	18.7051	17.1461	65.7721	100.0001
Average	17.96178	17.01435	65.02384	99.99999
Sigma	0.481532	0.14674	0.514176	0.0001

Table 3.2.3. Elemental composition of ACP prepared using Co/Si precursor ratio of 3:3.

Atomic %	Co	Si	O	Total
1	16.9444	17.2187	65.8369	99.9999
2	17.1050	17.2684	65.6266	100
3	16.9687	17.1843	65.8470	100
4	16.3455	16.9876	66.6669	100
5	16.9389	16.8475	66.2137	100
6	17.2813	17.7745	64.9442	99.9999
7	17.4824	17.3875	65.1301	100
8	17.6743	17.2714	65.0543	100
9	16.9067	16.9744	66.1189	100
10	16.3982	16.9100	66.6919	100
Minimum	16.3455	16.8475	64.9442	100
Maximum	17.6743	17.7745	66.6919	100
Average	17.00454	17.18243	65.81305	100
Sigma	0.419574	0.274238	0.631489	4.22E-05

Table 3.2.4. Elemental composition of ACP prepared using Co/Si precursor ratio of 3:5.

Atomic %	Co	Si	O	Total
1	13.8897	15.2299	70.8804	99.9999
2	13.6022	15.7910	70.6068	100
3	13.6276	15.5769	70.7955	100
4	13.7903	15.3951	70.8146	100
5	13.3143	15.2325	71.4532	100
6	13.6235	15.7465	70.6299	99.9999
7	13.5420	15.6710	70.7870	100
8	14.7059	16.0553	69.2387	100
9	13.6650	15.6270	70.7080	100
10	13.3806	14.9869	71.6324	100
Minimum	13.3143	14.9869	69.2387	99.9999
Maximum	14.7059	16.0553	71.6324	100
Average	13.71411	15.53121	70.75465	99.99999
Sigma	0.38753	0.318701	0.634056	3.16E-05

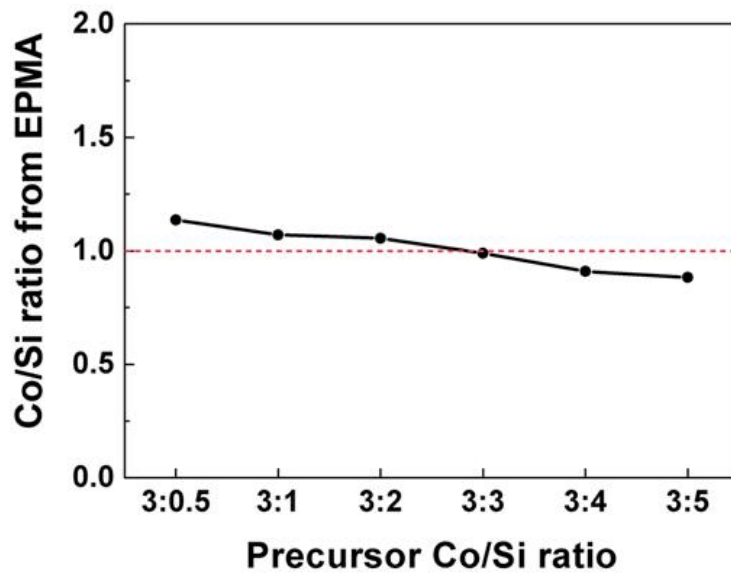


Figure 3.2.4. Variation of Co/Si ratio with precursor ratio.

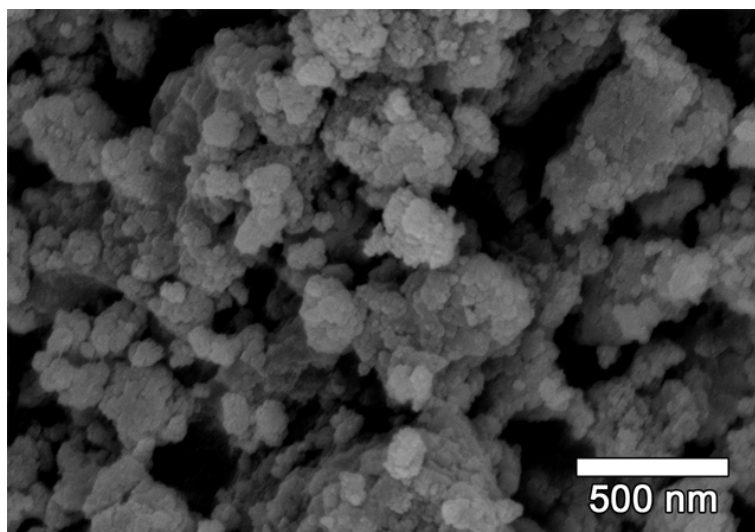


Figure 3.2.5. Scanning electron microscopy (SEM) image of the ACP prepared by co-precipitation method.

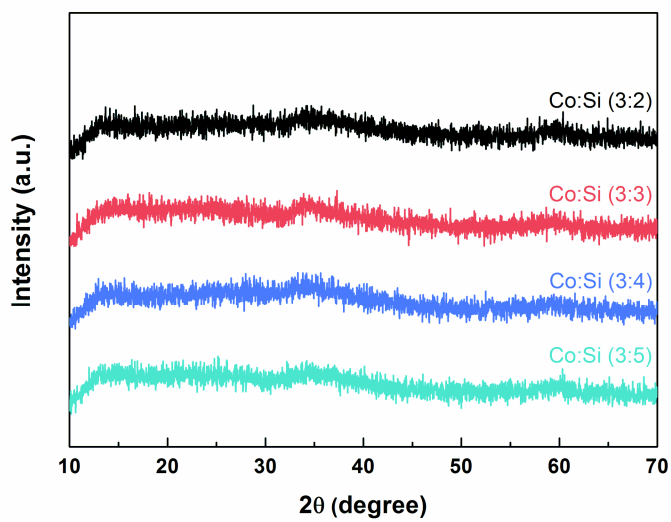


Figure 3.2.6. Powder XRD patterns of the ACP prepared with different precursor ratios.

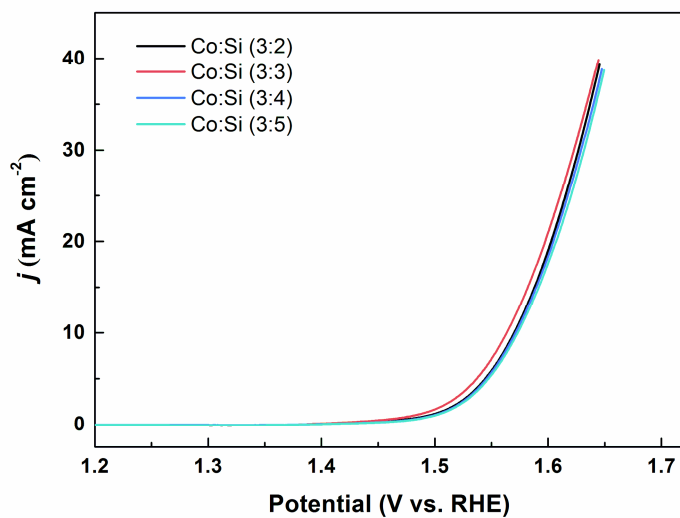


Figure 3.2.7. Polarization curves of the ACP in 1 M KOH electrolyte prepared with different precursor ratios.

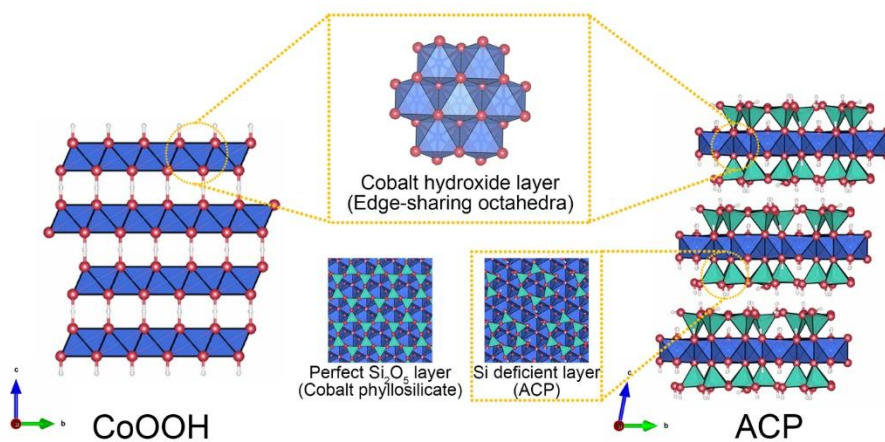


Figure 3.2.8. Schematic representation of CoOOH and ACP structures: the CoOOH and ACP consist of edge-sharing CoO₆ octahedra, and the silicate layer of ACP consists of a Si-deficient structure in contrast to the ideal phyllosilicate structure, which consists of a hexagonal tetrahedral ring.

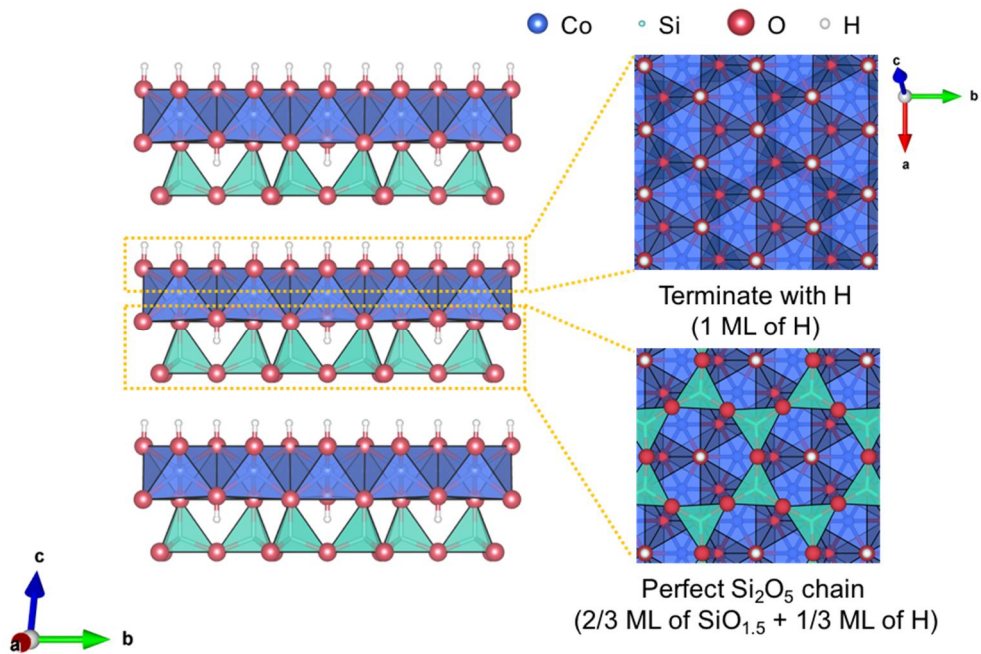


Figure 3.2.9. Structure of cobalt phyllosilicate $\text{Co}_3\text{Si}_2\text{O}_9\text{H}_4$. $\text{Co}_3\text{Si}_2\text{O}_9\text{H}_4$ consists of a cobalt hydroxide layer and perfect hexagonal silicate chains at one side of the cobalt layers. The other side is terminated with hydrogen. Co, Si, O, and H are represented by blue, green, red, and white spheres, respectively.

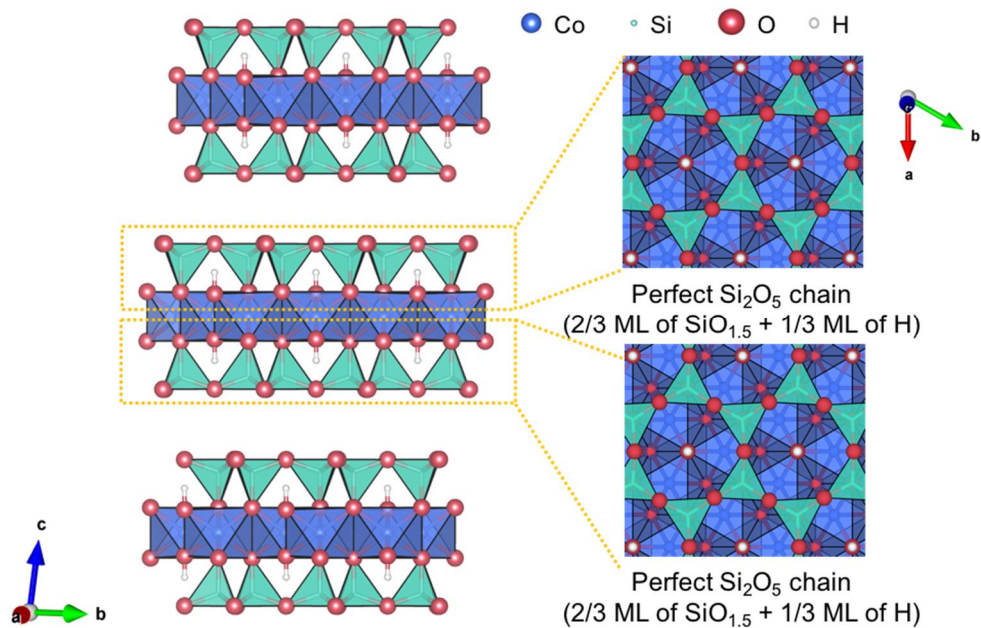


Figure 3.2.10. Structure of cobalt phyllosilicate $\text{Co}_3\text{Si}_4\text{O}_{12}\text{H}_2$. The $\text{Co}_3\text{Si}_4\text{O}_{12}\text{H}_2$ consists of a cobalt hydroxide layer and perfect hexagonal silicate chains at both sides of the cobalt layers. Co, Si, O, and H are represented by blue, green, red, and white spheres, respectively.

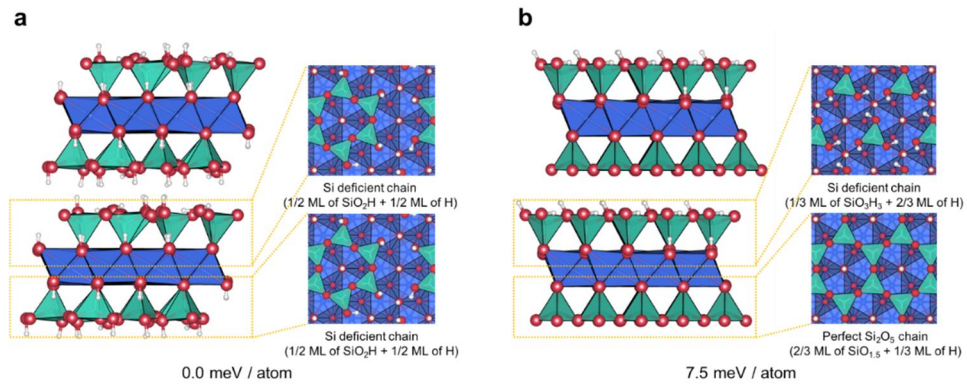


Figure 3.2.11. Calculated structure of the ACP ($\text{Co}_3\text{Si}_3\text{O}_{12}\text{H}_6$). Based on the reported structures of cobalt phyllosilicate ($\text{Co}_3\text{Si}_2\text{O}_9\text{H}_4$ and $\text{Co}_3\text{Si}_4\text{O}_{12}\text{H}_2$), we predicted the structural motif of the ACP with $\text{Co}:\text{Si}:\text{O} = 1:1:4$ using DFT calculations. Hydrogen atoms were added to maintain the Co oxidation state at $2+$. (a) The homogeneous model with Si-deficient chains at both sides of the cobalt hydroxide layer shows much more stable energy (7.5 meV per atom) than that of (b) the inhomogeneous model with Si-deficient chain at one side of the cobalt hydroxide layer. Co, Si, O, and H are represented by blue, green, red, and white spheres, respectively.

2.3.2 Electrochemical properties of ACP

The OER catalytic activity of the ACP was evaluated using cyclic voltammetry (CV) and was compared with those of well-known Co-based catalysts such as CoOOH nanoplates (NLs) and Co₃O₄ nanoparticles (NPs) (see **Figure 3.2.12**). XRD patterns and scanning electron microscopy images of the Co₃O₄ NPs and CoOOH NLs are provided in **Figure 3.2.13–3.2.16**. The iR-corrected CV curves of the ACP exhibit a lower onset potential and η than those of the CoOOH NLs and Co₃O₄ NPs at the same current density (j). η of ACP for the OER is approximately 367 mV for $j = 10 \text{ mA cm}^{-2}$, whereas the CoOOH NLs and Co₃O₄ NPs require η of 400 and 490 mV, respectively (see **Figure 3.2.17**). The Tafel slopes of the ACP, CoOOH NLs, and Co₃O₄ NPs were 60, 72, and 74 mV dec⁻¹, respectively, as observed in **Figure 3.2.18**. For a more precise comparison of the activities, we measured the double-layer capacitances (C_{dl}) of the samples to determine the electrochemically active surface area of the catalysts using CV. **Figure 3.2.19** shows the double-layer charging j differences ($\Delta j = j_a - j_c$ at 1.05 V vs. reversible hydrogen electrode (RHE)) of the catalysts with respect to the scan rate. The slope of the plot is proportional to C_{dl} , which provides an information of the relative surface area. C_{dl} of the CoOOH was larger than that of ACP or the Co₃O₄ NPs in **Figure 3.2.19**. Therefore, it can be deduced that the higher j of ACP does not originate from the high surface area but is instead related to the intrinsically improved catalysis, which will be discussed in the following section.

Furthermore, a long-term stability test under a constant j of 10 mA cm^{-2} revealed that ACP maintains a constant voltage for 24 h with only a slight increase from 1.60 to 1.66 V (see **Figure 3.2.20**).

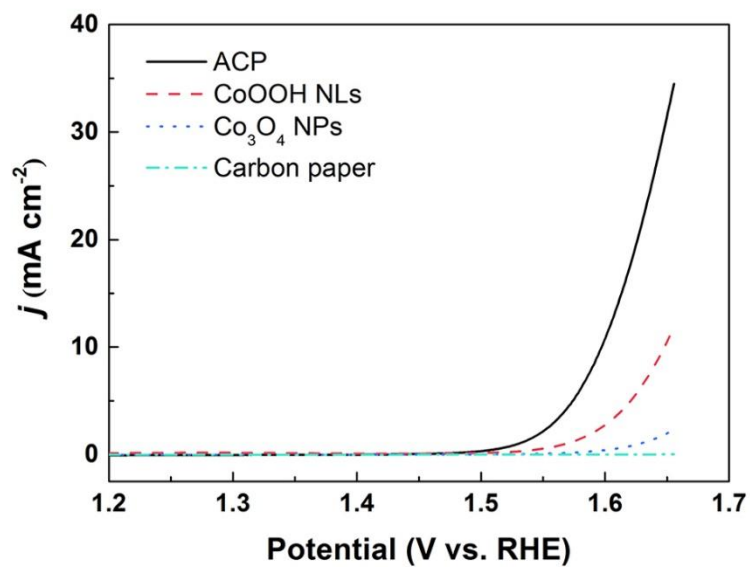


Figure 3.2.12. *iR*-corrected polarization curves in 1 M KOH at a scan rate of 10 mV s⁻¹.

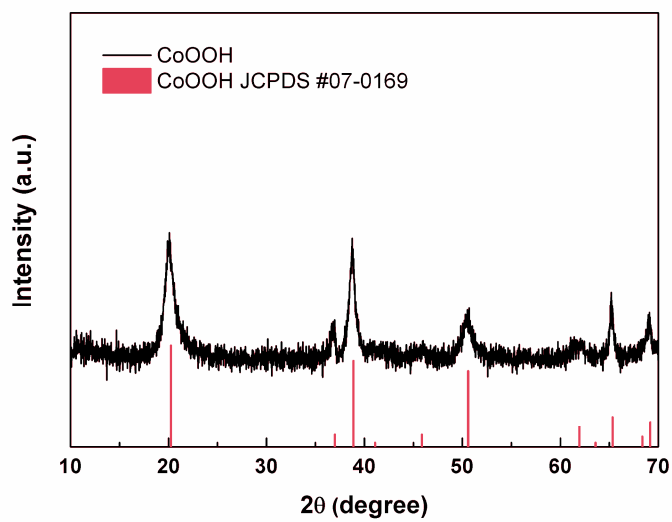


Figure 3.2.13. Powder XRD pattern of the CoOOH nanoplates.

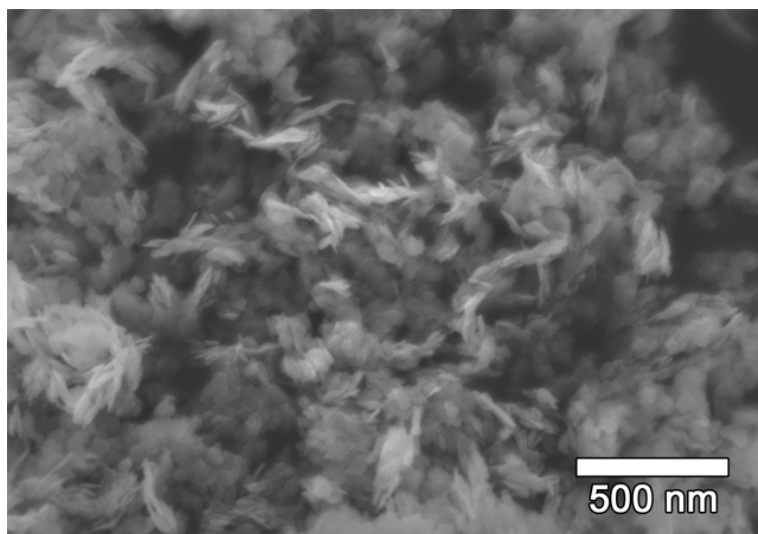


Figure 3.2.14. SEM image of the CoOOH nanoplates.

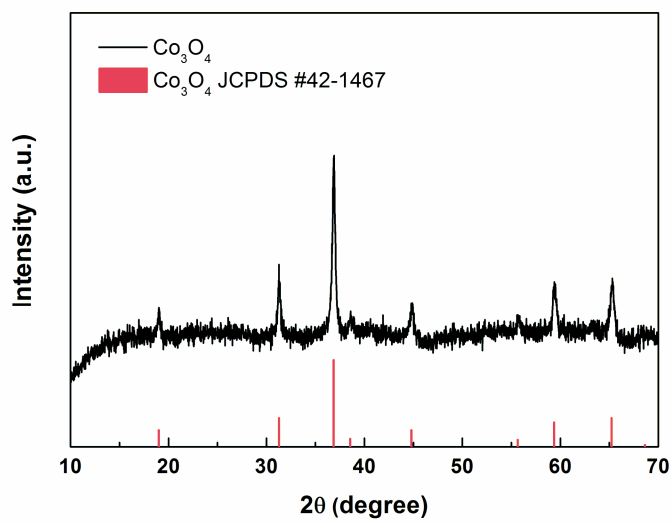


Figure 3.2.15. Powder XRD pattern of the Co₃O₄ nanoparticles.

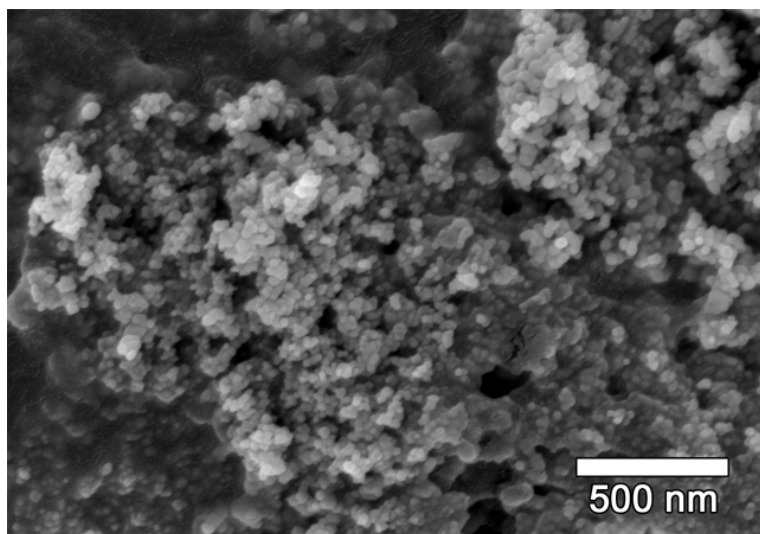


Figure 3.2.16. SEM image of the Co₃O₄ nanoparticles.

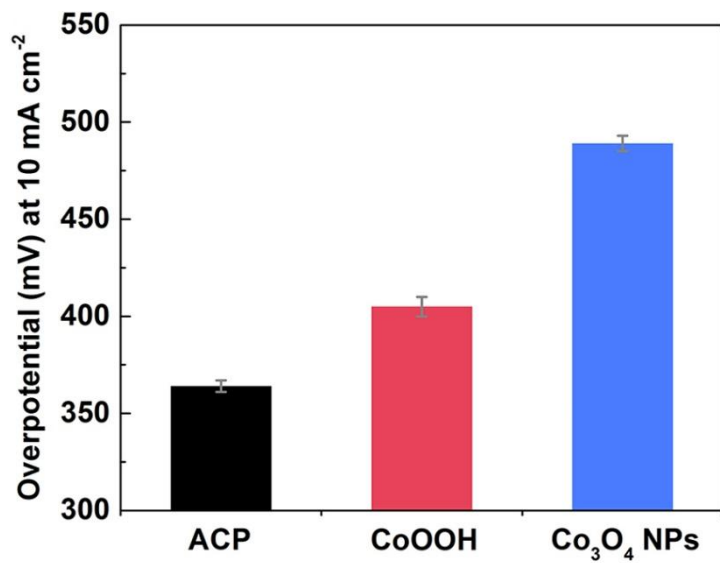


Figure 3.2.17. OER η required for $j = 10 \text{ mA cm}^{-2}$.

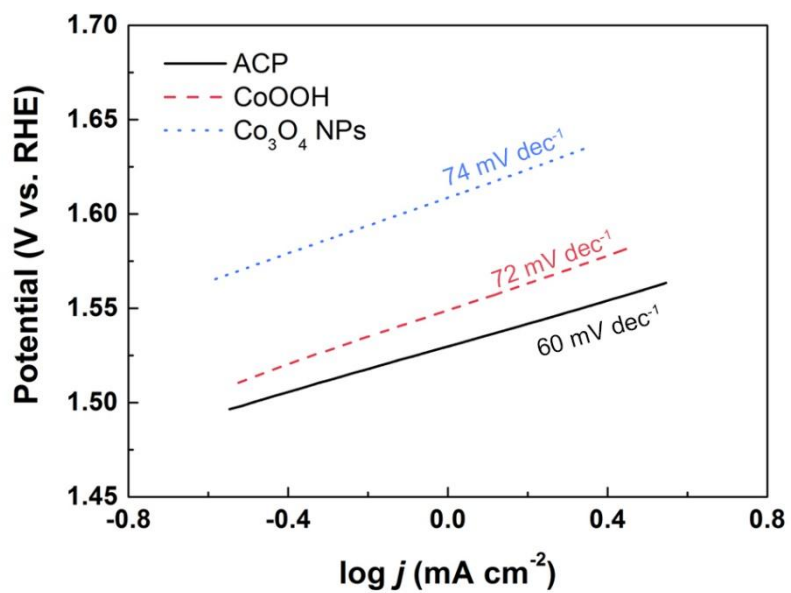


Figure 3.2.18. Tafel plots in 1 M KOH at a scan rate of 10 mV s⁻¹.

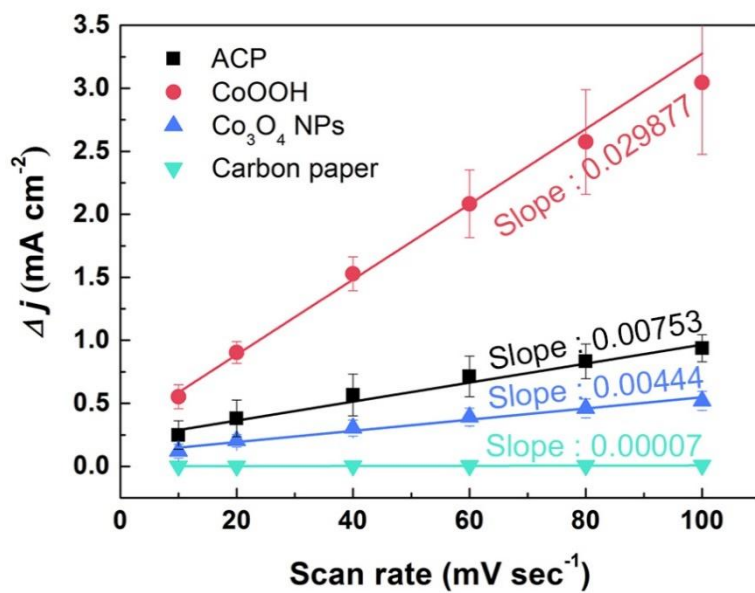


Figure 3.2.19. $\Delta j = j_a - j_c$ at 1.05 V vs. RHE as a function of the scan rate to evaluate C_{dl} .

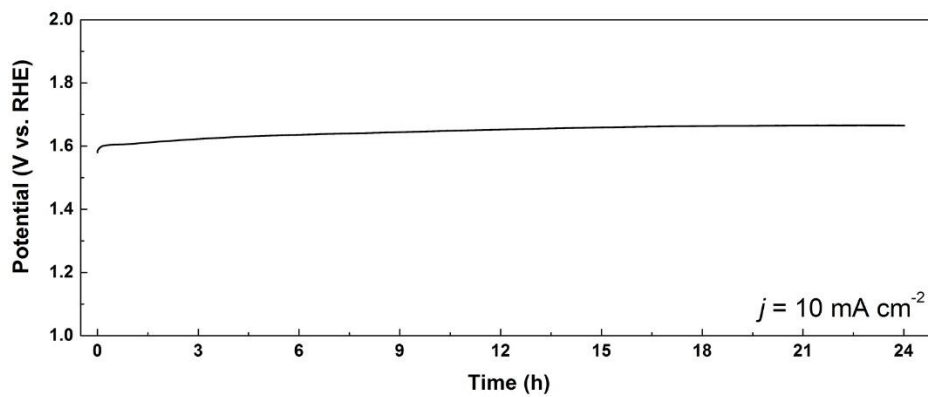


Figure 3.2.20. Long-term stability of ACP at $j = 10 \text{ mA cm}^{-2}$ for 24 h.

2.3.3 Oxidation state and local structure of ACP

X-ray absorption fine structure (XAFS) analysis was performed before and after the electrolysis to probe the local structure of the catalyst during the electrolysis. In **Figure 3.2.21**, the edge position in the X-ray absorption near edge structure (XANES) of the as-prepared ACP indicates that the initial oxidation state of the Co ion was 2+, which is consistent with that of the Co(II)O reference. However, the value shifts toward a higher energy close to that of the LiCo(III)O₂ reference after the electrolysis, indicative of the presence of Co³⁺ in the ACP with irreversible electrochemical oxidation. The irreversible oxidation of Co ions in the ACP was expected to be accompanied by permanent changes in the crystal structure. Thus, the structure of the ACP was further investigated using extended X-ray absorption fine structure (EXAFS) analysis, which is effective for probing the local structural change of amorphous materials.[20-22] **Figure 3.2.22 and 2.3.23** present the k^3 -weighted EXAFS oscillations and Fourier-transform (FT)-EXAFS spectra, respectively, for the as-prepared ACP, ACP after electrolysis, and CoOOH. Note that the x-axis in the FT-EXAFS spectra is the apparent distance, which is shorter than the real distance because the phase shift was not considered. Both figures indicate that the local structure of the ACP becomes analogous to that of CoOOH after the electrolysis. The FT-EXAFS spectra in **Figure 3.2.23** display two notable peaks: peak I and II, which are attributable to the Co–O and Co–Co shell, respectively, as indicated by the EXAFS fits (vide infra). These peaks are

located at 1.6 and 2.8 Å for the as-prepared ACP and shift to 1.5 and 2.5 Å, respectively, after the electrolysis. This finding suggests that the irreversible oxidation reaction during the electrolysis causes structural contraction because of the smaller ionic size of Co^{3+} . For more quantitative analysis, the spectra of the samples were fitted to EXAFS calculations considering the Si incorporation in the Co-based layered hydroxide structure, as shown in **Figure 3.2.24**, **Table 3.2.5**, and **Figures 3.2.25 and 3.2.26**. Notably, the fitting with the consideration of the silicate layers in the ACP (red line in **Figure 3.2.24**) provided a much better result than that without the Si (blue line). In particular, the shoulder region at approximately 2.8 Å in the fitted FT-EXAFS spectrum could not be accounted for using the model similar to CoOOH . However, the Co–Si bonding introduced by the silicate layers in the ACP successfully generated a broad peak in the region, which supports the presence of silicate layers remaining after the electrolysis, distinguishing the local environment of Co in the ACP from that in CoOOH .

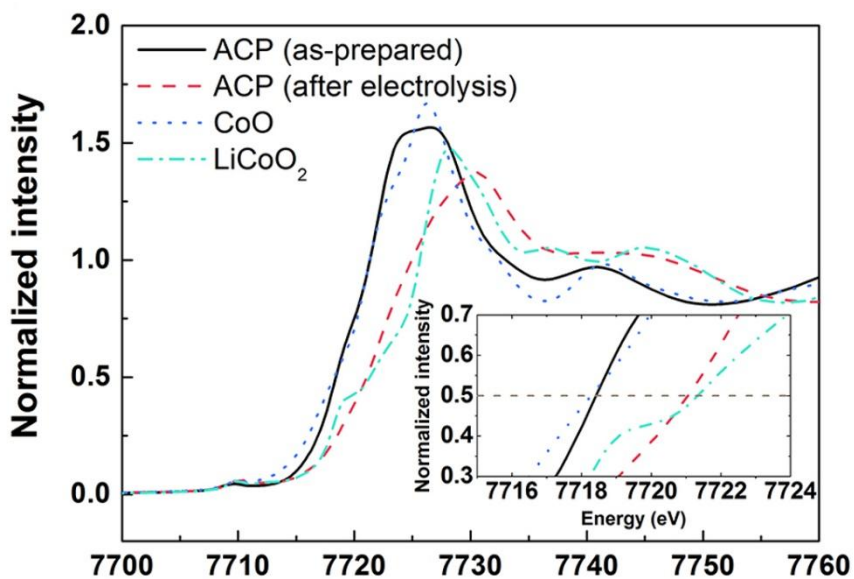


Figure 3.2.21. XANES Co K-edge spectra of the as-prepared ACP and ACP after 1st CV. For comparison, the spectra of CoO and LiCoO₂ are also shown for reference samples of Co²⁺ and Co³⁺, respectively.

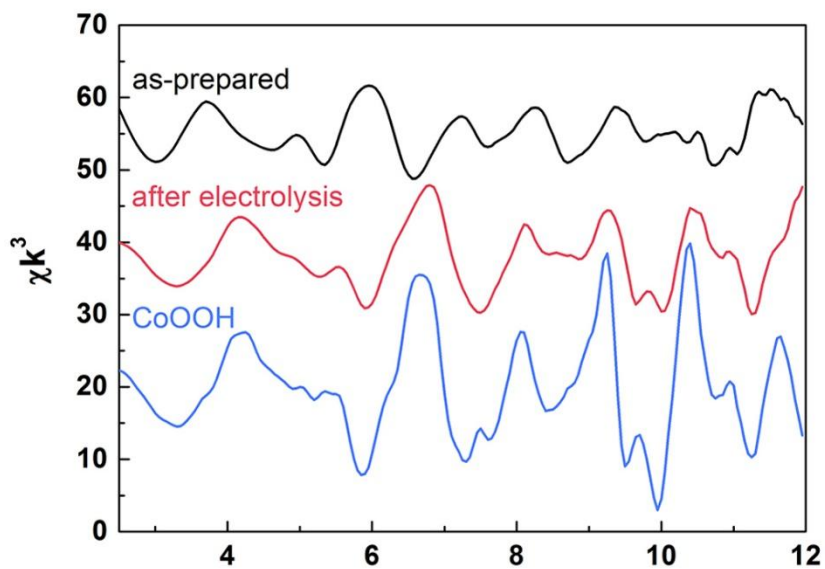


Figure 3.2.22. Oscillations of the EXAFS spectra of the as-prepared ACP, ACP after electrolysis, and CoOOH.

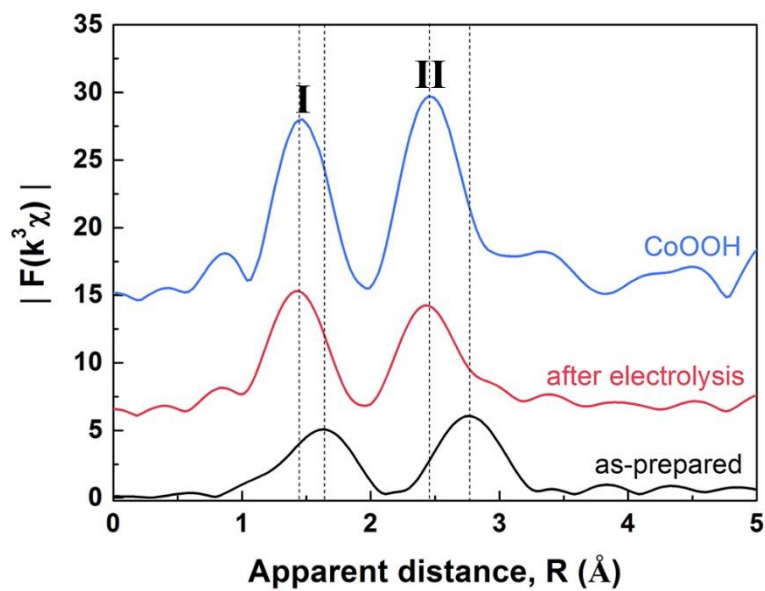


Figure 3.2.23. k^3 -weighted FT-EXAFS spectra of the as-prepared ACP, ACP after electrolysis, and CoOOH.

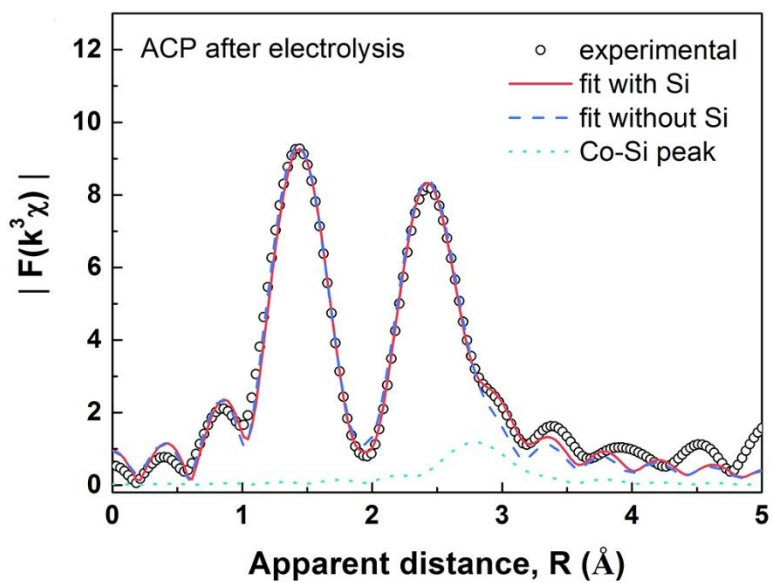


Figure 3.2.24. Comparison of experimental FT-EXAFS spectrum (dotted line) of the ACP after electrolysis and theoretical fit (red line).

Table 3.2.5 Structural parameters of the theoretically fitted FT-EXAFS spectra.

Co K edge	Co-O			Co-Co			Co-Si		
	N	d (Å)	σ^2 (Å ²)	N	d (Å)	σ^2 (Å ²)	N	d (Å)	σ^2 (Å ²)
As-prepared	5.1	2.089	0.009	5.4	3.13	0.011	2.4	3.41	0.006
ACP	(8)	(6)	(1)	(8)	(1)	(1)	(2)	(2)	(3)
After	5.0	1.893	0.004	5.0	2.826	0.006	2.0	3.296	0.007
electrolysis	(9)	(1)	(1)	(6)	(6)	(1)	(4)	(14)	(2)
CoOOH	6.0	1.898	0.003	6.0	2.853	0.003			
	(7)	(6)	(1)	(7)	(6)	(1)			

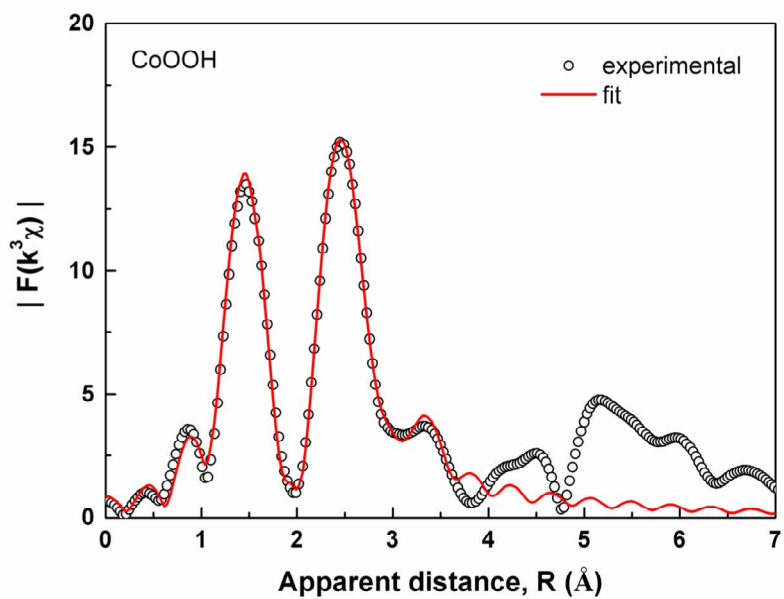


Figure 3.2.25. Comparison between experimental FT-EXAFS spectrum of the CoOOH nanoplates (dotted line) and theoretical fit (red line).

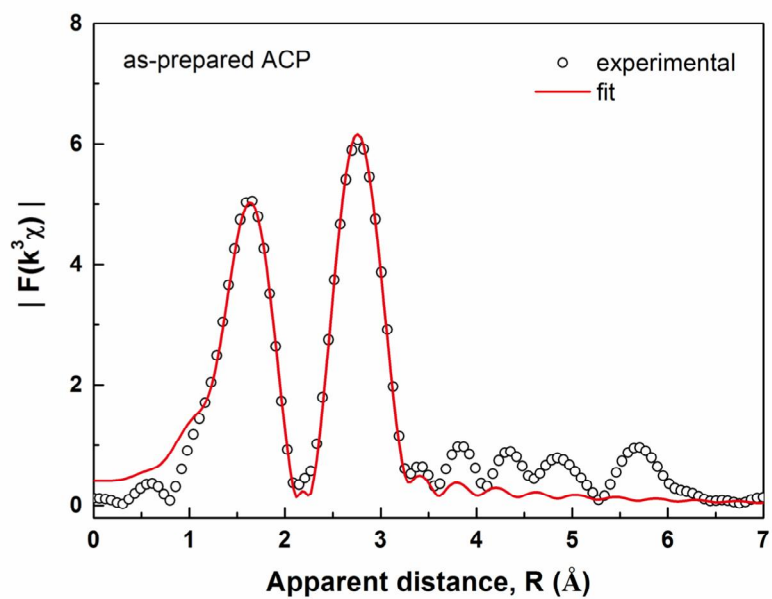


Figure 3.2.26. Comparison between experimental FT-EXAFS spectrum of the as-prepared ACP (dotted line) and theoretical fit (red line).

2.3.4 Slab modeling for DFT calculation

To understand the role of the silicate in the catalytic reaction at an atomistic level, we comparatively investigated the OER thermodynamics of CoOOH and ACP using DFT calculations. There are two major structural differences between the surface of CoOOH and the ACP: the interlayer distance and the diversity of the surficial reaction sites. **Figure 3.2.27-3.2.30** compares the surficial atomic geometries of CoOOH (**Figure 3.2.27, 3.2.29**) and ACP (**Figure 3.2.28, 3.2.30**) in the OER operating voltage range. We closely examined the (10 $\bar{1}$ 4) surface of CoOOH because it is known to be the most OER-active surface for cobalt hydroxides according to the previous work by Bell *et al.*[82] In a comparative study of the ACP, we also probed the equivalent ACP surface, which has a similar atomic arrangement as that of CoOOH (10 $\bar{1}$ 4) (see **Figures 3.2.31-3.2.34** for the detailed surface cleavage procedure) because of the structural similarity of CoOOH and ACP. The local structural difference between the surfaces of CoOOH and ACP can be easily observed in **Figure 3.2.27 and 3.2.28** in terms of the interlayer bonding nature. The two CoO₆ layers in CoOOH share hydrogen atoms via hydrogen bonding between the layers, which enables the CoO₆ layers to closely bond with each other (see **Figure 3.2.27**). In contrast, large silicate polyanions are present between the two CoO₆ layers and do not allow the hydrogen bonding leading to a longer interlayer distance in the ACP (see **Figure 3.2.28**). Therefore, the interaction between the Co layers in the ACP is generally weaker

than that in CoOOH. The diversity of the surficial reaction sites in the surficial difference between ACP and CoOOH should also be noted. **Figure 3.2.29** depicts the oxygen reaction sites on the surface of CoOOH. There are only two types of active sites on the surface considering the symmetry of the CoOOH crystal: the on-top site of a single 5-fold coordinated Co ion (terminal site, denoted as O_t) and the bridge di- μ -oxo site between two 5-fold coordinated Co ions (bridge site, denoted as O_b). However, the ACP surface can have various active sites because of the introduction of silicate termination, as demonstrated in **Figure 3.2.30** (top view of the surface). In particular, silicate groups that are bound to some of the oxygen sites result in many distinct environments around the active sites. Consequently, the ACP surface contains surficial oxygen sites with local environments, *e.g.*, the terminal 1 site with OH₂ configuration (denoted as O_{t1}), terminal 2 site bound with silicate (denoted as O_{t2}), bridge 1 site (denoted as O_{b1}) and bridge 2 site (denoted as O_{b2}) in **Figure 3.2.30**. Note that there are also terminal 3, terminal 4, bridge 3, and bridge 4 sites present in the ACP that are not explicitly represented in **Figure 3.2.30** (see **Figure 3.2.34**).

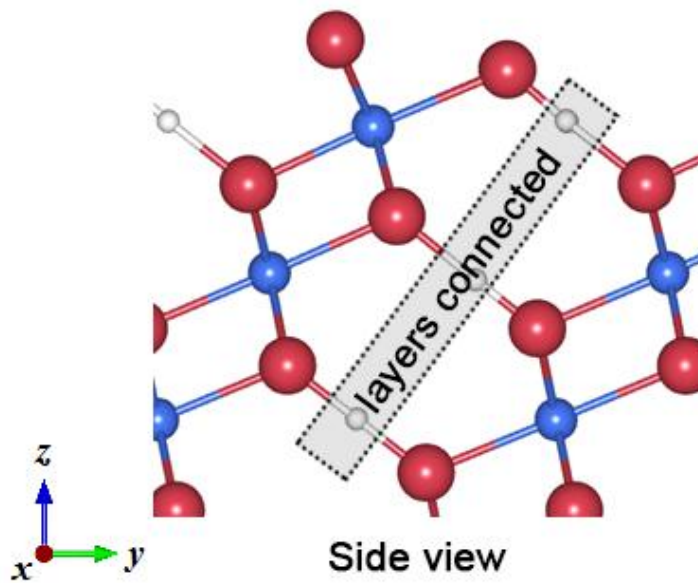
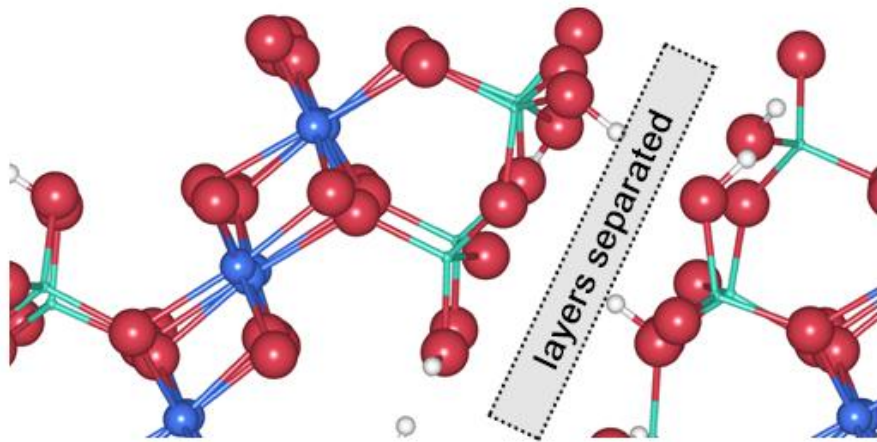


Figure 3.2.27. Side view of CoOOH (10 $\bar{1}$ 4) surface, which is the most active surface for the OER.



Side view

Figure 3.2.28. Side view of CoOOH surface with similar atomic configuration as the CoOOH ($10\bar{1}4$) surface. The ACP surface has a longer interlayer distance than the CoOOH surface.

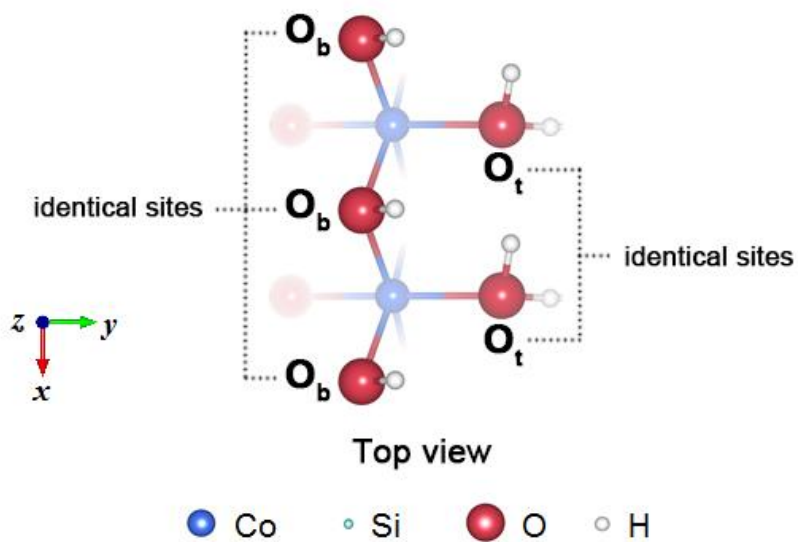


Figure 3.2.29. Top view of active surface of CoOOH, showing active sites for the OER. Co, Si, O, and H are represented by blue, green, red, and white spheres, respectively. For improved clarity, only the topmost atoms are shown.

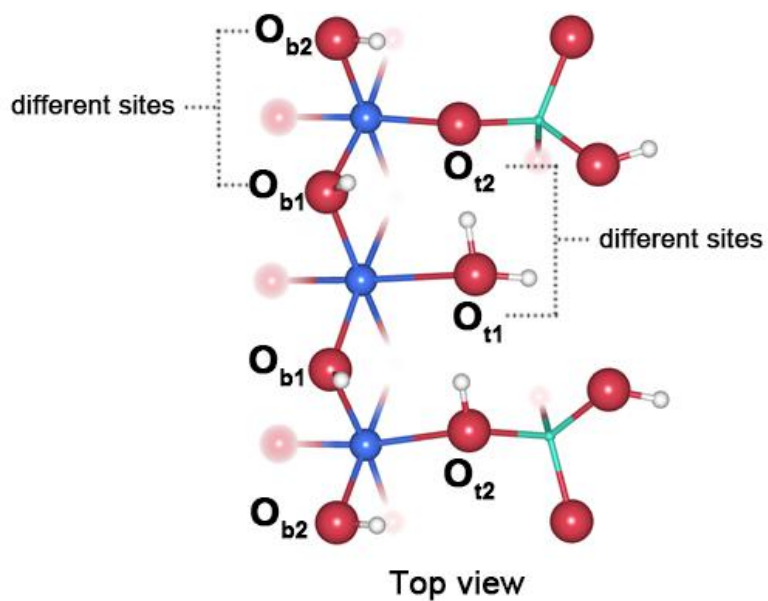


Figure 3.2.30. Top view of active surface of ACP, showing active sites for the OER. For improved clarity, only the topmost atoms are shown.

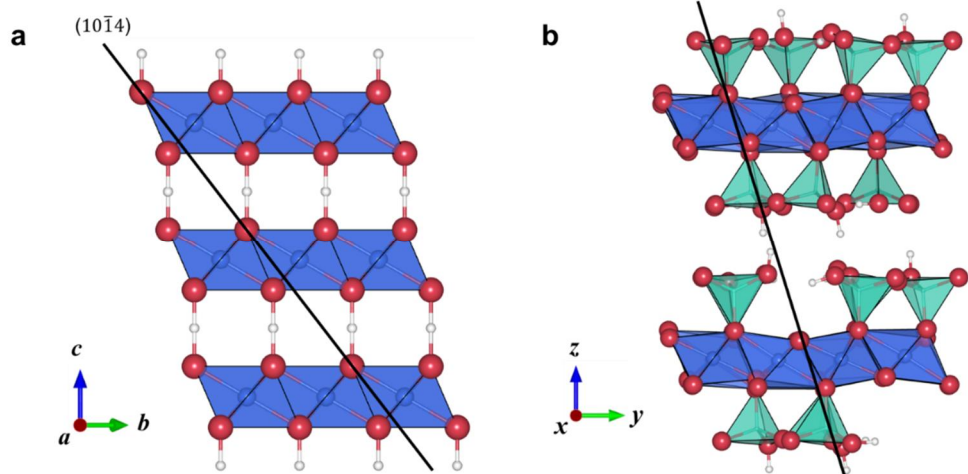


Figure 3.2.31. Crystal structure of (a) CoOOH and (b) ACP; the cleavage lines are shown in black. Note that the $(10\bar{1}4)$ surface is the most OER-active surface from CoOOH. The cleavage line for ACP has a similar atomic configuration as the CoOOH $(10\bar{1}4)$ surface, and the silicate tetrahedron is preserved.

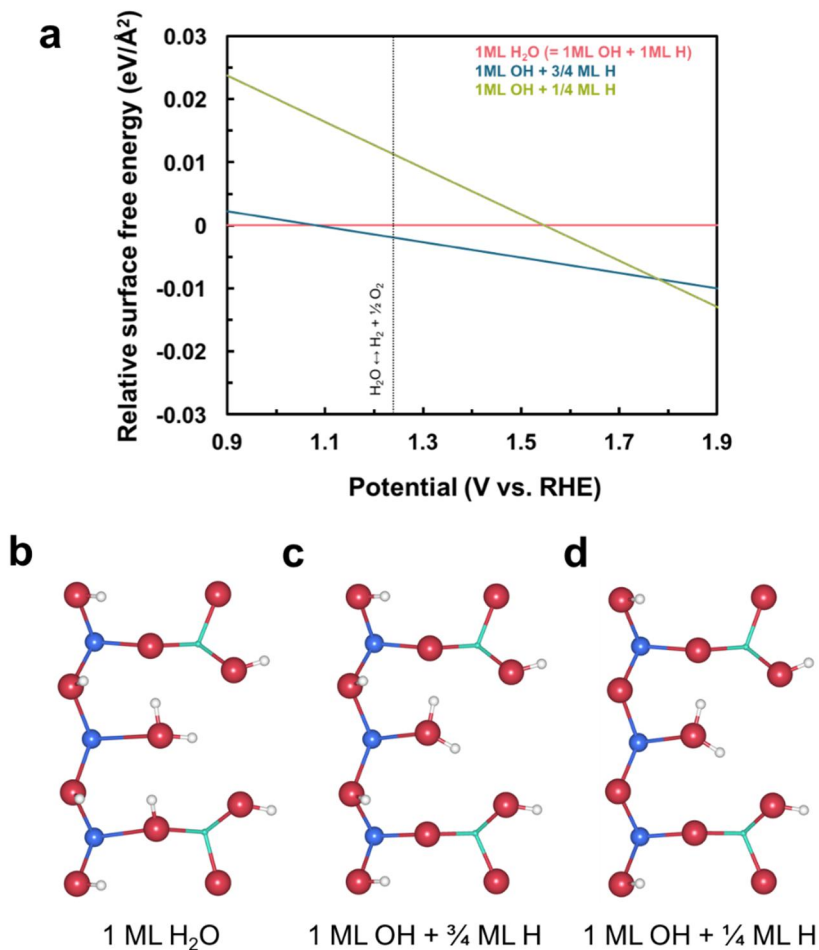


Figure 3.2.32. Surface termination of the ACP surface (model 1) corresponding to the potential. (a) Surface phase diagram as a function of applied potential for ACP surface model. Stable surface structures with adsorbates corresponding to applied potential with: (b) 1 monolayer (ML) of co-adsorbed H₂O (below 1.1 V), (c) 1 ML of OH and 3/4 ML of H (from 1.1 to 1.8 V), and (d) 1 ML of OH and 1/4 ML (above 1.8 V). For improved clarity, only the topmost atoms are shown.

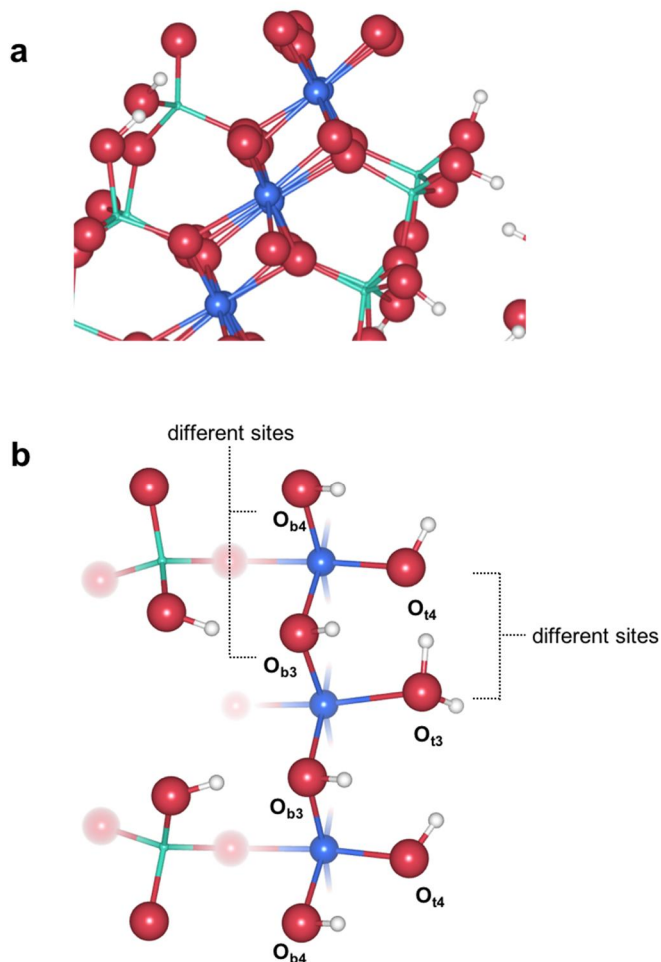


Figure 3.2.33. Surface structures of another surface of the ACP model (model 2). Unlike the ACP surface model, silicates are adsorbed at the bridge site rather than the terminal site. (a) Side view of the CoOOH surface with similar atomic configuration as the CoOOH ($101\bar{4}$) surface. (b) Top view of the active surface of ACP showing the active sites for the OER. Co, Si, O, and H are represented by blue, green, red, and white spheres, respectively. For improved clarity, only the topmost atoms are shown.

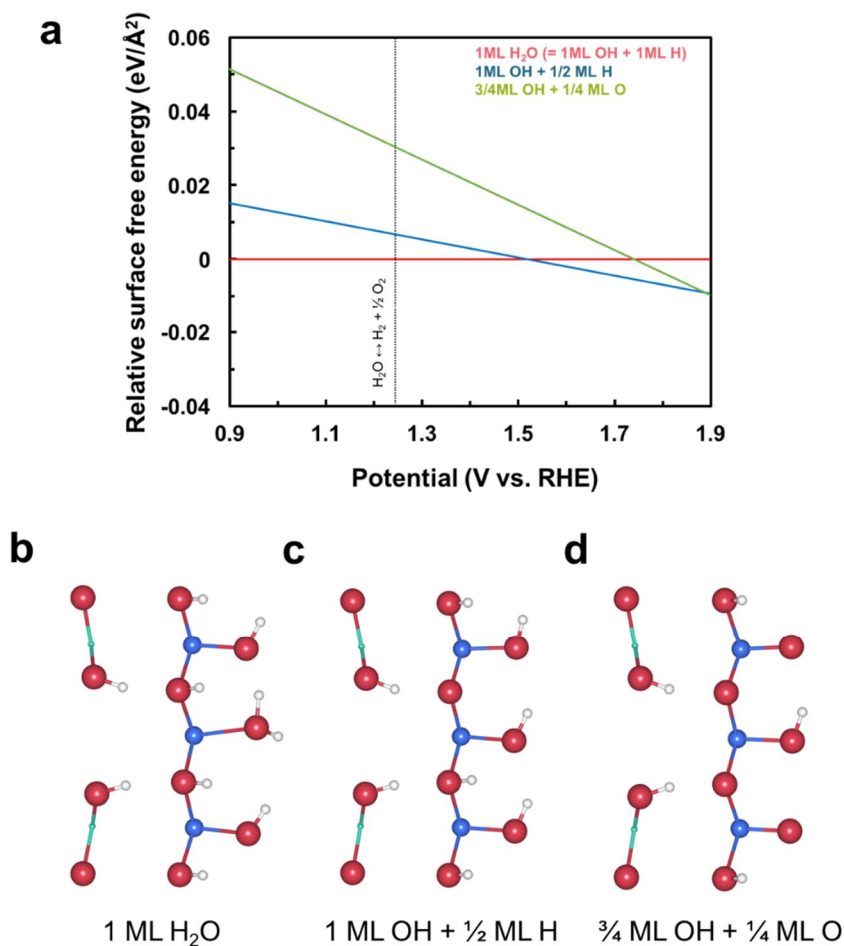


Figure 3.2.34. Surface termination of another ACP surface (model 2) corresponding to the potential. (a) Surface phase diagram as a function of applied potential for the ACP surface model. Stable surface structures with adsorbates corresponding to applied potential with: (b) 1 ML of co-adsorbed H₂O (below 1.1 V), (c) 1 ML of OH and 3/4 ML of H (from 1.1 to 1.8 V), and (d) 1 ML of OH and 1/4 ML (above 1.8 V). For improved clarity, only the topmost atoms are shown.

2.3.5 OER thermodynamics

The first-principles calculations revealed that the distinct local environment induced by silicate groups on the ACP surface significantly regulates the catalytic activity of each active reaction site. **Figure 3.2.35** shows the theoretical η for the OER occurring at various active sites on the ACP and CoOOH surfaces. At a glance, the range of η for the OER becomes more diversified for the ACP compared with the two values for CoOOH. Most interestingly, the bridge 1 site on the ACP surface exhibits a much lower η (340 mV) than other sites in the ACP and those in the CoOOH.[79] Even though other active sites in the ACP exhibit comparable or higher η compared with those of CoOOH, the existence of the most reactive site with the lowest η , *i.e.*, the bridge 1 site in the ACP, implies that the overall OER reaction can be more facilitated in the ACP. Along with the terminal 4 site (541 mV), the bridge 1 site would serve as a major reaction site in the electrolysis of the ACP. To understand the enhanced catalytic activity at the bridge 1 site, the OER energies were closely examined. **Figure 3.2.36** compares the free energy landscape of the OER occurring at the bridge 1 site on the ACP surface (black line) with that of the OER occurring at the bridge site (cyan line) and terminal site (blue line) on the CoOOH surface. Note that standard conditions ($T = 298.15$ K, $P = 1$ bar, and $\text{pH} = 0$) and the thermodynamic equilibrium potential for water oxidation (1.23 V vs. RHE) were assumed in these calculations. The OER cycle in **Figure 3.2.36** is divided into four electrochemical hydrogen abstraction

steps. The third step (*i.e.*, the OOH* formation step) is the potential-limiting step for the OER at the bridge 1 site on the ACP surface. Note that the OOH* formation step was similarly observed to be the potential-limiting step for the active sites on the CoOOH surface, in agreement with a previous study.[82] This finding may imply that the structural similarity between the CoOOH and ACP leads to analogous catalytic mechanisms. However, much more stable OOH* adsorption is observed for the bridge 1 site on the ACP surface than on the CoOOH surface, which results in a much lower theoretical η .

The origin of this stabilization can be rationalized based on the structural flexibility of the ACP surface. **Figures 2.3.37 and 2.3.38** show the atomic configurations around the active sites for the O* intermediate (left panel) and OOH* intermediate (right panel) for the bridge 1 sites on the ACP and CoOOH surfaces for comparison, respectively. One notable difference in the OOH* intermediate structure of the ACP is that an additional O–H bonding is produced, as denoted by the red circle. Initially, the H1 is mainly bound with the O1 and has a relatively weak bonding with O2 for both ACP and CoOOH (left panels of **Figure 3.2.37 and 3.2.38**). However, when the OOH* intermediate structure is formed, the H1–O2 bond distance becomes significantly shortened for ACP (1.81 \rightarrow 1.68 Å), resulting in stronger O–H bonding,[80] whereas that of CoOOH remains almost unchanged (1.79 \rightarrow 1.78 Å). The overall energy of the ACP can be significantly reduced with the additional hydrogen bonding present in the OOH* intermediate structure. This structural difference is attributable to the lack of interlayer O–H–O

bonds in the phyllosilicate, which offers flexibility to the motion of the OH₂ group. In the CoOOH, the interlayer O–H–O hydrogen bonds are present between the layers (see O1–H2–O3 bond in **Figure 3.2.38**); thus, the oxygen position is relatively fixed. However, the oxygen atoms are free from bonding with the layer below because of the presence of the silicate layers, which facilitates the adjustment of their positions upon the structural change. The stabilization of the ACP with the flexible oxygen motion that can induce the additional O–H bonding reduces the energy of the OOH* intermediate at the bridge 1 site on the ACP surface, consequently leading to the low η in the overall OER reaction.[81] These results suggest that the presence of the interlayer polysilicate between Co layers in the ACP modulates the active site reactivity, thereby affecting the OER thermodynamics.

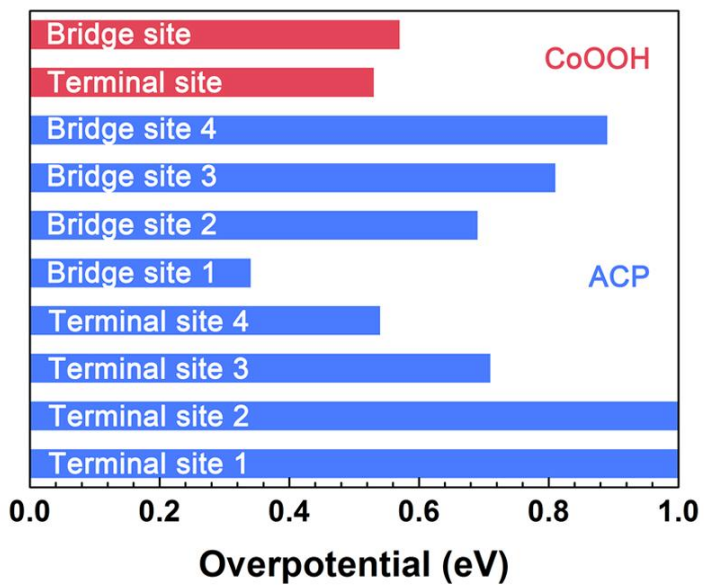


Figure 3.2.35. Theoretical η for OER of plausible sites. Some bridge sites on the ACP surface show much lower η than the active sites of CoOOH.

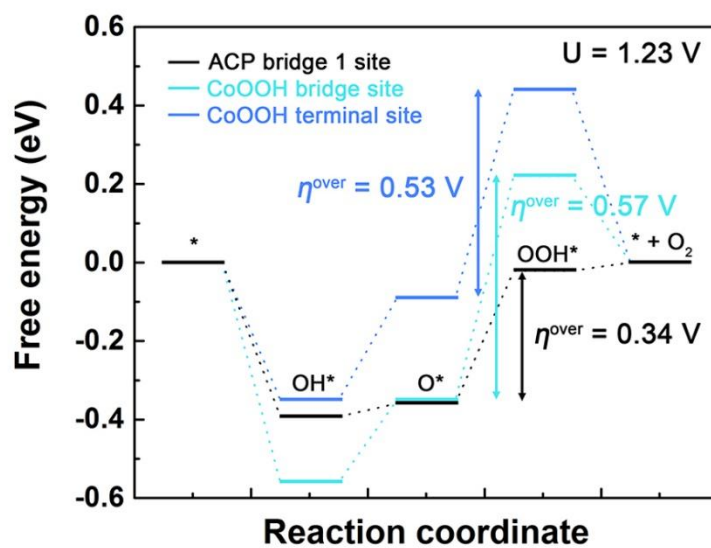


Figure 3.2.36. Free energy landscape for OER at 1.23 V (ideal potential for OER). The black, cyan, and blue lines indicate the free energy of the ACP bridge 1 site, CoOOH bridge site, and CoOOH terminal site, respectively.

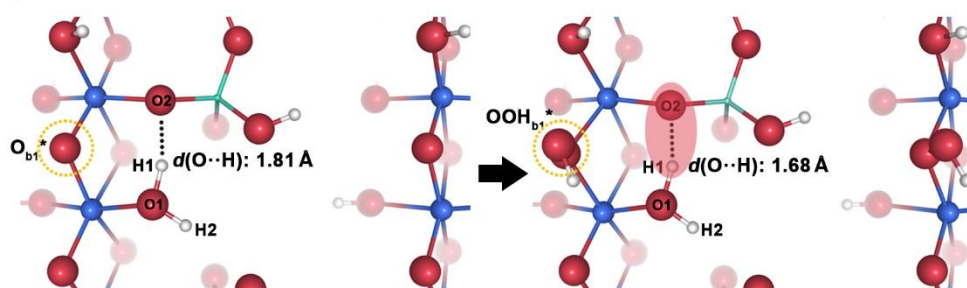


Figure 3.2.37. Comparison of the structures for the OOH^* formation step (rate-determining step for these cases) at the ACP bridge 1 site. Reaction sites and hydrogen bonds are indicated with yellow and red circles, respectively. Further adjustment of the bond length at the ACP surface reduces the OER η .

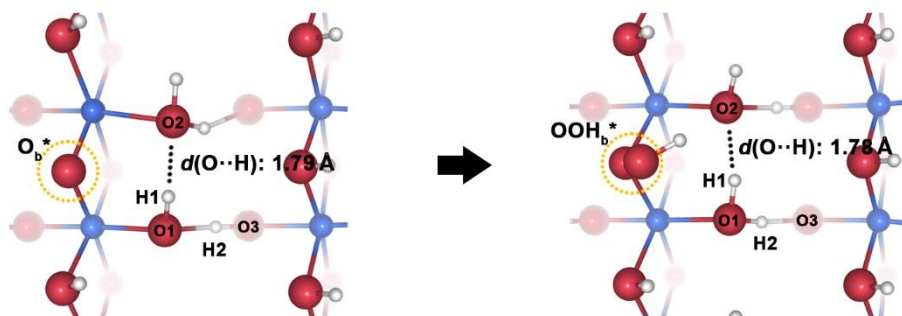


Figure 3.2.38. Comparison of the structures for the OOH^* formation step (rate-determining step for these cases) at the CoOOH bridge site.

2.4 Conclusion

In summary, we reported earth-abundant layered phyllosilicate materials as efficient OER catalysts for water splitting for the first time. The ACP introduced in this study could be prepared by a simple room-temperature synthesis and exhibited the general nature of the phyllosilicate as well as superior OER catalytic activity compared with that of other Co-based catalysts. Our DFT calculations on the OER mechanism suggested that the silicate component – the redox-inactive part in the ACP – aided in substantially reducing the η of the catalytic active sites by modulating the local structure. Furthermore, the structural flexibility induced by the polysilicate between the Co layers in the layered framework could stabilize the OOH* formation step in the ACP. This formation step is the potential-limiting step of the overall OER mechanism; thus, the OER activity could be further enhanced. We believe that these findings concerning this new group of catalyst materials with unexpected chemistry will be helpful for further investigations of efficient catalysts with high performance and will provide insight for the design of layered OER catalysts by the structural modulation.

Chapter 3. Activation of Reaction Sites in Amorphous Cobalt Iron Phyllosilicate for the Efficient Oxygen Evolution Reaction

3.1. Introduction

Energy demand is continuously increasing due to industrial development and population growth, however, fossil fuel based energy has problems such as CO₂ emission, fuel depletion. Therefore, many renewable energy has been developed, among which hydrogen energy is attracting attention because it has abundant, environmentally friendly and high energy density. Artificial photosynthesis, a water-splitting system using solar-to-chemical conversion, is the most environmentally friendly and efficient method.[34, 35, 37, 39] However, the oxygen evolution reaction (OER), which is a half reaction of the overall water splitting reaction, determines the rate of the whole reaction because the four electrons are involved and O-O bond formation is difficult. Therefore, the development of OER catalyst is the most important in the hydrogen energy field and tremendous researches are directed to it.

Many 3d transition metal-based catalysts (Mn,[14, 50, 55, 65, 66, 69, 93] Fe,[52, 94] Co,[13, 15, 16, 95-100] Ni,[21, 49, 54, 64, 101-104] and Cu[105-108])

with comparable performance to conventional precious metal based catalysts in alkaline electrolyte have been developed, but still require improved properties for industrial applications. In recent years, many studies have been carried out to apply multiple metal elements in various materials to overcome the limitations of single metal based catalysts.[29, 31, 32, 103, 109-112] In particular, the researches about synergistic effect by multiple metal application in layered double hydroxide (LDH) and amorphous materials have been extensively progressed. Several combinations of transition metal compositions have been reported, but the addition of Fe to Ni and Co based catalysts showed a dramatic increase in OER performance.[25, 27, 29, 31, 113] Trotochaud *et al.* reported that the catalytic activity of the $\text{Ni}_{1-x}\text{Fe}_x\text{OOH}$ OER electrocatalyst film increases when intentionally or coincidentally Fe incorporates Ni site.[27] They concluded that they are consistent with the hypothesis[114] that the Ni center is activated through a partial-charge-transfer mechanism induced by Fe through the TOF value. Friebe *et al.* showed that Fe was present in the MO_6 octahedral site in the NiFeOOH electrocatalyst using X-ray absorption spectroscopy (XAS), and they established that Fe ion in the NiOOH host exhibited lower overpotential than Ni ion from DFT calculation.[27] Much research has been reported on binary materials consisting of Co and Fe ions as well as Ni and Fe. The effects of Fe addition in Co based catalysts were very similar to those in Ni based catalysts. Burke *et al.* found that the incorporation of Fe resulted in a catalytic activity increase of CoOOH over 100 fold, suggesting that CoOOH could act as a conductive host and that Fe could act as an active site.[31] Yang *et*

al. confirmed the synergistic effect of Co and Fe when the incorporation of Al and Fe ion into $\text{Co}(\text{OH})_2$ improves OER performance only in Fe-incorporated $\text{Co}(\text{OH})_2$. [95]

It is important to have insight into the reaction mechanism in order to design an efficient catalyst with synergistic effects of the elements. To obtain clear understanding about this effect, experimental studies and first principle calculation studies have attempted to identify the role of each element. Since the OER is greatly influenced by the local structure of the site where the reaction occurs, XAS is the most commonly used method for analyzing local structure. [15, 27, 29, 95] Rapid conversion between the steps during OER makes it hard to analyze the chemical state, leading to the limitation of ex-situ analysis. Therefore, many studies have been devoted to the mechanisms study by in-situ analytical instruments such as Raman spectroscopy, Fourier-transform infrared spectroscopy (FT-IR), Mössbauer spectroscopy, XAS, and differential electrochemical mass spectrometry (DEMS). [29, 113, 115-119] In addition, researches to find an active site based on first principle calculation and to predict reaction have been actively carried out. Several DFT calculation researches have reported that Fe can improve the OER catalytic activity because it acts as an active site with lower overpotential in NiFeOOH . [27, 120] On the other hand, Zhang *et al.* recently obtained the O to OH adsorption energy differences used as a descriptor for predicting the activity of the catalyst, and reported the superior performance of the catalyst in practice. [111]

They suggested that tuning of the OER performance is possible by mixing FeOOH with strong OH adsorption energy and WO₃ and CoOOH with weak OH adsorption energy. Despite of these efforts to understand for multiple metal based catalyst, unknown OER chemistries still remain in several parts. Moreover, because the studies are mostly limited to specific materials such as perovskite oxide or LDH, a widening view is needed through research in various materials.

Herein, we introduce the improvement of OER performance in amorphous cobalt phyllosilicate catalyst by introducing Fe ion, named amorphous cobalt iron phyllosilicate (ACFP), and provide the insight into how Fe ion can affect the surrounding OER active sites. The electrochemical test confirmed that the OER performance by Fe incorporation was improved until Fe content reached 40%. In the phase containing Fe, the Tafel slope decreased to ~40 mV dec⁻¹ compared to the pure cobalt phase. Inactive sites having large OER overpotential in pure cobalt phyllosilicate can be newly activated by lowering overpotential in Fe doped cobalt phyllosilicate, as demonstrated by DFT calculation. This finding suggests that inactive reaction sites can be active by introducing new elements and provides an opportunity to broaden the scope of synergistic effect in multiple metal based catalysts.

4.2 Results and discussion

4.2.1 Phase identification of ACFP

The series of ACFP was synthesized by simple coprecipitation reaction from mixing metal chloride (CoCl_2 and $\text{FeCl}_2 \cdot 4\text{H}_2\text{O}$) aqueous solution with Na_2SiO_3 aqueous solution at a room temperature. As shown in **Figure 4.2.1**, all of as-prepared ACFPs show no clear diffraction peak, which indicates the amorphous structure. For a detailed phase analysis of ACFPs, hydrothermally annealed ACFPs were prepared at 180 °C for 24 h. The XRD patterns of annealed ACFPs (**Figure 4.2.2**) are similar to that of as-prepared ACFP, however, clear peaks appear after annealing process, indicating that the more crystalline phyllosilicate are formed. Peaks of annealed ACFPs were well matched with the XRD reference of cobalt phyllosilicate ($\text{Co}_3\text{Si}_4\text{O}_{10}(\text{OH})_2$, #21-0871) and iron phyllosilicate ($\text{Fe}_2\text{Si}_4\text{O}_{10}(\text{OH})_2$, #42-0569). There was no significant difference in the XRD patterns within the annealed ACFP series, but as the Fe content increased, the some peaks, especially near 28° , became sharper. This trend means the phase of the sample is closer to iron phyllosilicate than cobalt phyllosilicate.

To compare the phases of the as-prepared and annealed samples, the local environment of materials were investigated using the Fourier-transform infrared (FT-IR) spectra (**Figure 4.2.3 and 4.2.4**). All of as-prepared ACFP spectra showed a very similar shape. The shoulder peaks at 3600 cm^{-1} corresponds to the O-H

stretching vibration mode (ν_{OH}) of the OH-3M (M: Co or Fe) group and the broad band near 3500 cm^{-1} is due to the adsorbed water molecule. The low wavelength region consists of peaks related to the silicate. The peak at 1000 cm^{-1} is assigned to the Si-O bending vibration mode (δ_{SiO}) and the peak at 660 cm^{-1} is overlapped with peaks corresponding to the Si-O stretching vibration mode (ν_{OH}) and the O-H bending vibration mode (δ_{OH}) of the OH-3M group. In addition, asymmetric Si-O bending vibration mode (δ_{SiO}) appears the peak at 450 cm^{-1} . [89] The spectra of annealed ACFPs were also shown almost same patterns compared to that of as-prepared ACFPs. From the XRD and FT-IR results, it can be concluded that the as-prepared ACFPs exhibit amorphous property, but have the bonding characters of phyllosilicate within a short-range order. The crystal structure of cobalt iron phyllosilicate is schematically illustrated in **Figure 4.2.5**. Phyllosilicate has a layer stacked structure and each layer has a metal hydroxide layer sandwiched by a silicate layer. The edge-sharing MO_6 octahedral constitutes the metal hydroxide layer, and the SiO_4 tetrahedral forms corner-sharing silicate layers.

Figure 4.2.6 and 4.2.7 exhibit the Co and Fe *K*-edge X-ray absorption near edge structure (XANES) spectra of ACFPs. From the same edge position of ACFPs with that of Co(II)O reference, it is obvious that the Co oxidation state of the series of ACFP is 2+. Likewise, the Fe *K*-edge position confirmed that the Fe ion in ACFP was 3+. Quantitative analysis of elemental composition by energy dispersive spectroscopy (EDS) analysis was carried out to analyze whether

precipitation reaction was predominantly caused by specific elements of Co and Fe. Co/Fe ratios of ACFPs are consistent with that of precursor ratios from **Figure 4.2.8**. Therefore, it can be seen that the preferred metal in the precipitation reaction does not exist and is synthesized evenly. In addition, the atomic ratios of M:Si:O in the series of ACFPs exhibited approximately 1:1:4 as shown in **Table 4.2.1**.

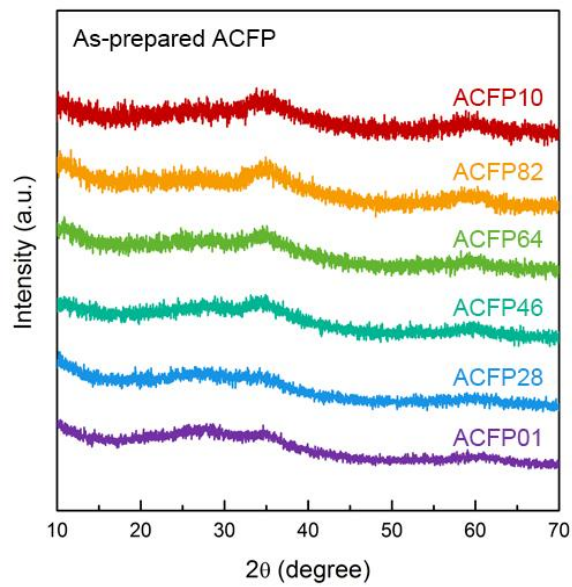


Figure 4.2.1. Powder XRD patterns of the series of as-prepared ACFPs.

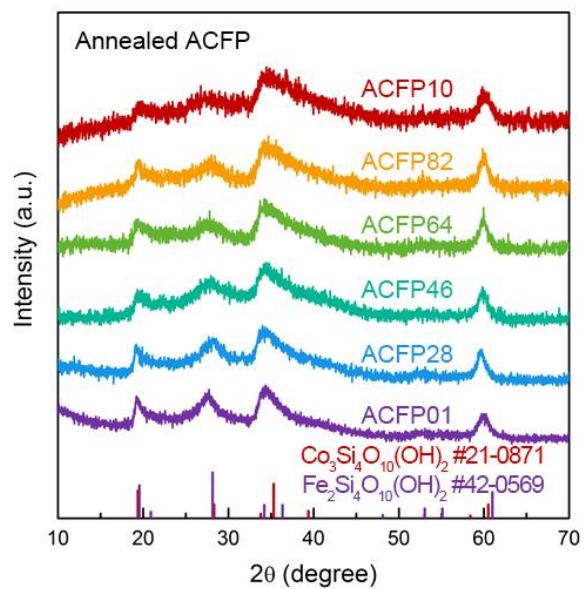


Figure 4.2.2. Powder XRD patterns of the series of annealed ACFPs after hydrothermal treatment.

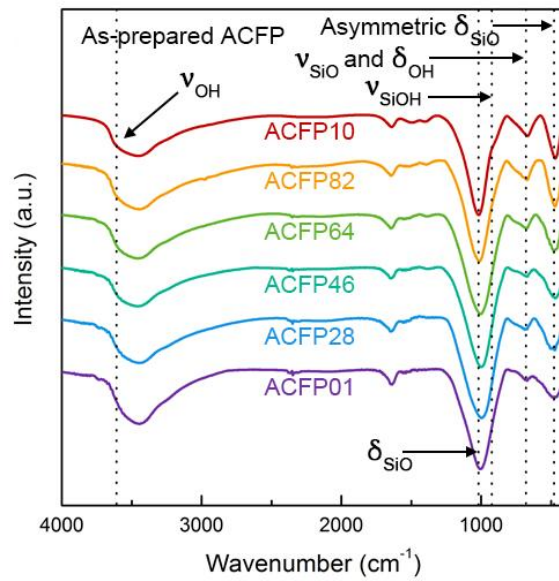


Figure 4.2.3. FT-IR spectra of as-prepared ACFP.

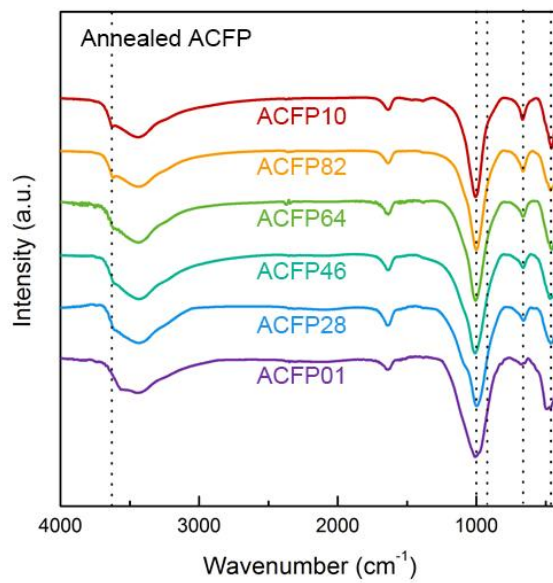


Figure 4.2.4. FT-IR spectra of annealed ACFP after hydrothermal treatment.

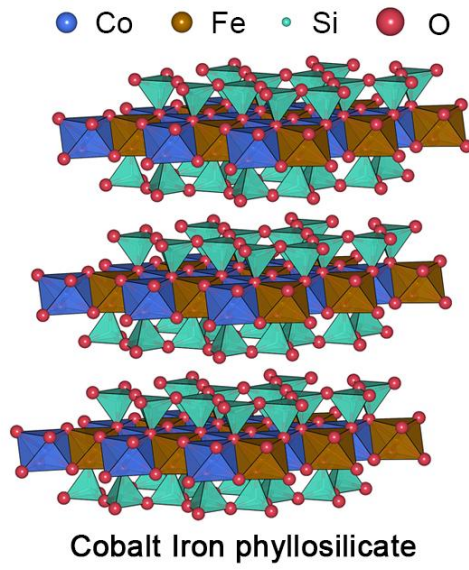


Figure 4.2.5. Schematic illustrated crystal structure of cobalt iron phyllosilicate.

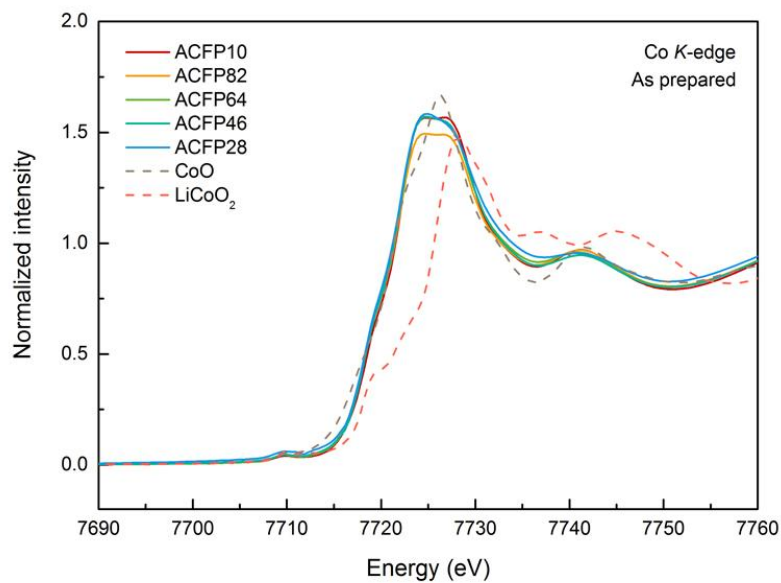


Figure 4.2.6. XANES Co *K*-edge spectra of the series of as-prepared ACFP. For comparison, the spectra of CoO, and LiCoO₂ are shown for reference samples of Co²⁺, and Co³⁺, respectively.

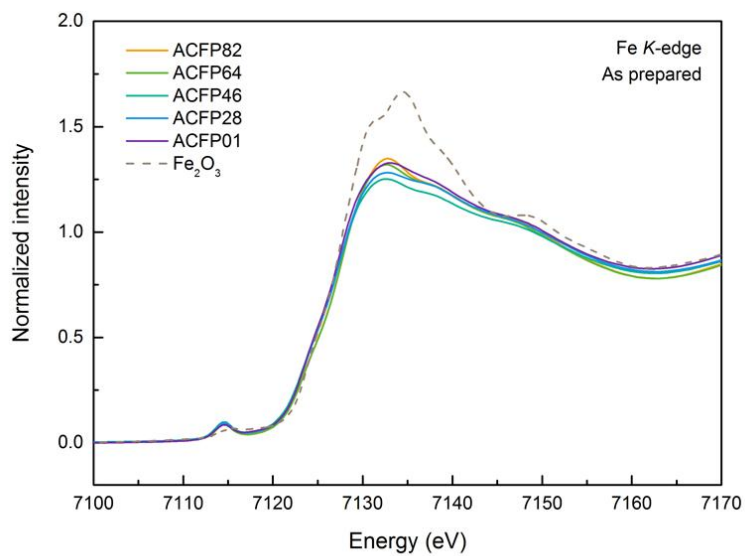


Figure 4.2.7. XANES Fe *K*-edge spectra of the series of as-prepared ACFP. For comparison, the spectra of Fe₂O₃ is shown for reference samples of Fe³⁺.

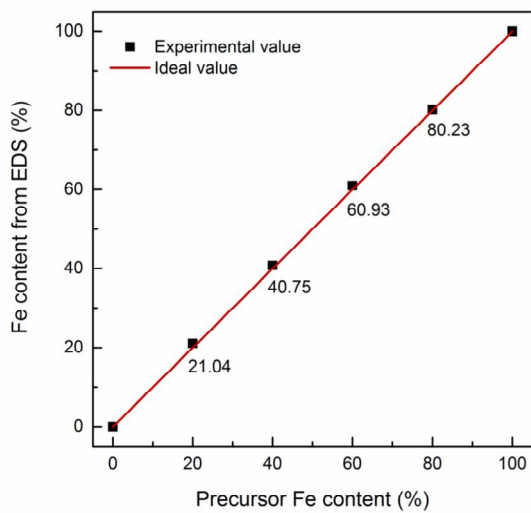


Figure 4.2.8. Quantitative analysis of Co/Fe ratio from EDS.

Table 4.2.1. Ratios of elements in the series of ACFP.

	Co	Fe	Si	O
ACFP10	16.589		18.605	64.8055
ACFP82	12.31	3.28	17.945	66.47
ACFP64	9.79	6.735	18.785	64.69
ACFP46	5.815	9.07	17.755	67.355
ACFP28	2.61	10.595	16.205	70.59
ACFP01		16.47	18.12	65.41

3.3.2 XPS analysis for solid solution forming

In amorphous materials, it is difficult to find out whether material is in the form of solid solution or phase separated from crystal structural changes with XRD. Therefore, we confirmed the forming of solid solution from electronic structural change with XPS. **Figure 4.2.9** exhibits the Co 2p spectra of ACFPs. Co 2p peak is composed of two peak, Co 2p main peak and its satellite peak with higher binding energy than main peak. The main peak and satellite peak are related to the $2p^53d^8L^{-1}$ and $2p^53d^7$ final state, respectively. When photoelectron is generated in the 2p orbital by absorbing the X-ray, the hole in the 2p core orbital shows strong attraction. For screening this attraction, the electron in the L shell of ligand transfers to the cobalt 3d orbital. Therefore, photoelectron can be emitted with maintaining the initial kinetic energy. The competitive process is less screening process by *sp* orbital than ligand charge transfer, which is denoted $2p^53d^7$. As a result, photoelectron has lower kinetic energy and higher binding energy than main peak. As the Fe contents increases, the intensity of satellite peak increases as compared to that of main peak. It can be seen that ligand charge transfer to Co ion during photoelectron emission process becomes more difficult because the electron of oxygen existing between Co^{2+} and Fe^{3+} is biased toward the Fe^{3+} with the larger electronegativity. These results are evidence that Co and Fe exist in the form of solid solutions affecting each other.

The Fe 2p spectra of ACFPs are also varied with the ratio of Co and Fe ion as shown in **Figure 4.2.10**. In case of Fe³⁺ in octahedral structure, since electron configuration of 3d orbital exhibits high spin state, five unpaired electrons are in 3d orbital. When core unpaired electron in 2p orbital is created by X-ray absorption, coupling between this electron and unpaired electron in 3d orbital can create a number of final state. Therefore, Fe 2p peak shows multiplet peak structure. The intensity and position of these multiplet peak are changed by the ligand charge transfer effect in transition metal compound. The change of the Fe 2p spectrum with variation of the ratio of Co and Fe can be another evidence about solid solution.

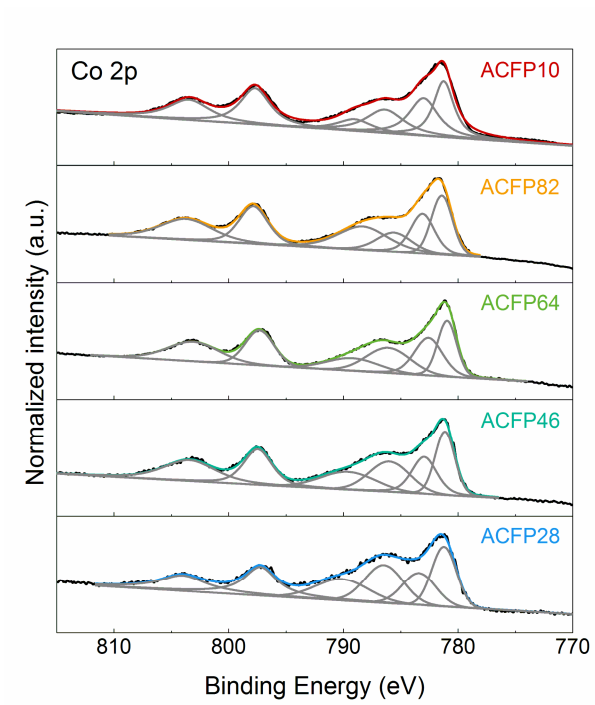


Figure 4.2.9. XPS Co 2p spectra of the series of ACFP.

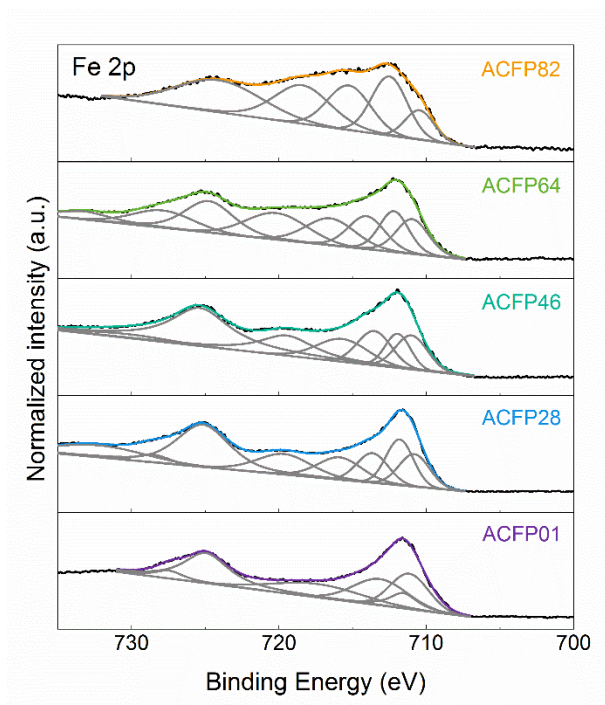


Figure 4.2.10. XPS Fe 2p spectra of the series of ACFP.

3.3.3 Electrochemical properties of ACFP

The electrochemical properties of ACFPs were measured in the three electrode beaker cell configurations in 1 M KOH electrolyte. The OER performance was evaluated by cyclic voltammetry (CV) and the corresponding Tafel plot. As we mentioned at experimental section, the overpotential (η) at current density of 10 mA cm^{-2} was used to evaluate OER catalytic activity. From the iR corrected polarization curves, catalytic activity can be enhanced until addition of Fe ion reaches 40% (ACFP64) as shown in **Figure 4.2.11**. Relative values of the specific surface area were evaluated by the electrochemical active surface area (ECSA) to eliminate the specific surface area factor affecting the OER performance (see **Figure 4.2.12**). Electrochemical double layer capacitances (C_{dl}) of ACFPs were obtained by the slope of the scan rate versus the capacitive current density. The value of C_{dl} tended to decrease gradually with increasing Fe content. It can be seen that the improvement is not caused by the specific surface area because the OER activity are improved despite the decrease of the specific surface area. Notably, although there was no significant difference in the onset potential except for ACFP01, the slopes of curves caused the difference of overpotential. However, when Fe was added more than that, overpotential tended to increase again. Corresponding Tafel slopes of ACFPs are shown in **Figure 4.2.13**. In the case of cobalt pure phyllosilicate (ACFP10), the Tafel slope was approximately 60 mV dec^{-1} whereas that of Fe-containing phyllosilicate (ACFP82 ~ ACFP01) decreased

to approximately 40 mV dec^{-1} . Although finding the rate determining step through the experimentally obtained Tafel slope is difficult because the other factors such as series resistance, mass transportation and surface coverage have a large effect on it. However, it can be inferred that the rate determining step of the oxygen evolution reaction may have changed due to the large change in the Tafel slope due to Fe addition. The changes in overpotential and Tafel slope according to Fe content are shown in **Figure 4.2.14**. Both values plotted a U-shaped plot and showed the smallest overpotential value in ACFP64. The overpotential for OER of ACFP10 was 365 mV, which was consistent with the previously reported value, and the overpotential was 325 mV in ACFP64. These trends as a function of Fe content are very similar with the previously reported trends of NiFe or CoFe LDH. Burke *et al.* reported that the Tafel slope of 60 mV dec^{-1} in electrodeposited pure cobalt film was reduced to 30 mV dec^{-1} at 55% Fe containing film.[31] In addition, Görlin *et al.* reported that the tafel slope, which showed 55 mV dec^{-1} at $\text{Ni}_{100}\text{Fe}_0$, could be reduced to 35 mV dec^{-1} at $\text{Ni}_{45}\text{Fe}_{55}$ in the NiFe catalyst.[29] From the comparison of overpotential with hydroxide catalyst (see **Figure 4.2.15**), the effect of silicate layer reported in previous part is still valid in Co-Fe binary system at all Co-Fe ratio .

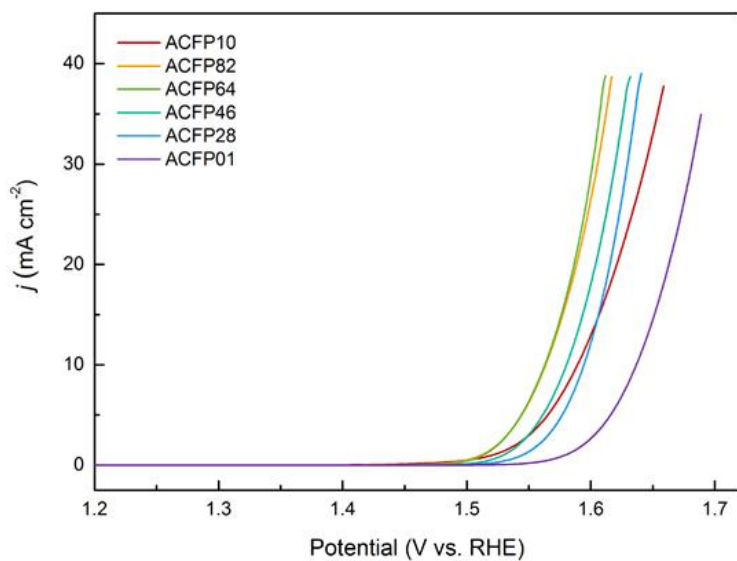


Figure 4.2.11. *iR*-corrected polarization curves in 1 m KOH at a scan rate of 10 mV s^{-1} .

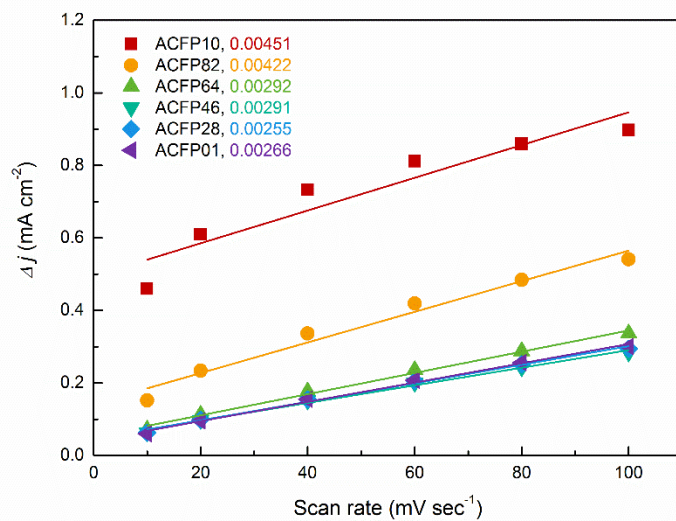


Figure 4.2.12. Double layer capacitance of the series of ACFPs for comparison of electrochemical active surface area.

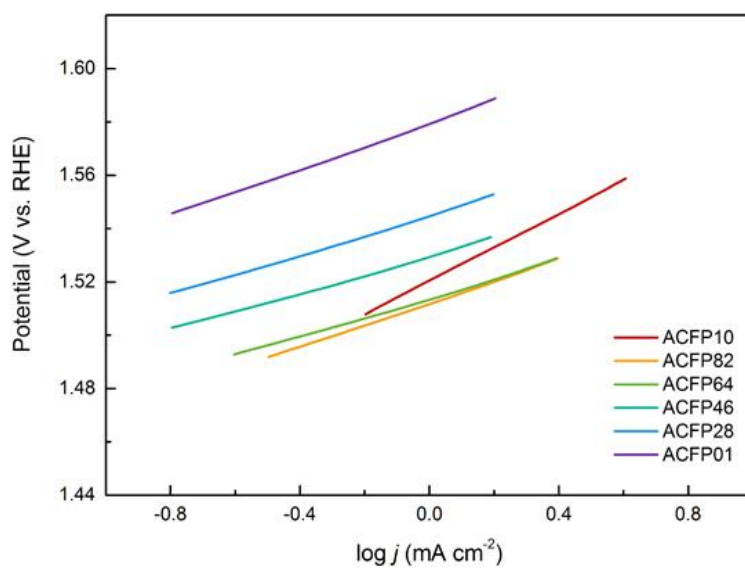


Figure 4.2.13. Tafel plots of the series of ACFP corresponding to Figure 4.2.11.

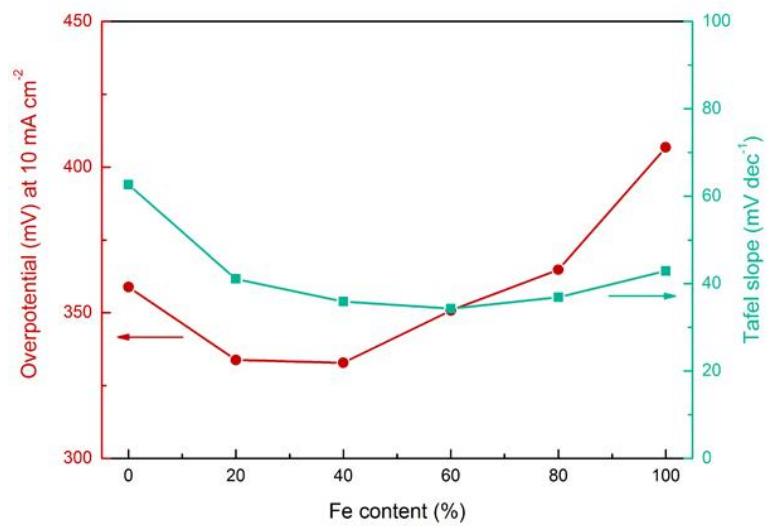


Figure 4.2.14. Overpotential and Tafel slope variation as a function of Fe content.

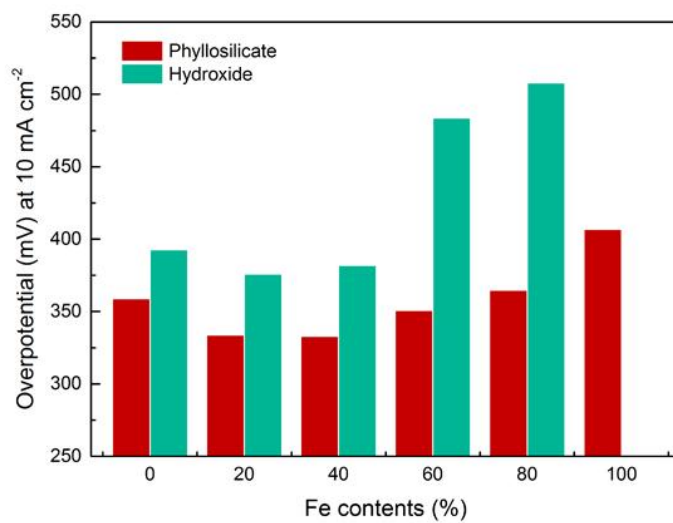


Figure 4.2.15. Overpotential comparison of phyllosilicate and hydroxide catalysts.

3.3.4 The oxidation state analysis: EPR analysis

It is important to understand the reaction mechanism accurately because the improvement of OER by Fe addition accompanies the change of Tafel slope which means the change of RDS. Therefore, the oxidation state of Co and Fe during OER is investigated by EPR spectroscopy as shown in **Figure 4.2.16**. In case of Co ion, since Co^{2+} and Co^{4+} have an unpaired electron in $3d$ orbital, it can be detected by EPR analysis. The EPR spectrum of as-prepared ACFP10 shows only Co^{2+} signal. However, after bulk electrolysis at $1.6 V_{\text{RHE}}$ for 10 min, the EPR spectrum of freezed ACFP10 sample clearly exhibits Co^{4+} signal. Generally, the RDS of Co-based catalysts is the step in which intermediates are passed from O^* to OOH^* , and when the intermediate is O^* , the Co ion is present at $4+$. Therefore Co^{4+} is detected in the EPR because it remains the longest in Co^{4+} during OER. In contrast, the EPR spectrum of as-prepared ACFP64 has Co^{2+} and Fe^{3+} signal and even if potential is applied. This result means that the step in which intermediates are passed from O^* to OOH^* becomes fast to be detected in the EPR analysis. In the step from O^* to OOH^* , the OH adsorption energy significantly affect to reaction rate. The OH adsorption energy of Co catalyst can be tuned to an appropriate value for OH adsorption energy when Fe ion which has strong OH adsorption energy is incorporated.[111] Therefore, the reaction rate of step from O^* to OOH^* becomes faster than before and this may induce the change of RDS.

These assumptions are also consistent with the change in Tafel slope with Fe ion incorporation.

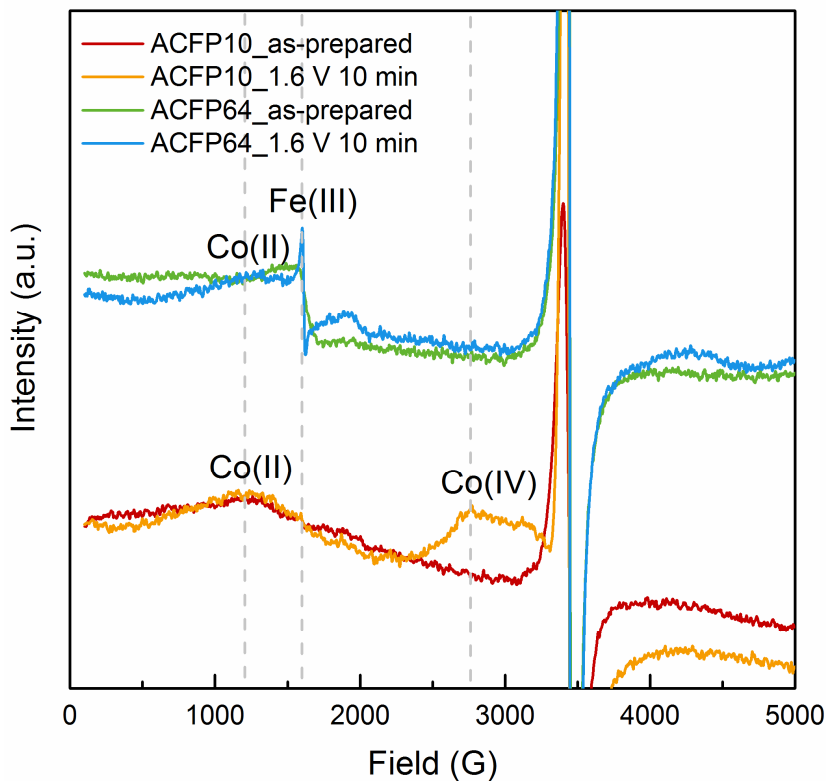


Figure 4.2.16. EPR spectra of ACFP10 and ACFP64. For comparison, the as-prepared sample and the sample when the OER potential was applied were plotted together.

3.3.5 Determination of reaction sites in ACFP

To understand the effects of Fe substitution into ACP on the catalytic reaction at an atomistic level, we investigated the OER thermodynamics using DFT calculations. Five-layer ACP slab model proposed in our previous study was also used in this work to calculate OER energetics. Due to the asymmetry of ACP slab, there exist two types of surface layer depending on the orientation of silicate groups on the surface which were designated as model 1 and model 2 respectively as shown in **Figure 4.2.17**. For the purpose of comparing the catalytic activities of ACP and ACFP, one of the Co ions in the topmost surface layer of the ACP slab was substituted for Fe ions. All the possible transition metal sites were considered for Fe substitution, and the most thermodynamically stable case were adopted in each model for the calculation of OER energetics. The presence of silicate groups and Fe ions induced diverse atomic sites with distinct local environment on the surface. Atomic sites can be broadly divided into bridge sites which mean μ_2 -O bridges between metal ions and terminal sites which mean terminal oxygen atoms on top of metal octahedral. In our previous study, we reported that silicate groups provides the surface of ACP with the structural flexibility due to the lack of interlayer O-H-O bonds, resulting in bridge 1 site with a very low theoretical η (340 mV).[15] The first-principles calculations revealed that the catalytic activities of each atomic site were further regulated by the introduction of Fe as shown in **Figure 4.2.18**. Compared to the pure ACP, of particular significance in the case of

Fe-doped ACP is the activation of bridge 2 and bridge 3 sites. While the bridge 2 and bridge 3 sites exhibit a η of 690 mV and 810 mV in the pure ACP respectively, their η are remarkably lowered to 320 mV and 250 mV respectively in the Fe-doped ACP. On the other hand, the catalytic activity of bridge 1 site which was the most active site in the pure ACP with η of 340 mV is almost unchanged by the incorporation of Fe, representing η of 420 mV. Considering the low η of bridge 2 and bridge 3 sites along with the preserved catalytic activity of bridge 1 site, the results of DFT calculation imply that the substitution of Fe into ACP can enhance the overall catalytic activity significantly by increasing the number of catalytically active sites, although the other atomic sites of Fe-doped ACP represents comparable or higher η compared with those of the pure ACP.

For more precious analysis for OER thermodynamics, four OER steps of bridge 3 site is shown in **Figure 4.2.19**. Standard condition ($T = 298.15\text{K}$, $P = 1$ bar, and $\text{pH} = 0$) and the thermodynamic equilibrium potential for OER ($1.23 \text{ V}_{\text{RHE}}$) is assumed for these calculation. The overall OER overpotential of each sites is determined by RDS which exhibits the largest overpotential among the steps. In case of bridge 3 site for pure ACP, the third steps (OOH^* formation step) is the RDS, showing extremely large theoretical overpotential value (0.81 eV). In contrast, RDS of bridge 3 site for Fe doped ACP is changed to the second step (O^* formation step) with lowering overpotential value (0.25 eV). From these results, incorporation of Fe ion induces facilitating OOH^* formation step compared to the

catalyst containing only Co ion. This calculation results are consistent with the results of experimentally observed RDS changes in Tafel plot and EPR spectrum.

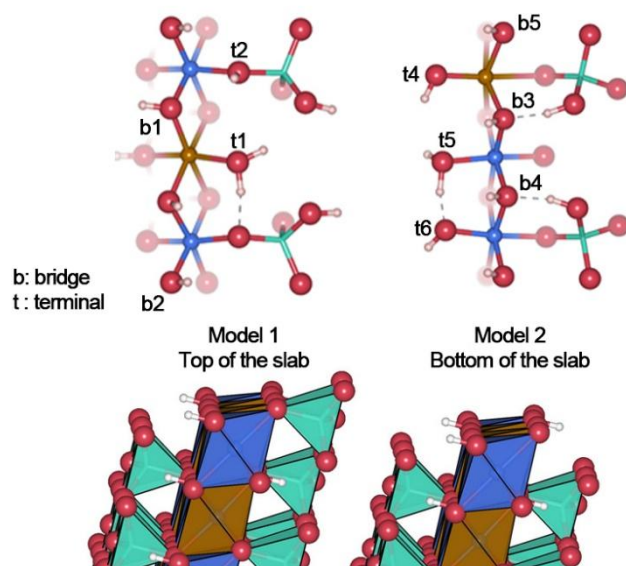


Figure 4.2.17. Top view of active surface of ACFP, showing active sites for the OER. Co, Fe, Si, O, and H are represented by blue, dark yellow, green, red, and white spheres, respectively.

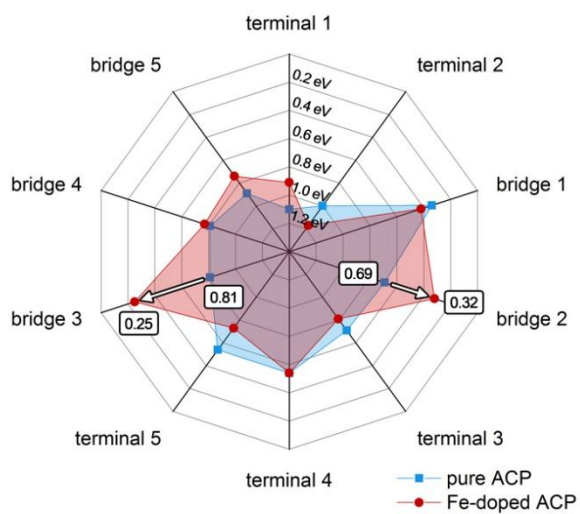


Figure 4.2.18. Radar plot for comparison with pure ACP and Fe-doped ACP of overpotential at each sites.

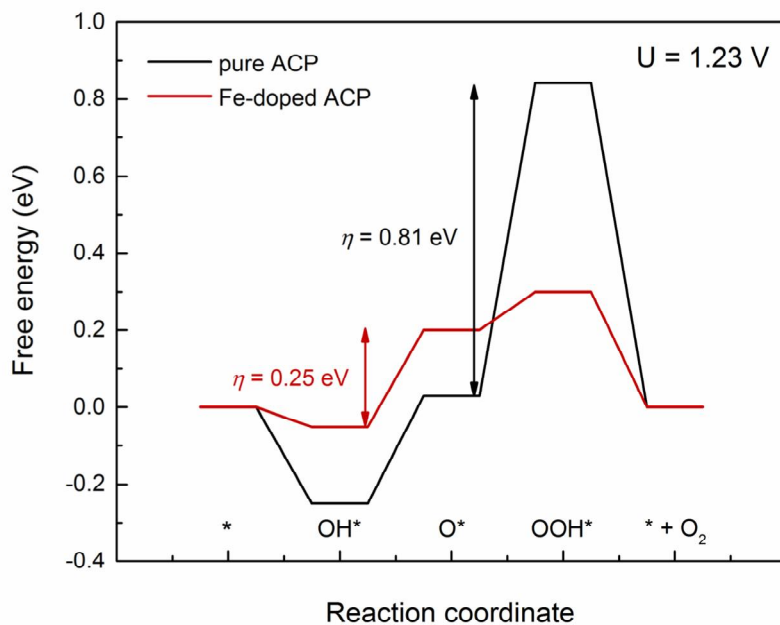


Figure 4.2.19. Free energy landscape of pure ACP and Fe-doped ACP for OER at 1.23 V (ideal potential for OER).

4.2.6 Tracking bridge site oxygen evolution

In contrast to the terminal site known to have a fast exchange rate, the oxygen on the bridge site constituted the lattice, so there was much debate as to whether it could actually participate in the OER.[24, 130] Since the calculation results show that the bridge site has the best activity in the ACFP catalyst, ^{18}O isotope labeling to bridge site experiment was performed to prove participation of bridge site oxygen. If the oxygen at the bridge site can participate in the OER, as the reaction proceeds, the oxygen at the bridge site evolves as an oxygen gas and this vacancy is filled with the oxygen of the electrolyte. Therefore, OER sufficiently proceeded in the KOH electrolyte based on H_2^{18}O water to replace the oxygen in the bridge site with ^{18}O . Then, electrode was rinsed by deionized water based on H_2^{16}O . Oxygen at the terminal site can also be substituted to ^{18}O when OER occurs in the KOH electrolyte based on H_2^{18}O . Since it is known that the exchange of oxygen at the terminal site with the oxygen in the electrolyte occurs rapidly,[24] the resting state was maintained for 5 hours on the KOH electrolyte based on H_2^{16}O water in order to remove ^{18}O from the terminal site. Then, $^{34}\text{O}_2$ gas analysis was performed by DEMS in the KOH electrolyte based on H_2^{16}O water. As shown in **Figure 4.2.20**, $^{34}\text{O}_2$ partial pressure increases with applying voltage for ^{18}O labeled ACFP64. From the comparison with unlabeled ACFP64, this signal is not due to an isotope present in nature. This analysis can support the results of the OER participation of the bridge site oxygen calculated computationally.

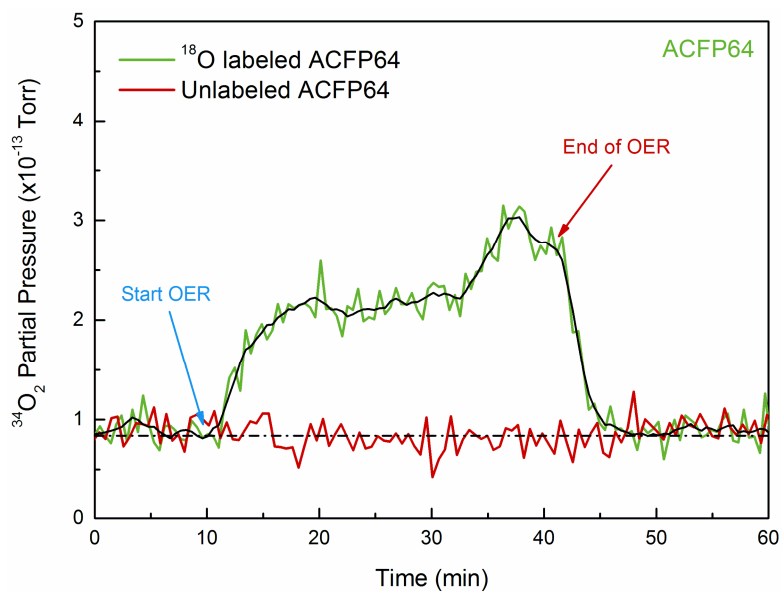


Figure 4.2.20. DEMS analysis during OER to detect $^{34}\text{O}_2$ gas evolution.

4.3 Conclusion

In summary, our study demonstrated the possibility of amorphous cobalt iron phyllosilicate as a new efficient OER electrocatalyst because ACFP is not only earth abundant but also can be synthesized easily at room temperature. The introduction of Fe into Co phyllosilicate has resulted in a remarkable improvement in OER performance from overpotential of 365 mV to 325 mV at current density of 10 mA cm⁻² with lowering Tafel slope from ~60 mV dec⁻¹ to ~40 mV dec⁻¹ in spite of decrease of electrochemical active surface area. Oxidation state analysis during OER was performed by EPR spectroscopy and indicates that incorporation of Fe ion can induce the change of RDS compared to Co phyllosilicate. First-principles calculations revealed that this improvement in OER performance was attributed to activation of two additional bridge sites and overpotential of bridge sites decreased with changing RDS step when Fe was introduced. Gas analysis by DEMS was also conducted to prove participation of bridge site oxygen. This work may shed light on the origin of OER performance enhancement by introducing new elements, which would be valuable for the designing of efficient OER catalysts for industrial application.

Chapter 5. Concluding remarks

The development of efficient and low-cost OER catalyst is quite important for the industrial feasibility of hydrogen energy. In this thesis, we reported a cost-effective catalyst by applying phyllosilicate, a kind of earth-abundant mineral present in the nature, as an OER catalyst, and discussed how each part in the structure can affect the OER catalytic activity by the DFT calculation. The silicate layer of phyllosilicate gave structure flexibility compared to the layered hydroxide by breaking bonding between layers, which resulted in overpotential reduction of the active site. In addition, the Fe ion introduced into the amorphous cobalt phyllosilicate could activate the reaction sites by lowering the overpotential of the reaction sites around the cobalt. The OER performance of phyllosilicate catalysts reported in this thesis are shown in **Table 5.1** for comparison with the previously reported catalysts. In the case of amorphous cobalt phyllosilicate, the OER characteristics were remarkably superior to those of the previously reported Co catalysts. In the case of amorphous cobalt iron phyllosilicate, it is found that the catalyst has very excellent properties among multi-metal based catalysts. Although structural modified catalysts exhibits lower overpotential than phyllosilicate catalysts, phyllosilicate catalysts are also expected that OER activity can be improved by hybrid structure with carbon material and optimization of catalyst condition. In addition, the fact that the process is simpler than other catalysts and that the cost of materials is inexpensive has the potential to be the most likely

candidate to replace existing precious metal-based catalysts. We believe knowledge of OER catalyst field can be broaden by applying phyllosilicate as an OER catalyst, and expect that these discussions will play a role as a diection guidance of designing new efficient OER catalysts.

Table 5.1. Electrocatalytic OER activities of previously reported metal oxide catalysts

Catalyst	Electrolyte	Substrate	Catalyst loading amount	Overpotential at specific current density	Ref
Amorphous cobalt phyllosilicate	1 M KOH	Carbon paper	0.4 mg cm ⁻²	367 mV @ 10 mA cm ⁻²	This work
Amorphous cobalt iron phyllosilicate	1 M KOH	Carbon paper	0.4 mg cm ⁻²	330 mV @ 10 mA cm ⁻²	This work
γ -CoOOH bulk	1 M KOH	Glassy carbon	0.15 mg cm ⁻²	374 mV @ 10 mA cm ⁻²	[131]
γ -CoOOH nanosheet	1 M KOH	Glassy carbon	0.15 mg cm ⁻²	300 mV @ 10 mA cm ⁻²	[131]
Co oxide / Au	0.1 M KOH	Au	-	~450 mV @ 10 mA cm ⁻²	[132]
Electrodeposited crystalline Co ₃ O ₄	1 M KOH	Stainless steel	-	~400 mV @ 10 mA cm ⁻²	[133]
Au@Co ₃ O ₄	0.1 M KOH	Glassy carbon	200 μ g cm ⁻²	350 mV @ 2.84 mA cm ⁻²	[134]
Co ₃ O ₄ /GR	0.1 M KOH	ITO glass	-	540 mV @ 1.30 mA cm ⁻²	[135]
Co ₃ O ₄	1 M KOH	Ti	-	440 mV @ 10 mA cm ⁻²	[136]
Alkoxide-intercalated Co-Fe LDH	1 M KOH	Ni foam	1 mg cm ⁻²	310 mV (onset)	[137]
Ni-Co LDH nanosheets	0.1 M KOH	Ni foam	1.76 mg cm ⁻²	670 mV @ 50 mA cm ⁻²	[138]
Co _{0.54} Fe _{0.46} OOH	0.1 M	Glassy	0.20	390 mV	[139]

nanosized Ni-Fe LDH/N-doped graphene	KOH	carbon	mg cm^{-2}	@ 10 mA cm^{-2}	[140]
	0.1 M KOH	Glassy carbon	0.25 mg cm^{-2}	337 mV @ 10 mA cm^{-2}	
Co-Fe LDH/rGO	0.1 M KOH	Glassy carbon	0.2 mg cm^{-2}	340 mV @ 10 mA cm^{-2}	[141]
	1 M KOH	Glassy carbon	0.142 mg cm^{-2}	324 mV @ 10 mA cm^{-2}	
Co-Fe LDH (1:0.35)	0.1 M KOH	Glassy carbon	250 $\mu\text{g cm}^{-2}$	350 mV @ 10 mA cm^{-2}	[95]
Co-Fe O _x film (64:36)	0.1 M KOH	FTO	-	270 @ 1 mA cm^{-2}	[112]
Fe-Co-W oxyhydroxide (1:1.02:0.70)	0.1 M KOH	gold-plated Ni foam	0.21 mg cm^{-2}	191 @ 10 mA cm^{-2}	[111]
Co _{0.5} Mn _{0.5} WO ₄	0.1 M KOH	Glassy carbon	0.2 mg cm^{-2}	400 @ 10 mA cm^{-2}	[142]
Zn-Co LDH	0.1 M KOH (pH 13)	Glassy carbon	0.28 mg cm^{-2}	340 mV (onset)	[100]
Ni-Co-OH	1 M NaOH	Glassy carbon	0.82 mg cm^{-2}	337 mV @ 10 mA cm^{-2} (2-h constant current polarization)	[143]
Exfoliated Ni-Fe nanosheets	1 M KOH	GCE	0.07 mg cm^{-2}	300 mV @ 10 mA cm^{-2}	[64]

Chapter 6. Abstract in Korean

수소는 지속 가능성과 기존의 화석 연료에 비해 높은 에너지 밀도를 갖고 있다는 장점 덕분에 다음 세대의 유망한 에너지 자원 중 하나로 각광을 받고 있다. 수소는 다양한 방법으로 생산될 수 있지만, 그 중에서 물을 분해하여 수소를 생산하는 방법은 환경 친화적이고 지속성이 우수하기 때문에 최선의 해결책으로 여겨지고 있다. 산업적인 수요를 만족하기 위해선 효율적인 물 분해 시스템의 구축이 중요하다. 물 분해 시스템의 구성 요소 중, 산소 발생 촉매의 개발은 매우 중요하다. 그 이유는 산소 발생 반응은 4 전자 반응이고 O-O 결합 형성이 느리기 때문에 이에 의해서 물 분해 전반의 속도가 결정되기 때문이다. 따라서 많은 연구들이 새로운 고효율의 산소 발생 촉매의 개발과 메커니즘 이해를 위해 진행되고 있다.

산소 발생 촉매의 연구 초기에는, Ru나 Ir 같은 귀금속 혹은 이의 산화물 형태의 촉매들이 그 우수한 특성 때문에 폭 넓게 연구가 진행되어 왔지만, 희소성에 따른 비싼 가격은 상용화에 가장 큰 걸림돌로 작용하게 됐다. 이를 해결하기 위한 방안으로, 3d 전이금속 (Mn, Fe, Co 그리고 Ni)을 기반으로 하는 촉매들이 제시되었다. 보고된 많은 전이금속 촉매는 중성과 알칼라인 전해질에서 매우 우수한 특성과 안정성을 보였다. 또한, 많은 연구들이 반응의 메커니즘과 특성을 결정짓는 요소를 알기 위해 진행됐지만, 많은 부분이 여전히 밝혀지지 않았으며 추가적인 연구가 필요한 실정이다.

이 학위 논문에서는 자연계에 존재하는 층상 규산염이라는 광물을 이용하여 우수한 특성을 보이는 산소 발생 촉매로 적용하였으며, 구조 내의 여러 요소들이 어떻게 산소 발생 반응에 영향을 미칠 수 있는 지에 대해 분석하였다. 우리는 층상 규산염 기반의 촉매 연구를 통해 고효율은 촉매를 디자인하는데 새로운 길을 제시할 수 있을 것이라고 생각한다.

2장에서는 층상의 결정 구조 모티프를 갖는 비정질의 코발트

기반 층상규산염을 새로운 산소 발생 촉매로 적용하였다. XAS를 이용한 구조 분석을 통해 비정질 층상규산염 촉매가 제일원리 계산을 통해 밝혀진 산소 발생 반응에 유리한 CoOOH와 유사한 구조를 갖고 있음을 알 수 있었다. 또한 활성 부위 주변의 실리케이트로 인해 산소 발생 반응에 필요한 과전압을 CoOOH에 비해서 낮출 수 있음을 제일 원리 계산을 통해 증명하였다.

3장에서는 비정질 층상 규산염 내에서 코발트와 철 이온의 역할에 대해 논의하였다. 실험적 분석을 통해서 합성된 비정질 코발트 철 층상 규산염 촉매가 고용체를 이루고 있음을 확인하였다. 철이 첨가됨에 따라 철의 함량 40%의 범위까지 산소 발생 반응에 필요한 과전압이 감소하였고, Tafel slope 또한 코발트만 존재하는 상에 비해 줄어들었다. 제일 원리 계산을 통해 철 이온의 함유에 의해 높은 과전압을 필요로 하던 반응 부위가 과전압이 낮아지며 산소 발생 반응의 활성을 떨 수 있음을 증명하였다.

주요어: 층상 규산염, 물 전기분해, 산소 발생 반응, 층상 수산화물, 전이금속, 전기촉매

학 번: 2009-23894

Chapter 7. Curriculum Vitae

Educational Background

- **Unified Course of the Master and Ph. D. Candidate**

September 2009 – February 2014

Electronic Functional Materials Laboratory

Department of Materials Science and Engineering

Seoul National University | Republic of Korea

(Supervisor: Prof. Kug Sun Hong)

March 2014 – Present

Advanced Energy Materials Laboratory

Department of Materials Science and Engineering

Seoul National University | Republic of Korea

(Supervisor: Prof. Kisuk Kang)

- **Bachelor of Science**

March 2005 – August 2009

Major: Advanced Materials Science and Engineering

Sungkyunkwan University | Republic of Korea

Research Interests

Synthesis of nanostructured materials for energy system

Control of electron and electrolyte transport properties by nanostructured metal oxide materials.

- Fast electron transport electrode using 1-D based nanostructure materials for solar fuel system
- Electron and electrolyte kinetic control in energy storage system

Electrocatalyst materials for water splitting

Metal hydroxide as oxygen evolution reaction catalyst

- Novel catalyst materials for oxygen evolution reaction
- Effect of redox inactive part in structure
- Multication system for improving catalytic properties

Honors and Scholarships

- Encouragement Prize in the Patent-Universiade (Seoul, December, 2011)
- Excellence Prize in the Patent-Universiade (Seoul, December, 2012)
- PACRIM award in the Korean Ceramic Society (Seoul, November, 2016)

List of Publications

† These authors contributed equally.

- 1) **Ju Seong Kim**, Byunghoon Kim, Inchul Park and Kisuk Kang “Activation of reaction sites in amorphous cobalt iron phyllosilicate for the oxygen evolution reaction”, In preparation
- 2) **Ju Seong Kim**†, Byunghoon Kim†, Byunghoon Kim† and Kisuk Kang "Recent Progress on Multi-metal Oxide Catalysts for the Oxygen Evolution Reaction", Advanced Energy Materials, Accepted
- 3) **Ju Seong Kim**†, Inchul Park†, Eun-Suk Jeong, Kyoungsuk Jin, Won Mo Seong, Gabin Yoon, Hyunah Kim, Byunghoon Kim, Ki Tae Nam and Kisuk Kang "Amorphous cobalt phyllosilicate with layered crystalline motifs as water oxidation catalyst", Advanced Materials, Vol. 29, pp. 1606893 (2017)
- 4) Jun Kim†, **Ju Seong Kim**†, Hionsuck Baik, Kisuk Kang and Kwangyeol Lee "Porous β -MnO₂ nanoplates derived from MnCO₃ nanoplates as highly efficient electrocatalysts toward oxygen evolution reaction", RSC Advances, Vol. 6, pp. 26535 (2016)
- 5) **Ju Seong Kim**†, Seong Sik Shin, Hyun Soo Han, Sun Shin, Jae Ho Suk, Kisuk Kang, Kug Sun Hong and In Sun Cho “Facile preparation of TiO₂ nanobranch/nanoparticle hybrid architecture with enhanced light harvesting properties for dye-sensitized solar cells”, Journal of Nanomaterials, Vol 1, pp.

9 (2015)

- 6) **Ju Seong Kim†**, Seong Sik Shin, Hyun Soo Han, Lee Seul Oh, Dong Hoe Kim, Jae-Hun Kim, Kug Sun Hong and Jin Young Kim “1-D structured flexible supercapacitor electrodes with prominent electronic/ionic transport capabilities”, ACS Applied Materials & Interfaces, Vol 6, pp. 268 (2014)
- 7) **Ju Seong Kim†**, Hyun Soo Han, Sun Shin, Gill Sang Han, Hyun Suk Jung, Kug Sun Hong and Jun Hong Noh “In₂O₃:Sn/TiO₂/CdS heterojunction nanowire array photoanode in photoelectrochemical cells”, International Journal of Hydrogen Energy, Vol 39, pp. 17473 (2014)
- 8) **Ju Seong Kim†**, Hee Jo Song, Hee-Suk Roh, Dong Kyun Yim, Jun Hong Noh and Kug Sun Hong “Luminescent characteristics of green emitting Li₂Ca₂Si₂O₇:Eu²⁺ phosphor”, Materials Letters, Vol 79, pp. 112 (2012)
- 9) Hyun Soo Han, Gill Sang Han, **Ju Seong Kim**, Dong Hoe Kim, Jung Sug Hong, Salim Caliskan, Hyun Suk Jung, In Sun Cho and Jung-Kun Lee “Indium-Tin-Oxide nanowire array based CdSe/CdS/TiO₂ one-dimensional heterojunction photoelectrode for enhanced solar hydrogen production”, ACS Sustainable Chemistry & Engineering, Vol 4, pp. 1161 (2016)
- 10) Sun Shin, Hyun Soo Han, **Ju Seong Kim**, Ik Jae Park, Myeong Hwan Lee, Kug Sun Hong and In Sun Cho “A tree-like nanoporous WO₃ photoanode with enhanced charge transport efficiency for photoelectrochemical water oxidation” Journal of Materials Chemistry A, Vol 3, pp. 12920 (2015)
- 11) Seong Sik Shin, Woon Seok Yang, Jun Hong Noh, Jae Ho Suk, Nam Joong

- Jeon, Jong Hoon Park, **Ju Seong Kim**, Won Mo Seong and Sang Il Seok
“High-performance flexible perovskite solar cells exploiting Zn_2SnO_4 prepared
in solution below 100 °C” Nature Communications, Vol 6, pp. 7410 (2015)
- 12) Seong Sik Shin, Dong Wook Kim, Jong Hoon Park, Dong Hoe Kim, **Ju Seong Kim**, Kug Sun Hong and In Sun Cho “Anionic ligand assisted synthesis of 3-D hollow TiO_2 architecture with enhanced photoelectrochemical performance” Langmuir, Vol 30, pp. 15531 (2014)
- 13) Seong Sik Shin, **Ju Seong Kim**, Jae Ho Suk, Kee Doo Lee, Dong Wook Kim, Jong Hoon Park, In Sun Cho, Kug Sun Hong and Jin Young Kim “Improved quantum efficiency of highly efficient perovskite $BaSnO_3$ -based dye-sensitized solar cells” ACS Nano, Vol 7, pp. 1027 (2013)
- 14) Hyun Soo Han, **Ju Seong Kim**, Dong Hoe Kim, Gil Sang Han, Hyun Suk Jung, Jun Hong Noh and Kug Sun Hong “ TiO_2 nanocrystals shell layer on highly conducting indium tin oxide nanowire for photovoltaic devices”, Nanoscale, Vol 5, pp. 3520 (2013)
- 15) Dong Hoe Kim, Won Mo Seong, Ik Jae Park, Eun-Sang Yu, Seong Sik Shin, **Ju Seong Kim**, Hyun Suk Jung, Sangwook Lee and Kug Sun Hong “Anatase TiO_2 nanorod-decorating for highly efficient photoenergy conversion”, Nanoscale, Vol 5, pp. 11725 (2013)
- 16) Seong Sik Shin, Dong Wook Kim, Daesub Hwang, Jae Ho Suk, Lee Seul Oh, Byung Suh Han, Dong Hoe Kim, **Ju Seong Kim**, Dongho Kim, Jin Young Kim and Kug Sun Hong “Controlled interfacial electron dynamics in highly

- efficient Zn₂SnO₄-based dye-sensitized solar cells” CHEMSUSCHEM, Vol 7, pp. 501 (2013)
- 17) Ik Jae Park, Hee-Suk Roh, Hee Jo Song, Dong Hoe Kim, **Ju Seong Kim**, Won Mo Seong, Dong-Wan Kim and Kug Sun Hong “ γ -Al₂O₃ nanospheres-directed synthesis of monodispersed BaAl₂O₄:Eu²⁺ nanosphere phosphors” CrystEngComm, Vol. 15, pp. 4797 (2013)
- 18) Hee Jo Song, Jun Hong Noh, Hee-Suk Roh, **Ju Seong Kim**, Dong-Wan Kim and Kug Sun Hong “Preparation and characterization of nano-sized Y₃Al₅O₁₂:Ce³⁺ phosphor by high-energy milling process” Current Applied Physics, Vol. 13, pp. S69 (2013)
- 19) Jun Hong Noh, Bo Ding, Hyun Soo Han, **Ju Seong Kim**, Jong Hoon Park, Sang Baek Park, Hyun Suk Jung, Jung-Kun Lee and Kug Sun Hong “Tin doped indium oxide core-TiO₂ shell nanowires on stainless steel mesh for flexible photoelectrochemical cells” Applied Physics Letters, Vol 100. pp. 084104 (2012)
- 20) Sang Hyeon Kim, Sangbaek Park, Chan Woo Lee, Byung Suh Han, Se Won Seo, **Ju Seong Kim**, In Sun Cho and Kug Sun Hong “Photophysical and photocatalytic water splitting performance of stibiotantalite type-structure compounds, SbMO₄ (M = Nb, Ta)” International Journal of Hydrogen Energy, Vol 37, pp. 16895 (2012)
- 21) Dong Kyun Yim, Hee Jo Song, In-Sun Cho, **Ju Seong Kim** and Kug Sun Hong “A novel blue-emitting NaSrPO₄:Eu²⁺ phosphor for near UV based white

light-emitting-diodes” Materials Letters, Vol. 65, pp. 1666 (2011)

Chapter 8. References

- [1] S. Chu, Y. Cui, N. Liu, *Nat. Mater.* **2017**, *16*, 16.
- [2] M. Jacobson, W. Colella, D. Golden, *Science* **2005**, *308*, 1901.
- [3] U. S. E. I. Administration, 2017.
- [4] F. M. Sapountzi, J. M. Gracia, H. O. Fredriksson, J. H. Niemantsverdriet, *Progr. Energy Combust. Sci.* **2017**, *58*, 1.
- [5] U. S. d. o. Energy, in *Fuel cell technologies office*, Vol. 2017, 2017.
- [6] W. T. Hong, M. Risch, K. A. Stoerzinger, A. Grimaud, J. Suntivich, Y. Shao-Horn, *Energy Environ. Sci.* **2015**, *8*, 1404.
- [7] N.-T. Suen, S.-F. Hung, Q. Quan, N. Zhang, Y.-J. Xu, H. M. Chen, *Chem. Soc. Rev.* **2017**, *46*, 337.
- [8] I. C. Man, H. Y. Su, F. Calle-Vallejo, H. A. Hansen, J. I. Martínez, N. G. Inoglu, J. Kitchin, T. F. Jaramillo, J. K. Nørskov, J. Rossmeisl, *ChemCatChem* **2011**, *3*, 1159.
- [9] S. Cherevko, S. Geiger, O. Kasian, N. Kulyk, J.-P. Grote, A. Savan, B. R. Shrestha, S. Merzlikin, B. Breitbach, A. Ludwig, *Catal. Today* **2016**, *262*, 170.
- [10] R. Kötz, H. Neff, S. Stucki, *J. Electrochem. Soc.* **1984**, *131*, 72.
- [11] R. Kötz, H. Lewerenz, S. Stucki, *J. Electrochem. Soc.* **1983**, *130*, 825.

- [12] InfoMine, 2017.
- [13] M. W. Kanan, D. G. Nocera, *Science* **2008**, *321*, 1072.
- [14] J. Park, H. Kim, K. Jin, B. J. Lee, Y.-S. Park, H. Kim, I. Park, K. D. Yang, H.-Y. Jeong, J. Kim, *J. Am. Chem. Soc.* **2014**, *136*, 4201.
- [15] J. S. Kim, I. Park, E. S. Jeong, K. Jin, W. M. Seong, G. Yoon, H. Kim, B. Kim, K. T. Nam, K. Kang, *Adv. Mater. (Weinheim, Ger.)* **2017**, *29*.
- [16] H. Kim, J. Park, I. Park, K. Jin, S. E. Jeong, S. H. Kim, K. T. Nam, K. Kang, *Nat. Commun.* **2015**, *6*.
- [17] R. Subbaraman, D. Tripkovic, K.-C. Chang, D. Strmcnik, A. P. Paulikas, P. Hirunsit, M. Chan, J. Greeley, V. Stamenkovic, N. M. Markovic, *Nat. Mater.* **2012**, *11*, 550.
- [18] F. Dionigi, P. Strasser, *Adv. Energy Mater.* **2016**, *6*.
- [19] J. Suntivich, K. J. May, H. A. Gasteiger, J. B. Goodenough, Y. Shao-Horn, *Science* **2011**, *334*, 1383.
- [20] M. W. Kanan, J. Yano, Y. Surendranath, M. Dincă, V. K. Yachandra, D. G. Nocera, *J. Am. Chem. Soc.* **2010**, *132*, 13692.
- [21] D. K. Bediako, B. Lassalle-Kaiser, Y. Surendranath, J. Yano, V. K. Yachandra, D. G. Nocera, *J. Am. Chem. Soc.* **2012**, *134*, 6801.
- [22] M. Risch, K. Klingan, F. Ringleb, P. Chernev, I. Zaharieva, A. Fischer, H. Dau, *ChemSusChem* **2012**, *5*, 542.
- [23] C. L. Farrow, D. K. Bediako, Y. Surendranath, D. G. Nocera, S. J. Billinge, *J. Am. Chem. Soc.* **2013**, *135*, 6403.

- [24] A. M. Ullman, C. N. Brodsky, N. Li, S.-L. Zheng, D. G. Nocera, *J. Am. Chem. Soc.* **2016**, *138*, 4229.
- [25] L. Trotochaud, S. L. Young, J. K. Ranney, S. W. Boettcher, *J. Am. Chem. Soc.* **2014**, *136*, 6744.
- [26] J. R. Swierk, S. Klaus, L. Trotochaud, A. T. Bell, T. D. Tilley, *J. Phys. Chem. C* **2015**, *119*, 19022.
- [27] D. Friebe, M. W. Louie, M. Bajdich, K. E. Sanwald, Y. Cai, A. M. Wise, M.-J. Cheng, D. Sokaras, T.-C. Weng, R. Alonso-Mori, *J. Am. Chem. Soc.* **2015**, *137*, 1305.
- [28] K. Fominykh, P. Chernev, I. Zaharieva, J. Sicklinger, G. Stefanic, M. Döblinger, A. Müller, A. Pokharel, S. Böcklein, C. Scheu, *ACS Nano* **2015**, *9*, 5180.
- [29] M. Görlin, P. Chernev, J. F. de Araújo, T. Reier, S. Dresp, B. Paul, R. Krähnert, H. Dau, P. Strasser, *J. Am. Chem. Soc.* **2016**, *138*, 5603.
- [30] M. Görlin, J. Ferreira de Araújo, H. Schmies, D. Bernsmeier, S. r. Dresp, M. Gliech, Z. Jusys, P. Chernev, R. Kraehnert, H. Dau, *J. Am. Chem. Soc.* **2017**, *139*, 2070.
- [31] M. S. Burke, M. G. Kast, L. Trotochaud, A. M. Smith, S. W. Boettcher, *J. Am. Chem. Soc.* **2015**, *137*, 3638.
- [32] L. J. Enman, M. S. Burke, A. S. Batchellor, S. W. Boettcher, **2016**.
- [33] N. S. Lewis, D. G. Nocera, *Proc. Natl. Acad. Sci. U.S.A.* **2006**, *103*, 15729.
- [34] M. Grätzel, *Nature* **2001**, *414*, 338.

- [35] D. Gust, T. A. Moore, A. L. Moore, *Acc. Chem. Res.* **2009**, *42*, 1890.
- [36] J. R. Swierk, T. E. Mallouk, *Chem. Soc. Rev.* **2013**, *42*, 2357.
- [37] Y. Tachibana, L. Vayssieres, J. R. Durrant, *Nat. Photonics* **2012**, *6*, 511.
- [38] A. Kudo, Y. Miseki, *Chem. Soc. Rev.* **2009**, *38*, 253.
- [39] T. Faunce, S. Styring, M. R. Wasielewski, G. W. Brudvig, A. W. Rutherford, J. Messinger, A. F. Lee, C. L. Hill, M. Fontecave, D. R. MacFarlane, *Energy Environ. Sci.* **2013**, *6*, 1074.
- [40] J. K. Hurst, *Science* **2010**, *328*, 315.
- [41] T. A. Betley, Q. Wu, T. Van Voorhis, D. G. Nocera, *Inorg. Chem.* **2008**, *47*, 1849.
- [42] D. Galizzioli, F. Tantardini, S. Trasatti, *J. Appl. Electrochem.* **1974**, *4*, 57.
- [43] J. Horkans, M. Shafer, *J. Electrochem. Soc.* **1977**, *124*, 1202.
- [44] S. D. Tilley, M. Cornuz, K. Sivula, M. Grätzel, *Angew. Chem., Int. Ed.* **2010**, *122*, 6549.
- [45] W. J. Youngblood, S.-H. A. Lee, Y. Kobayashi, E. A. Hernandez-Pagan, P. G. Hoertz, T. A. Moore, A. L. Moore, D. Gust, T. E. Mallouk, *J. Am. Chem. Soc.* **2009**, *131*, 926.
- [46] L. Tong, L. Duan, Y. Xu, T. Privalov, L. Sun, *Angew. Chem., Int. Ed.* **2011**, *50*, 445.
- [47] Y. Gorlin, T. F. Jaramillo, *J. Am. Chem. Soc.* **2010**, *132*, 13612.
- [48] H. Wang, H.-W. Lee, Y. Deng, Z. Lu, P.-C. Hsu, Y. Liu, D. Lin, Y. Cui, *Nat. Commun.* **2015**, *6*.

- [49] J. Luo, J.-H. Im, M. T. Mayer, M. Schreier, M. K. Nazeeruddin, N.-G. Park, S. D. Tilley, H. J. Fan, M. Grätzel, *Science* **2014**, *345*, 1593.
- [50] J. Kim, J. S. Kim, H. Baik, K. Kang, K. Lee, *RSC Adv.* **2016**, *6*, 26535.
- [51] S. W. Lee, C. Carlton, M. Risch, Y. Surendranath, S. Chen, S. Furutsuki, A. Yamada, D. G. Nocera, Y. Shao-Horn, *J. Am. Chem. Soc.* **2012**, *134*, 16959.
- [52] W. D. Chemelewski, H.-C. Lee, J.-F. Lin, A. J. Bard, C. B. Mullins, *J. Am. Chem. Soc.* **2014**, *136*, 2843.
- [53] F. Song, X. Hu, *J. Am. Chem. Soc.* **2014**, *136*, 16481.
- [54] M. Dincă, Y. Surendranath, D. G. Nocera, *Proc. Natl. Acad. Sci. U.S.A.* **2010**, *107*, 10337.
- [55] M. Huynh, D. K. Bediako, D. G. Nocera, *J. Am. Chem. Soc.* **2014**, *136*, 6002.
- [56] A. Bergmann, E. Martinez-Moreno, D. Teschner, P. Chernev, M. Gliech, J. F. de Araújo, T. Reier, H. Dau, P. Strasser, *Nat. Commun.* **2015**, *6*.
- [57] M. S. Burke, S. Zou, L. J. Enman, J. E. Kellon, C. A. Gabor, E. Pledger, S. W. Boettcher, *J. Phys. Chem. Lett.* **2015**, *6*, 3737.
- [58] K. J. May, C. E. Carlton, K. A. Stoerzinger, M. Risch, J. Suntivich, Y.-L. Lee, A. Grimaud, Y. Shao-Horn, *J. Phys. Chem. Lett.* **2012**, *3*, 3264.
- [59] A. Grimaud, K. J. May, C. E. Carlton, Y.-L. Lee, M. Risch, W. T. Hong, J. Zhou, Y. Shao-Horn, *Nat. Commun.* **2013**, *4*.
- [60] S. Yagi, I. Yamada, H. Tsukasaki, A. Seno, M. Murakami, H. Fujii, H.

- Chen, N. Umezawa, H. Abe, N. Nishiyama, *Nat. Commun.* **2015**, *6*.
- [61] J. T. Mefford, X. Rong, A. M. Abakumov, W. G. Hardin, S. Dai, A. M. Kolpak, K. P. Johnston, K. J. Stevenson, *Nat. Commun.* **2016**, *7*.
- [62] M. Gong, Y. Li, H. Wang, Y. Liang, J. Z. Wu, J. Zhou, J. Wang, T. Regier, F. Wei, H. Dai, *J. Am. Chem. Soc.* **2013**, *135*, 8452.
- [63] X. Long, J. Li, S. Xiao, K. Yan, Z. Wang, H. Chen, S. Yang, *Angew. Chem., Int. Ed.* **2014**, *126*, 7714.
- [64] F. Song, X. Hu, *Nat. Commun.* **2014**, *5*.
- [65] I. Zaharieva, P. Chernev, M. Risch, K. Klingan, M. Kohlhoff, A. Fischer, H. Dau, *Energy Environ. Sci.* **2012**, *5*, 7081.
- [66] D. M. Robinson, Y. B. Go, M. Mui, G. Gardner, Z. Zhang, D. Mastrogiovanni, E. Garfunkel, J. Li, M. Greenblatt, G. C. Dismukes, *J. Am. Chem. Soc.* **2013**, *135*, 3494.
- [67] D. K. Bediako, Y. Surendranath, D. G. Nocera, *J. Am. Chem. Soc.* **2013**, *135*, 3662.
- [68] Y. Surendranath, M. W. Kanan, D. G. Nocera, *J. Am. Chem. Soc.* **2010**, *132*, 16501.
- [69] K. Jin, J. Park, J. Lee, K. D. Yang, G. K. Pradhan, U. Sim, D. Jeong, H. L. Jang, S. Park, D. Kim, *J. Am. Chem. Soc.* **2014**, *136*, 7435.
- [70] M. Okubo, E. Hosono, J. Kim, M. Enomoto, N. Kojima, T. Kudo, H. Zhou, I. Honma, *J. Am. Chem. Soc.* **2007**, *129*, 7444.
- [71] M. Newville, *J. Synchrotron Rad.* **2001**, *8*, 322.

- [72] S.-W. Han, *International journal of nanotechnology* **2006**, *3*, 396.
- [73] S.-W. Han, E. Stern, D. Haskel, A. Moodenbaugh, *Physical Review B* **2002**, *66*, 094101.
- [74] G. Kresse, J. Furthmüller, *Physical review B* **1996**, *54*, 11169.
- [75] G. Kresse, D. Joubert, *Physical Review B* **1999**, *59*, 1758.
- [76] S. Dudarev, G. Botton, S. Savrasov, C. Humphreys, A. Sutton, *Physical Review B* **1998**, *57*, 1505.
- [77] B. Hammer, L. B. Hansen, J. K. Nørskov, *Physical Review B* **1999**, *59*, 7413.
- [78] M. n. García-Mota, M. Bajdich, V. Viswanathan, A. Vojvodic, A. T. Bell, J. K. Nørskov, *J. Phys. Chem. C* **2012**, *116*, 21077.
- [79] L. Wang, T. Maxisch, G. Ceder, *Physical Review B* **2006**, *73*, 195107.
- [80] A. Jain, G. Hautier, S. P. Ong, C. J. Moore, C. C. Fischer, K. A. Persson, G. Ceder, *Physical Review B* **2011**, *84*, 045115.
- [81] J. Chen, X. Wu, A. Selloni, *Physical Review B* **2011**, *83*, 245204.
- [82] M. Bajdich, M. García-Mota, A. Vojvodic, J. K. Nørskov, A. T. Bell, *J. Am. Chem. Soc.* **2013**, *135*, 13521.
- [83] J. Rossmeisl, K. Dimitrievski, P. Siegbahn, J. K. Nørskov, *J. Phys. Chem. C* **2007**, *111*, 18821.
- [84] A. McDonald, B. Scott, G. Villemure, *Microporous Mesoporous Mater.* **2009**, *120*, 263.
- [85] F. Alvarez-Ramírez, J. Toledo-Antonio, C. Angeles-Chavez, J. Guerrero-

- Abreo, E. López-Salinas, *J. Phys. Chem. C* **2011**, *115*, 11442.
- [86] A. Dumas, M. Mizrahi, F. o. Martin, F. G. Requejo, *Cryst. Growth Des.* **2015**, *15*, 5451.
- [87] Q. Rong, L.-L. Long, X. Zhang, Y.-X. Huang, H.-Q. Yu, *Appl. Energy* **2015**, *153*, 63.
- [88] C. Qiu, J. Jiang, L. Ai, *ACS Appl. Mater. Interfaces* **2015**, *8*, 945.
- [89] R. Trujillano, J.-F. Lambert, C. Louis, *J. Phys. Chem. C* **2008**, *112*, 18551.
- [90] M. A. Melo Jr, C. Airoidi, *Dalton Trans.* **2010**, *39*, 10217.
- [91] A. R. Pawley, R. L. Jones, *Phys. Chem. Miner.* **2011**, *38*, 753.
- [92] M. Welch, A. Pawley, S. Ashbrook, H. Mason, B. Phillips, *Am. Mineral.* **2006**, *91*, 1707.
- [93] A. Grimaud, C. E. Carlton, M. Risch, W. T. Hong, K. J. May, Y. Shao-Horn, *J. Phys. Chem. C* **2013**, *117*, 25926.
- [94] J. A. Seabold, K.-S. Choi, *J. Am. Chem. Soc.* **2012**, *134*, 2186.
- [95] F. Yang, K. Sliozberg, I. Sinev, H. Antoni, A. Bähr, K. Ollegott, W. Xia, J. Masa, W. Grünert, B. R. Cuenya, *ChemSusChem* **2017**, *10*, 156.
- [96] W. Liu, K. Du, L. Liu, J. Zhang, Z. Zhu, Y. Shao, M. Li, *Nano Energy* **2017**, *38*, 576.
- [97] J. Masa, P. Weide, D. Peeters, I. Sinev, W. Xia, Z. Sun, C. Somsen, M. Muhler, W. Schuhmann, *Adv. Energy Mater.* **2016**.
- [98] P. W. Menezes, A. Indra, A. Bergmann, P. Chernev, C. Walter, H. Dau, P. Strasser, M. Driess, *Journal of Materials Chemistry A* **2016**, *4*, 10014.

- [99] N. Jiang, B. You, M. Sheng, Y. Sun, *Angew. Chem., Int. Ed.* **2015**, *54*, 6251.
- [100] X. Zou, A. Goswami, T. Asefa, *J. Am. Chem. Soc.* **2013**, *135*, 17242.
- [101] D. Guo, J. Qi, W. Zhang, R. Cao, *ChemSusChem* **2017**, *10*, 394.
- [102] L. Wang, X. Huang, J. Xue, *ChemSusChem* **2016**, *9*, 1835.
- [103] R. D. Smith, M. S. Prévot, R. D. Fagan, Z. Zhang, P. A. Sedach, M. K. J. Siu, S. Trudel, C. P. Berlinguette, *Science* **2013**, *340*, 60.
- [104] S. Wang, J. Nai, S. Yang, L. Guo, *ChemNanoMat* **2015**, *1*, 324.
- [105] S. K. Bikkarolla, P. Papakonstantinou, *J. Power Sources* **2015**, *281*, 243.
- [106] M. Li, Y. Xiong, X. Liu, X. Bo, Y. Zhang, C. Han, L. Guo, *Nanoscale* **2015**, *7*, 8920.
- [107] X. Wu, K. Scott, *J. Mater. Chem.* **2011**, *21*, 12344.
- [108] R. Singh, J. Pandey, N. Singh, B. Lal, P. Chartier, J.-F. Koenig, *Electrochim. Acta* **2000**, *45*, 1911.
- [109] Z. Lu, L. Qian, Y. Tian, Y. Li, X. Sun, X. Duan, *Chem. Commun. (Cambridge, U. K.)* **2016**, *52*, 908.
- [110] J. Y. Chen, J. T. Miller, J. B. Gerken, S. S. Stahl, *Energy Environ. Sci.* **2014**, *7*, 1382.
- [111] B. Zhang, X. Zheng, O. Voznyy, R. Comin, M. Bajdich, M. García-Melchor, L. Han, J. Xu, M. Liu, L. Zheng, *Science* **2016**, *352*, 333.
- [112] R. D. Smith, M. S. Prévot, R. D. Fagan, S. Trudel, C. P. Berlinguette, *J. Am. Chem. Soc.* **2013**, *135*, 11580.

- [113] S. Klaus, Y. Cai, M. W. Louie, L. Trotochaud, A. T. Bell, *J. Phys. Chem. C* **2015**, *119*, 7243.
- [114] D. A. Corrigan, *J. Electrochem. Soc.* **1987**, *134*, 377.
- [115] J. Y. Chen, L. Dang, H. Liang, W. Bi, J. B. Gerken, S. Jin, E. E. Alp, S. S. Stahl, *J. Am. Chem. Soc.* **2015**, *137*, 15090.
- [116] B. J. Trzeźniewski, O. Diaz-Morales, D. A. Vermaas, A. Longo, W. Bras, M. T. Koper, W. A. Smith, *J. Am. Chem. Soc.* **2015**, *137*, 15112.
- [117] D. Wang, J. Zhou, Y. Hu, J. Yang, N. Han, Y. Li, T.-K. Sham, **2015**.
- [118] M. Zhang, M. De Respinis, H. Frei, *Nature Chem.* **2014**, *6*, 362.
- [119] B. S. Yeo, A. T. Bell, *J. Phys. Chem. C* **2012**, *116*, 8394.
- [120] O. Diaz-Morales, I. Ledezma-Yanez, M. T. Koper, F. Calle-Vallejo, **2015**.
- [121] A. Jain, G. Hautier, C. J. Moore, S. P. Ong, C. C. Fischer, T. Mueller, K. A. Persson, G. Ceder, *Computational Materials Science* **2011**, *50*, 2295.
- [122] M. Capdevila-Cortada, Z. Łodziana, N. López, ACS Publications, 2016.
- [123] M. Aykol, C. Wolverton, *Physical Review B* **2014**, *90*, 115105.
- [124] P. Bothra, S. K. Pati, *ACS Energy Letters* **2016**, *1*, 858.
- [125] K. Mathew, R. Sundararaman, K. Letchworth-Weaver, T. Arias, R. G. Hennig, *The Journal of chemical physics* **2014**, *140*, 084106.
- [126] K. Mathew, R. Hennig, 2015.
- [127] J. A. Gauthier, C. F. Dickens, L. D. Chen, A. D. Doyle, J. K. Nørskov, *J. Phys. Chem. C* **2017**.

- [128] S. Sakong, M. Naderian, K. Mathew, R. G. Hennig, A. Groß, *The Journal of chemical physics* **2015**, *142*, 234107.
- [129] F. Calle-Vallejo, A. Krabbe, J. M. García-Lastra, *Chemical Science* **2017**, *8*, 124.
- [130] A. Grimaud, O. Diaz-Morales, B. Han, W. T. Hong, Y.-L. Lee, L. Giordano, K. A. Stoerzinger, M. T. Koper, Y. Shao-Horn, *Nature Chem.* **2017**, *9*, 457.
- [131] J. Huang, J. Chen, T. Yao, J. He, S. Jiang, Z. Sun, Q. Liu, W. Cheng, F. Hu, Y. Jiang, *Angew. Chem., Int. Ed.* **2015**, *54*, 8722.
- [132] B. S. Yeo, A. T. Bell, *J. Am. Chem. Soc.* **2011**, *133*, 5587.
- [133] J. A. Koza, Z. He, A. S. Miller, J. A. Switzer, *Chem. Mater.* **2012**, *24*, 3567.
- [134] Z. Zhuang, W. Sheng, Y. Yan, *Adv. Mater. (Weinheim, Ger.)* **2014**, *26*, 3950.
- [135] B. H. Suryanto, X. Lu, C. Zhao, *Journal of Materials Chemistry A* **2013**, *1*, 12726.
- [136] X. Liu, Z. Chang, L. Luo, T. Xu, X. Lei, J. Liu, X. Sun, *Chem. Mater.* **2014**, *26*, 1889.
- [137] G. Abellán, J. A. Carrasco, E. Coronado, J. Romero, M. Varela, *Journal of Materials Chemistry C* **2014**, *2*, 3723.
- [138] J. Jiang, A. Zhang, L. Li, L. Ai, *J. Power Sources* **2015**, *278*, 445.
- [139] X. Zhang, L. An, J. Yin, P. Xi, Z. Zheng, Y. Du, *Scientific Reports* **2017**,

7.

- [140] C. Tang, H. S. Wang, H. F. Wang, Q. Zhang, G. L. Tian, J. Q. Nie, F. Wei, *Adv. Mater. (Weinheim, Ger.)* **2015**, *27*, 4516.
- [141] X. Han, C. Yu, J. Yang, C. Zhao, H. Huang, Z. Liu, P. M. Ajayan, J. Qiu, *Advanced Materials Interfaces* **2016**, *3*.
- [142] G. Karkera, T. Sarkar, M. Dixit Bharadwaj, A. S. Prakash, *ChemCatChem*.
- [143] K.-Y. Niu, F. Lin, S. Jung, L. Fang, D. Nordlund, C. C. McCrory, T.-C. Weng, P. Ercius, M. M. Doeff, H. Zheng, *Nano Lett.* **2015**, *15*, 2498.